UNIVERSITY OF CALIFORNIA
Los Angeles

Self-Guiding of Relativistically-Intense, Ultrashort Laser Pulses in Underdense Plasmas

A dissertation submitted in partial satisfaction
of the requirements for the degree
Doctor of Philosophy in Electrical Engineering

by

Joseph Edwin Ralph III

2009

The dissertation of Joseph Edwin Ralph III is approved.

George Morales Ph.D.

Christoph Niemann Ph.D.

Warren Mori Ph.D.

Chandrashekhar Joshi Ph.D, Committee Chair

University of California, Los Angeles

2009

To Tobi and Cory.

Table of Contents

List of Figures

List of Tables

VITA

2000	B.S. (Electrical Engineering) and (PHysics), Temple University, Philadelphia PA.
2005	M.S. (Electrical Engineering), University of California Los Angeles, Los Angeles, California.
2000	Optical/ Electrical Engineer Metrologic Instruments Inc. Blackwood NJ working on holographic optics and analog signal processing circuits.
2002–2008	Graduate Student Researcher, University of California Los Angeles, Los Angeles CA working on experiments on guiding high intensity laser pulses in a hollow capillary, Inverse Free Electron Lasers, Nonlinear Difference Frequency Mixing in GaAs for production of high power terahertz radiation, Nonlinear optics of underdense plasmas using ultrashort laser pulses, self-guiding of ultraintense ultrashort laser pulses in underdense plasma, acceleration of electrons in a self-guided laser wakefield accelerator using a 100 TW laser.

PUBLICATIONS

J.E. Ralph, K.A. Marsh, A.E. Pak, W. Lu, C.E. Clayton, F. Fang, W.B. Mori, and C. Joshi, "Self-guiding of Ultra-short, Relativistically Intense Laser Pulses

through Underdense Plasmas in the Blowout Regime", Submitted to Physical Review Letters

J.E. Ralph et. al.,"Experimental investigation of self-guiding using a matched laser beam in a CM scale length underdense plasm" Particle Accelerator Conference, 2007 Proceedings, pp. 3052-3054

F. Fang et. al.,"Evolution of relativistic plasma wave-front in LWF" Particle Accelerator Conference, 2007 Proceedings, pp. 1919-1921

S. Ya. Tochitsky, J. E. Ralph, C. Sung, and C. Joshi"Generation of Terahertz Megawatt-Power Pulse by Noncollinear Difference Frequency Mixing in GaA", J. Appl. Phys. 98, 026101 (2005)

Musumeci et. al.,"High Energy Gain of Trapped Electrons in a Tapered, Diffraction-Dominated Inverse Free-Electron-Lase", Phys. Rev. Lett. 94 (2005)

J.E. Ralph et al." Production of Terahertz Seed Radiation for FEL/IFEL Microbunchers for Second Generation Plasma Beatwave Experiments in Neptun", Particle Accelerator Conference, 2005 Proceedings pp. 2780- 2782

C. Sung et. al., "Terahertz IFEL/FEL Microbunching for Plasma Beatwave Accelerator", Particle Accelerator Conference, 2005 Proceedings pp. 2812- 2814

Musumeci, P. et. al. "High Energy Gain IFEL at UCLA Neptune Laborator", Particle Accelerator Conference, 2005 Proceedings pp. 500- 504

C. Sung et. al. "Study of a THz IFEL prebuncher for laser-plasma accelerator", AAC Proceeding 2004, pp. 922-928

ABSTRACT OF THE DISSERTATION

Self-Guiding of Relativistically-Intense, Ultrashort Laser Pulses in Underdense Plasmas

by

Joseph Edwin Ralph III

Doctor of Philosophy in Electrical Engineering

University of California, Los Angeles, 2009

Professor Chandrashekhar Joshi Ph.D, Chair

In this thesis we have investigated the self-guiding of relativistically intense ($I > 10^{18}$ W/cm^2) but extremely short ($\tau \sim 50fs$) laser pulses in underdense plasmas through experiments and supporting theory and simulations. Experiments were conducted using a multiterawatt Ti:Sapphire laser system and utilized gas jet targets of various lengths and densities. We find that such laser pulses can propagate tens of Rayleigh lengths until they are pump depleted if their initial focused spot size is "matched" to the plasma and the laser pulse has a peak power close to the "critical power" for relativistic guiding. In most of the experiments described in this thesis the laser pulse width was on the order of the wavelength of a plasmon moving with a phase velocity of c and therefore strong wake excitation was expected to occur. To determine whether self-guiding occured, we looked for a well defined spot in the image of the exit of plasma in addition to corresponding spectral modulation associated with a high amplitude plasma wake using two forward spectrometers. Indeed spectral analysis of the images of the laser spot that exited the plasma revealed that the self-guided portion of the laser pulse underwent considerable spectral modulation due to photon acceleration and de-

celeration in the wake. Energy balance of the transmitted laser spot also showed that most of the transmitted energy was in the guided spot when the beam was "matched" to the plasma. These optimally guided spots also tended to show the greatest red shift of the pulse spectrum as expected by photon deceleration by the wake. For plasma densities greater or less than the optimum density for guiding, the guided spot contained a smaller fraction of the total transmitted energy. The guided spots for these non-optimal plasma density conditions had a surrounding halo of typically blue shifted photons due to ionization of the neutral gas. Finally, by using plasmas of different length and varying plasma density and laser power, we show that the maximum distance over which such ultra-short, ultraintense laser pulses can be propagated in a plasma are limited over distances that can be predicted by the nonlinear pump depletion theory.

CHAPTER 1

Introduction

In the famous paper by Tajima and Dawson, the concept of laser driven plasma based accelerators was introduced through 1-d particle simulations[70]. This paper provided an impetus to the establishment of a new subfield within plasma physics known as plasma wakefield accelerators. Indeed, it is technology based on this concept that poses the greatest promise of replacing the current radio frequency cavity based accelerators and becoming the technology of choice for the next generation of particle accelerators.

Current linear accelerator technology uses high field radio frequency cavities to accelerate electrons and positrons to high energy. However, the acceleration gradient is limited by the maximum sustainable field in the cavity before break down occurs. Todays accelerators can maintain gradients of approximately 50 MeV / meter. This requires distances measured in kilometers to reach energies on the order of 100 GeV which are required for near term experiments in high energy physics. Plasmas, on the other hand can support enormous electric fields with accelerating gradients of 100s of GeV / meter which may reduce the scale of high energy particle accelerators.

Until recently, high power lasers could not access the laser wakefield regime, wherein the laser pulse resides in the first plasma wave wake. Instead experiments relied on other methods to excite relativistic high amplitude plasma waves. One such method uses beatwaves excited by a two frequency laser to resonantly excite

the high amplitude plasma wave capable of achieving high gradients[30, 70]. Another method uses a long intense pulse which will self-modulate due stimulated Raman scattering into a series of pulses with a period of the plasma wavelength. This series of pulses will than resonantly excite the plasma wave[63, 70]. Initial experimental results using this method produced some of the first accelerated electrons from plasma wave breaking (self-injection)[50]. As the laser technology evolved, pulses continued increase in energy and decrease in duration. Laser pulses were intense enough to tunnel ionize a nuetral gas and create a plasma. Today the laser pulses are so intense that this occurs early in the rise time of the laser pulse producing a fully ionized uniform cold plasma, ideal for wakefield acceleration[2, 36, 37]. Experiments in the late 1990s and early 2000s continued to rely on interactions of the laser pulse with the plasma wave to obtain resonance. This regime came to be known as self-modulated laser wakefield acceleration or SM-LWFA. Experiments in this regime produced some very important results such as acceleration of electrons to the 100 MeV energy range in about one millimeter[7, 73, 74]. Later a variation of the SM-LWFA was identified which results if a very intense pulse longer than the ideal half a plasma wavelength needed for true LWFA, but shorter than tens of plasma periods long [45].

It was the introduction of the chirped pulse amplification technology in the mid 1980s that provided the breakthrough in laser technology which allowed the production of short intense pulses which could be used for LWFA[68]. By 2000, CPA lasers had advanced to the point where the pulses were high enough in intensity and short enough to perform experiments close to the ideal LWFA[44]. Since then, ultra-short pulse ultra-intense lasers have advanced and become reliable. Modern chirped pulse amplification (CPA) type lasers use Ti:sapphire as the gain medium with highly advanced pulse shaping control systems to achieve powers greater than 100 TW with durations on the order of $\sim$30 fs. These lasers,

which were scientific research projects in their own right only a few years ago are now commercially available and have opened new paths and research directions in plasma physics, optical physics and high-energy density science[54].

The ultrahigh intensities of these lasers when focused lead to a new development in LWFAs, the blowout or bubble regime. The complete cavitation of electron, which first occurs in this regime was first theorized for high power laser pulses in the late 1980s through an important paper on nonlinear self-focusing in plasmas[69]. The importance of this regime as a plasma based accelerator (as realized using an electron beam driver) was pointed out in the early 1990s[58]. Ten years later, in 2002, Pukhov and Meyer-ter-vehn published a paper highlighting this regime[56] for laser drivers. Most recently, an approach to the physics in this regime using the key variable of the blowout radius R_b has produced a set of simplified equations suitable for scaling[40, 39, 38] and design of experiments. In a series of experiments highlighted in the journal *Nature*, three groups independently demonstrated that highly energetic and quasi-monoenergetic electrons could be produced through self-injection in a LWFA[48, 23, 17]. Prior results achieved high acceleration but generally with large energy spreads. Recently, experiments in France have demonstrated controlled injection of electrons into a LWFA leading to a monoenergetic beam[20]. Other methods have also very recently demonstrated controlled injection[22]. These efforts have effectively provided solutions to one of the major problems in LWFA, controlling when and if the electrons are injected into the wake behind the laser pulse.

The overall progress in the field of LWFA and the potential for a relatively compact accelerator has caught the attention of scientists in other fields. In the field of medicine researchers have been following this progress with eye toward treating cancer. As these small scale accelerators mature as a technology, it has

been suggested, for example to use the electron beam generated from compact accelerators to treat certain types of cancer. Such procedures now use proton beams to destroy cancer cells deep within the body without harming the surrounding tissue [42, 25, 46]. Because of the excessive size, a tradition RF accelerator used for this electron beam treatment would be impractical for all but a few research hospitals. One can imagine other future uses as well. The department of Homeland security here in US could potentially use the nearly collimated betatron X-Rays emitted by electrons as they are accelerated in a laser wakefield accelerator as a source for detecting fissionable materials through the excitation of nuclear resonances.

The promise of plasma based acceleration is not limited, however, to small scale accelerators. A few groups, have pushed the concept into the realm of high energy physics. Laser based accelerators have now achieved GeV level electron beams [32, 33, 35]. So far, however, the collaboration between, Stanford University, the University of Southern California, and our group at UCLA have shown, by far, the greatest advance in plasma based acceleration. When a high energy electron beam driver is used the plasma accelerator is termed Plasma Wakefield Accelerator PWFA. In recent experiments using the 42 GeV beam at the Stanford Linear Accelerator Center (SLAC) as the driver for PWFA, an energy gain of at least 42 GeV was observed after propagating the beam through less than one meter of plasma[3]. To put this into perspective, the previous 3000 meters were needed to achieve the first 40 GeV! These historic results show conclusively the potential for applications in high energy physics.

As lasers advance, the field of short ultraintense pulse laser plasma interactions must also advance. Very recently, a fully 3 dimensional theory developed here at UCLA[39, 40, 38] has provided a theoretical foundation for lasers propagating in

the blowout regime. The wealth of insight gained from this theory can be used to accurately calculate the parameters needed to optimize a LWFA or PWFA[40].

The physical picture associated with LWFA is presented visually in Fig. 1.1 which shows a cartoon snap shot of a slice of the interaction of the ultra-short ultra-intense laser pulse and an underdense plasma. In this figure the laser pulse, shown as the blue wavepacket is propagating from left to right. Ionization occurs at relatively low intensities compared to the peak intensity and so occurs early in the pulse. Here the blue represents the neutral gas and white, the ionized gas. The ponderomotive force associated with this pulse pushes plasma electrons forward and radially (shown in pink) leaving a region of near complete cavitation (shown in green) behind the pulse. The ions which move on a much slower time scale are essentially immobile providing a uniform background positive charge. After the pulse has passed, the evacuated electrons respond to the coulomb attraction created by the displaced electrons and background positive charge and are pulled back radially. This continues as the pulse moves through the plasma at a velocity close to the speed of light. The magnitude of the longitudinal electric field setup by this moving charge displacement is sufficient for trapping and acceleration of electrons. Such a bunch is shown in Fig. 1.1 as the ellipse with a minus sign inside. As the charge bunch is accelerated, it moves with a velocity which is faster than the wake structure. If the charge bunch moves sufficiently forward in the structure, it can outrun the accelerating structure or dephase, limiting the maximum acceleration. Alternatively, the drive pulse can loose sufficient energy by giving it to the wake structure such that it can no longer drive a wake (pump depletion). To achieve the greatest efficiency, the parameters of the LWFA should be chosen so that the electrons almost dephase when the laser pulse runs out of energy.

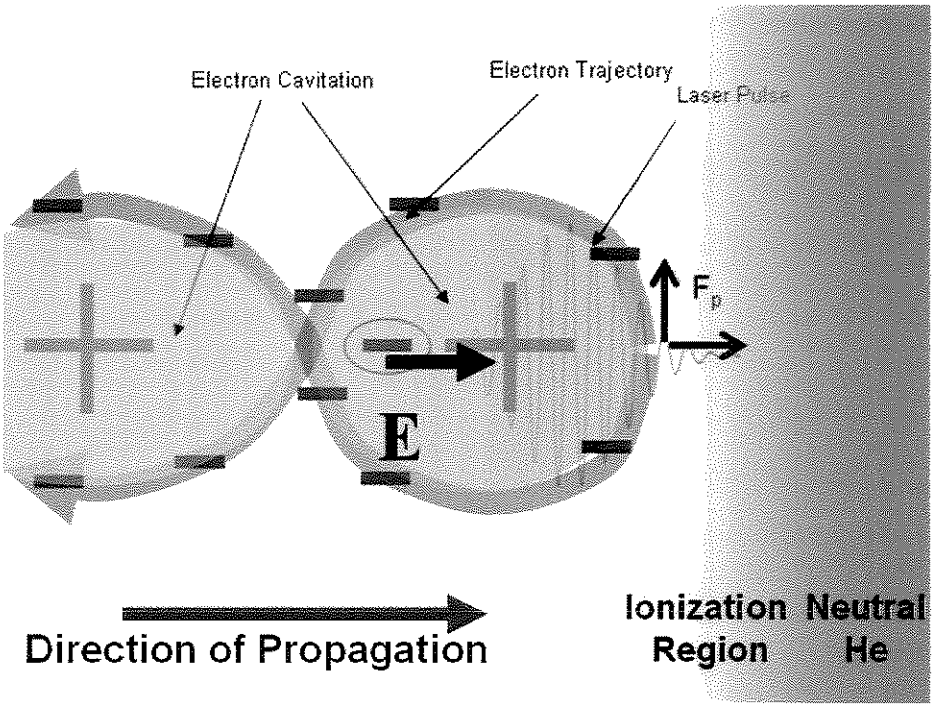

Figure 1.1: Physical Picture of Laser Wakefield Acceleration.

In addition to pump depletion, the laser pulse may become ineffective at driving a large amplitude wake if the intensity I of the pulse diminishes. Because the initial force on the electrons is nonlinear such that $F_p \propto \nabla(a^2)$ and $a \propto \sqrt{(I\lambda^2)}$, the magnitude of the wake structure depends on the intensity of the laser pulse. So, it is important to keep the intensity of the laser pulse high throughout the desired interaction length. The intensity can decrease if the pulse is stretched in time or expanded in space. Since controlling the temporal evolution of the laser pulse is not currently practical, much effort has been spent on controlling the spot size evolution.

In vacuum, a laser pulse with an initial spot size w_0 (given as the radius where the intensity falls off a factor of $1/e^2$) will diffract according to the well known equation $w(z) = w_0\sqrt{1 + z^2/z_R^2}$. Here the Rayleigh length is given as $z_R = \pi w_o^2/\lambda_0$. Diffraction of this type will lead to larger spots and therefore lower intensities limiting the interaction length to essentially 1 Rayleigh Length. Since the acceleration is dependent upon the interaction length of the pulse with the plasma, much research in LWFA has focused on extending this length. One obvious method to extend the interaction length is to extend the Rayleigh Length. Some groups have used this method to extend their interaction length in LWFA with good results[17]. The biggest drawback of this method is that as the spot size is increased to extend z_R, the power must be increased quadratically to maintain the same intensity. This quickly leads to very high power pulses for even modest length accelerators.

Many groups have turned to the creation of guiding structures within the plasma itself[63] to extend the interaction length. Several methods have been explored. Using an axicon to create a line focus, Durfee and Milchberg showed that channels can formed by heating a narrow region of ions[11]. These hot

ions spread out radially pulling the electrons and creating a density depression sufficient for guiding a second laser pulse. Variations on this theme using different focusing methods have shown similar results[78, 24]. At the same time, capillary discharges appeared as plasma sources which could produce such channels either through ablation of the walls of a hollow capillary[28] or through the an electrical discharge[61, 12]. The capillary discharge has proven effective in guiding pulses in plasmas and resulted in some of the best LWFA results LWFA[55, 33].

Finally, self-guiding can be employed to extend the interaction length. In the mid 1970s, it was recognized that the relativistic mass corrections due to high power laser pulses could produce self-focusing[49]. More than a decade later, a self-consistent theory showed that for short pulses (immobile ions), the ponderomotive force of the laser pulse would also cause an electron density depression and electron cavitation at some point behind the pulse[69] for laser pulses with powers greater than P_c. This theory also confirmed the critical laser power where relativistic self-focusing begins as $P_c \approx 17\omega_o^2/\omega_p^2$ GW. In the early 1990s, work by Sprangle, Esarey and Ting resulted in a quasi-static theory which could be applied to many problems related to LWFA[65]. It was in this paper (and later papers by the same group) that self-guiding was dismissed for the kind of short laser pulses necessary for LWFA since the front (λ_p portion) of the pulse would diffract as if in vacuum. Simulations performed with new particle codes seemed to agree that these short pulses could not be self-guided for significant distances due to diffraction at the front of the pulse[51]. Finally, experiments performed by reputable groups also seemed to show that short-pulses could not be guided over significant lengths[19, 24]. With simulation, theory and experiment all seemingly in agreement, the field moved toward plasma guiding structures to extend the interaction length. Even so, Decker and Mori performed simulations and presented theory as early as the mid 1990s that suggested that self-guiding may be

possible for fast rise-time pulses[9]. Experiments conducted in Taiwan a few years later also suggested that short-pulse self-guiding was possible[77]. Finally, recent theoretical work by Lu outlined the process wherein self-guiding is possible for short laser pulses[41, 39, 40] applying the results obtained by Decker and Mori[9]. Simulations presented through work by Lu also verified these conclusions. This work has recently revived the possibility of self-guiding as a method of extending the interaction length in LWFAs. As a result, self-guiding of ultra-short laser pulses has recently been demonstrated in LWFA type experiments[71, 57] with ongoing and future experiments planned in this self-guided regime[47].

CHAPTER 2

Theory

2.1 Introduction to Theory

When the laser pulse duration is on the order of a plasma wavelength for a plasmon that has a phase velocity $\sim$ c, the evolution of the laser pulse is tied to the evolution of the plasma wake. It is the wake, and it's various properties that effect the laser pulse and vice-versa. In this chapter, a general overview of wake formation and how this wake effects the laser pulse will be given. Since this dissertation is primarily experimental, this chapter will focus on the implications of theory and its relation to experimental results. Even so, careful explanation will be given to tie in the physics of important equations with the simulation and experimental results, which will be presented in subsequent chapters.

In light of the complex nature of laser plasma interactions, the discussion presented here will focus on phenomena observed in the experiment after providing a general foundation. This includes the nonlinear effects of self-focusing (guiding), photon acceleration (deceleration) and pump depletion.

2.2 The Quasi static Approximation and Wake Formation Related to Short Pulse Lasers

The quasi-static approximation, which is also known as the frozen field approximation, forms the basis for much of the theory describing laser produced plasma wakefields as described by P. Sprangle [64, 65] and his group in the early 1990s. The development here follows notes on the subject obtained through an advanced lecture series given by W. Mori[52]. The definition of a highly underdense plasma is $\omega_p/\omega_0 << 1$, where the oscillation frequency of the laser electric field $\omega_o = 2\pi c/\lambda_o$ and the electron plasma frequency $\omega_p = \sqrt{4\pi n_e e^2/m_e}$. Here λ_o is the laser wavelength, m_e is the electron mass, and e is the charge of an electron. The characteristic time scales are inherent in this definition. Here the laser electric field changes on the scale of $\tau_{laser} = \omega_0^{-1}$. The plasma responds on time scale of $\tau_{plasma} = \omega_0^{-1}$. Since the plasma response time is much longer than the field oscillation time of the laser, physics happening on the time scale of the τ_{laser} can be neglected as long as the pulse duration τ_L is sufficiently long compared with the time scale of the envelope evolution $\tau_e \approx \frac{\omega_0}{\omega_p}\omega_p^{-1}$. In the following development, the plasma wake response to a short laser pulse will be developed in 1-d. The ions which respond on a much longer time scale are assumed to be immobile, providing a uniform positive background charge.

Starting with the Euler's equation and Maxwell's equation, we now develop a basis for short pulse laser plasma interactions.

$$\left(\frac{\partial}{\partial t} + \mathbf{v}\cdot\nabla\right)\mathbf{p} = -e\left(\mathbf{E} + \frac{\mathbf{v}}{c}\times\mathbf{B}\right) \tag{2.1}$$

$$-\nabla\times\mathbf{E} = \frac{1}{c}\frac{\partial}{\partial t}\mathbf{B} \tag{2.2}$$

$$\nabla \times \mathbf{B} = \frac{4\pi \mathbf{J}}{c} + \frac{1}{c}\frac{\partial}{\partial t}\mathbf{E} \tag{2.3}$$

$$\nabla \cdot \mathbf{B} = 0 \tag{2.4}$$

$$\nabla \cdot \mathbf{E} = 4\pi\rho = 4\pi e\left(n_0 - n\right) \tag{2.5}$$

Taking the curl of equation 2.1,

$$\frac{\partial}{\partial t}\left(\nabla \times \mathbf{p}\right) + \nabla \times \left(\mathbf{v} \cdot \mathbf{p}\right) = -e\left[\nabla \times \mathbf{E} - \frac{e}{c}\nabla \times \left(\mathbf{v} \times \mathbf{B}\right)\right] \tag{2.6}$$

Using equation 2.2, we can rewrite equation 2.6 in terms of only the magnetic field.

$$\frac{\partial}{\partial t}\left(\nabla \times \mathbf{p}\right) + -\nabla \times \left(\mathbf{v} \times \nabla \times \mathbf{p}\right) = -\frac{e}{c}\left[\frac{\partial}{\partial t}\mathbf{B} + \nabla \times \left(\mathbf{v} \times \mathbf{B}\right)\right] \tag{2.7}$$

Combining terms,

$$\frac{\partial}{\partial t}\left[\nabla \times \mathbf{p} - \frac{e}{c}\mathbf{B}\right] - \nabla \times \left[\mathbf{v} \times \left(\nabla \times \mathbf{p} - \frac{e}{c}\mathbf{B}\right)\right] = 0 \tag{2.8}$$

The curl of the vector potential $\mathbf{B} = \nabla \times \mathbf{A}$ can now be substituted for $\mathbf{B}$. The term $\nabla \times \mathbf{p} - \frac{e}{c}\mathbf{B} \rightarrow \nabla \times \left(\mathbf{p} - \frac{e}{c}\mathbf{A}\right)$ can now be recognized as the curl of the canonical momentum P (or vorticity Λ) of an electron. So, equation 2.8 can now be written as.

$$\frac{\partial}{\partial t}\nabla \times P - \nabla \times \mathbf{v} \times \left(\nabla \times P\right) = 0 \tag{2.9}$$

For an unmagnetized plasma, $\nabla \times P = 0$, so

$$\nabla \times \mathbf{p} = \frac{e}{c}\mathbf{B} \tag{2.10}$$

As a result, the modified Euler Equation for no external B field can be written as,

$$\left(\frac{\partial}{\partial t} + \mathbf{v} \cdot \nabla\right)\mathbf{p} = -e\mathbf{E} + -\nabla \times (\nabla \times \mathbf{p}) \tag{2.11}$$

Using the identity $\mathbf{v} \cdot \nabla\mathbf{p} = mc^2\nabla\gamma - \mathbf{v} \times \nabla\mathbf{p}$, equation 2.11 reduces to the form,

$$\frac{\partial}{\partial t}\mathbf{p} = -e\mathbf{E} - mc^2\nabla\gamma \tag{2.12}$$

where the relativistic factor $\gamma = \sqrt{1 + p^2/(m^2c^2)}$. Taking the time derivative of equation 2.12.

$$\frac{\partial^2}{\partial t^2}\mathbf{p} = -e\frac{\partial}{\partial t}\mathbf{E} - mc^2\nabla\frac{\partial}{\partial t}\gamma \tag{2.13}$$

From equation 2.3 and using equation 2.10

$$\frac{\partial^2}{\partial t^2}\mathbf{p} = -e\left(\frac{c^2}{e}\nabla \times \nabla \times \mathbf{p} - 4\pi\mathbf{J}\right) - mc^2\frac{\partial}{\partial t}\nabla\gamma \tag{2.14}$$

The current density can be written also in terms of momentum, $\mathbf{J} = -en\mathbf{v} = -en\mathbf{p}/\gamma$. Substituting the electric field from equation 2.12 into equation 2.5 and solving for the density n.

$$n = n_0 - \nabla \cdot \frac{1}{4\pi e^2}\left(\frac{\partial}{\partial \mathbf{t}}\mathbf{p} - mc^2\nabla\gamma\right) \tag{2.15}$$

Finally, after plugging equation 2.15, we have an equation of motion for a cold fluid or single electron.

$$\frac{\partial^2}{\partial t^2}\mathbf{p} + c^2\nabla\times(\nabla\times\mathbf{p}) + \left(\omega_{p0}^2 + \frac{1}{m}\frac{\partial}{\partial t}\nabla\cdot\mathbf{p} + c^2\nabla^2\gamma\right)\frac{\mathbf{p}}{\gamma} + mc^2\frac{\partial}{\partial t}\nabla\gamma = 0 \quad (2.16)$$

This equation still maintains all the physics. Historically, it is at this point where normalized units are introduced. This practice often presents frustration for experimentalists who require *real* units to make comparisons with theory. However true this may be, working in normalized units presents a far less cumbersome path forward and so we change to normalized units. The normalized units are:$\mathbf{p_n} \rightarrow \mathbf{p}/mc, t_n \rightarrow t/\omega_p, z_n \rightarrow z(c/\omega_p)^{-1}, \omega_p \rightarrow 1$. Substituting normalized units and dropping the subscripts, equation 2.16 becomes,

$$\frac{\partial^2}{\partial t^2}\mathbf{p} + \nabla\times(\nabla\times\mathbf{p}) + \left(1 + \frac{\partial}{\partial t}\nabla\cdot\mathbf{p} + \nabla^2\gamma\right)\frac{\mathbf{p}}{\gamma} + \frac{\partial}{\partial t}\nabla\gamma = 0 \quad (2.17)$$

Now, this equation will be used as the basis for determining the interaction between a short laser pulse and an underdense plasma. For a short laser pulse pulse propagating in the z direction, $\nabla \rightarrow \hat{z}\frac{\partial}{\partial z}$ in 1-d,

$$\hat{x}\ \frac{\partial^2}{\partial t^2}p_x - \frac{\partial^2}{\partial z^2}p_x + \frac{p_x}{\gamma}\left(1 + \frac{\partial}{\partial t}\frac{\partial}{\partial z}p_z + \frac{\partial^2}{\partial z^2}\gamma\right) \quad (2.18)$$

$$\hat{z}\ \frac{\partial^2}{\partial t^2}p_z + \frac{p_z^2}{\gamma}\left(1 + \frac{\partial}{\partial t}\frac{\partial}{\partial z}p_z + \frac{\partial^2}{\partial z^2}\gamma\right) + \frac{\partial}{\partial t}\frac{\partial}{\partial z}\gamma = 0 \quad (2.19)$$

Switching to coordinates in the frame moving with laser pulse, let $\zeta = ct - z$ and $s = z$. So the partials are modified as $\frac{\partial}{\partial t} \rightarrow \frac{\partial}{\partial \zeta}$, and $\frac{\partial}{\partial z} \rightarrow \frac{\partial}{\partial s} - \frac{\partial}{\partial \zeta}$. Substituting into equations 2.18 and 2.19,

$$\hat{x}\ 2\frac{\partial}{\partial s}\frac{\partial}{\partial \zeta}p_x + \frac{p_x}{\gamma}\left[1 + \frac{\partial^2}{\partial \zeta^2}(\gamma - p_z)\right] - \frac{\partial^2}{\partial s^2}p_x + \frac{p_x}{\gamma}\left[\frac{\partial}{\partial s}\frac{\partial}{\partial \zeta}p_z + \left(\frac{\partial^2}{\partial s^2} - 2\frac{\partial}{\partial \zeta}\frac{\partial}{\partial s}\right)\gamma\right] = 0 \quad (2.20)$$

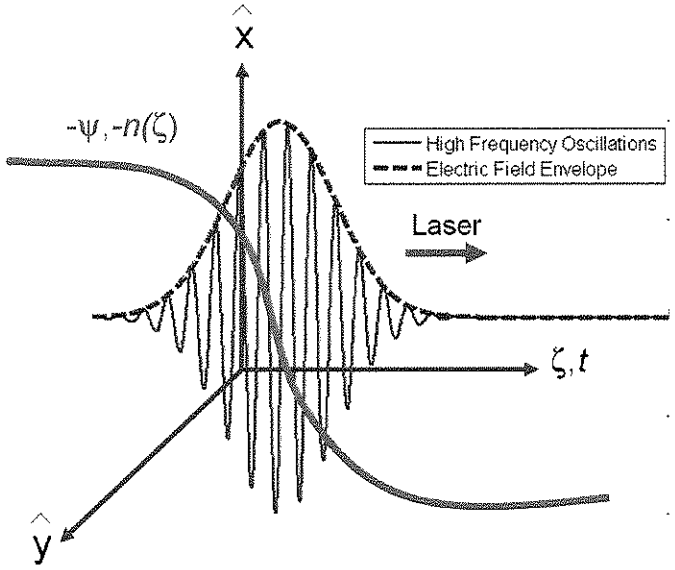

Figure 2.1: Short Laser Pulse coordinate axes illustration showing the laser pulse, envelope and wake.

$$\hat{z}\,\frac{\partial^2}{\partial\zeta^2}p_z+\frac{p_z}{\gamma}\left[1+\frac{\partial^2}{\partial\zeta^2}\left(\gamma-p_z\right)\right]-\frac{\partial^2}{\partial\zeta^2}\gamma+\frac{p_z}{\gamma}\left[\frac{\partial}{\partial s}\frac{\partial}{\partial\zeta}p_z+\left(\frac{\partial^2}{\partial s^2}-2\frac{\partial}{\partial s}\frac{\partial}{\partial\zeta}\right)\gamma\right]+\frac{\partial}{\partial\zeta}\frac{\partial}{\partial s}\gamma=0 \tag{2.21}$$

Pointing out the various scaling of the terms in the above equation. The fastest time scale is the laser frequency ω_0 which goes like $\frac{\partial}{\partial\zeta}$. The slow response is characterized by $\frac{\partial}{\partial s}$, which is on the time scale of the evolution of the laser pulse. Therefore, one can assume $\frac{\partial}{\partial\zeta} >> \frac{\partial}{\partial s}$. Recognizing this difference in time scales, equations 2.20 and 2.21 can be simplified by neglecting $\frac{\partial^2}{\partial s^2}$ and mixed terms as small. This forms the foundation for the quasi-static or frozen field approximation.

$$\hat{x}\;2\frac{\partial}{\partial s}\frac{\partial}{\partial\zeta}p_x+\frac{p_x}{\gamma}\left[1+\frac{\partial^2}{\partial\zeta^2}\left(\gamma-p_z\right)\right]=0 \tag{2.22}$$

$$\hat{z} - \frac{\partial^2}{\partial\zeta^2}(\gamma - p_z) + \frac{p_z}{\gamma}\left[1 + \frac{\partial^2}{\partial\zeta^2}(\gamma - p_z)\right] = 0 \tag{2.23}$$

Introducing χ, where $\chi \equiv \gamma - p_z = 1 + \phi - A_z = 1 + \psi$. Using $\gamma = 1 + p_z^2 + p_x^2$, so that $p_z = \frac{1}{2\chi}(1 + p_x^2 - \chi^2)$. Equations 2.22 and 2.23 can be written as,

$$\frac{\partial^2}{\partial\zeta^2}\chi + \frac{1}{2}\left(1 - \frac{1 + p_x^2}{\chi}\right) = 0 \tag{2.24}$$

$$2\frac{\partial}{\partial s}\frac{\partial}{\partial\zeta}p_x + \frac{p_x}{\chi} = 0 \tag{2.25}$$

Finally, we arrive at the familiar form of these equations by substituting the potential ψ and recognizing that in 1-d normalized units, from conservation of canonical momentum $\mathbf{P}$ that $a_x = p_x$.

$$\frac{\partial^2\psi}{\partial\zeta^2} + \frac{1}{2}\left[1 - \frac{1 + a_x^2}{(1 + \psi)^2}\right] = 0 \tag{2.26}$$

$$2\frac{\partial}{\partial s}\frac{\partial}{\partial\zeta}a_x + \frac{a_x}{1 + \psi} = 0 \tag{2.27}$$

Transforming back to real units, equation 2.26 has the following form,

$$\frac{d^2\psi}{d\zeta^2} = \frac{k_p^2}{2}\left[\frac{1 + a^2}{(1 - \psi)^2} - 1\right] \tag{2.28}$$

And a convenient form for the evolution of the vector potential of the laser pulse in time is,

$$\left(\frac{2}{c}\frac{\partial}{\partial\zeta}\frac{\partial}{\partial\tau} - \frac{1}{c^2}\frac{\partial^2}{\partial\tau^2}\right)a_\perp = k_p^2\frac{a_\perp}{1 + \psi} \tag{2.29}$$

,where τ=t.

Equations 2.28 and 2.29 form the basic building blocks for much of the nonlinear interactions described in this thesis.

2.3 Quasilinear nonlinear-optics of short pulse lasers

In this section, a physical picture of various phenomena based on quasilinear theory will be outlined in light of the quasi-static development in the previous section. To look at self-focusing will need to consider the transverse evolution. In the Lorentz gauge,

$$\frac{1}{c^2}\frac{\partial^2}{\partial t^2}\mathbf{A} - \nabla^2\mathbf{A} = \frac{4\pi}{c}\mathbf{J} \tag{2.30}$$

In the perpendicular direction,

$$\frac{1}{c^2}\frac{\partial^2}{\partial t^2}A_x - \frac{\partial^2}{\partial z^2}A_x - \nabla_\perp^2 A_x = \frac{4\pi}{c}j_x = \frac{4\pi}{c}\left(-env_x\right) \tag{2.31}$$

If the laser spot size $w_0 >> \lambda_o$ and the plasma is underdense $\frac{\omega_o}{\omega_p} >> 1$, we can rewrite the right hand side of Eqn. 2.31. Here,

$$\frac{4\pi}{c}\left(-env_x\right) = \frac{4\pi}{c}\left(\frac{-enp_y}{\gamma}\right) = \frac{4\pi}{c^2}\left(\frac{-e^2nA_y}{m\gamma}\right) \tag{2.32}$$

Here, we have used $\frac{p_y}{\gamma} = v_y$ and $A_y = \frac{ep_y}{mc}$. In unnormalized units, from the definition provided in the previous section, $n/\gamma = 1/\chi$. In the speed of light frame,

$$2\frac{\partial}{\partial\tau}\frac{\partial}{\partial\zeta}A_x - \nabla_\perp^2 A_x - \frac{\omega_p}{c^2}\frac{1}{\chi}A_x = 0 \tag{2.33}$$

To compare with Eqn. 2.29, in normalized units Eqn. 2.33 is,

$$2\frac{\partial}{\partial\tau}\frac{\partial}{\partial\zeta}a_x - \nabla_\perp^2 a_x = \frac{1}{\chi}a_x = -\frac{a_x}{1+\psi} \simeq -a_x\left(1-\psi\right). \tag{2.34}$$

From the assumptions above, the second time derivative (fast oscillation term) has been dropped. But, $\nabla_\perp$ has been included. This term will lead to transverse evolution of the laser pulse.

From Eqn. 2.26, $\frac{1}{1+\psi} \approx (1-2\psi+3\psi^2-4\psi^3...)$. We approximate a small wake $\frac{1}{1+\psi} \approx 1-2\psi$. This results in,

$$\frac{\partial^2}{\partial\zeta^2}\psi + \psi = \frac{A^2}{2}. \tag{2.35}$$

If we look for the evolution of the envelope of a laser pulse of the form $A = \frac{a}{2}e^{-i\omega_0\zeta} + c.c.$, Eqn. 2.26 can be rewritten as,

$$\left(\frac{\partial^2}{\partial\zeta^2}+1\right)\psi = \frac{|a|^2}{4}. \tag{2.36}$$

Historically, long pulses where $c\tau_{laser} >> \lambda_p$ are assumed in which the $\frac{\partial^2}{\partial\zeta^2}\psi << 1$, resulting in,

$$-2iw_0\frac{\partial}{\partial\tau} - \nabla_\perp^2 + \left(1-\frac{|a|^2}{4}\right)a = 0. \tag{2.37}$$

Here $\psi \approx \frac{|a|^2}{4}$ was used. Approximate 3D solutions for Eqn. 2.37 can be obtained through the method of source dependent expansion [66, 67] and through variational principle approach [10].

Another way to consider self-guiding and self-focusing is by considering the modification of the refractive index of the plasma by the laser pulse. The non-linear refractive index can be written in the form in which only the quasi-static

approximation is made. Here the nonlinear refractive index is,

$$\eta \simeq 1 - \frac{1}{2}\frac{\omega_p^2}{\omega_0^2}\left(\frac{1}{1+\psi}\right). \tag{2.38}$$

The form presented above in Eqn. 2.38 which is valid for highly nonlinear wakes will be considered later.

To make the physics more transparent, however, guiding will now be described assuming the existence of the wake. Self-guiding of laser pulses is possible when relativistically intense lasers produce plasma channels in which the radial profile of the refractive index, $\eta(r)$, exhibits a maximum on axis. Here $\eta = ck/\omega = \sqrt{1-\frac{\omega_p^2}{\omega^2}}$. This condition implies $\partial\eta/\partial r < 0$. As a high intensity laser pulse excites a nonlinear plasma wave, modifications resulting from radial variation of the relativistic factor $\gamma(r)$ and the radial density variation $n(r)$ lead to a nonlinear refractive index which can be written in the following form,

$$\eta(r) \simeq 1 - \frac{\omega_p^2}{2\omega_0^2}\frac{1}{\gamma(r)}\frac{n(r)}{n}. \tag{2.39}$$

Here n is the initial density. Since the relativistic electrons result primarily from the transverse quiver motion due to the laser electric field, $\gamma \simeq \gamma_\perp = (1 + a^2)^{1/2}$. Additionally, the variation in density can be expressed as $n(r) = n - \delta n(r)$. In the special case of weakly relativistic laser pulses $a_o << 1$, small density modulations $\delta n << n$ are produced so Eqn.2.39 can be written as,[14, 53],

$$\eta(r) = ck/\omega \simeq 1 - \frac{1}{2}\frac{\omega_p^2}{\omega_0^2}\left(1 - \frac{\langle a^2\rangle}{2} + \frac{\delta n}{n}\right). \tag{2.40}$$

Although Eqn. 2.40 is accurate only for weekly nonlinear lasers, the terms and therefore, the associated physics are represented independently. In Eqn.2.40, $\delta n/n$ is the self driven density depression and $\langle a^2\rangle/2$ is the refractive index change due to the relativistic mass corrections. Here $\langle a^2\rangle$ is the slow average (envelope)

of the vector potential. When a preformed density channel is used to guide the laser, an additional term $\Delta n/n$ is often added which represents the preformed radial density channel.

The radius of curvature of the wavefront of a laser beam as it focuses becomes larger until the phase front is a plane with infinite radius. This occurs at the focus. The spot size $w(t)$, defined as the radius $1/e$ of the electric field, then expands in time according to,

$$w\left(t\right) = w_0\sqrt{1+\frac{t^2}{\tau_R}}. \tag{2.41}$$

Here $\tau_R = \pi w_0^2/\lambda$ is the transverse spreading time and is the temporal equivalent of a Rayleigh length Z_R. Eqn. 2.41 can be differentiated twice to get the following equation of motion for the spot size in vacuum,

$$\frac{d^2}{dt^2}w(t) = \frac{4}{k_0^2}w(t)^3. \tag{2.42}$$

Here $k_0 = \omega_0/c$. Following the development of a simplified physical picture for self-guiding in a plasma, Mori was able to arrive at the same critical power for relativistic self-focusing P_c[53, 69, 49]. In this physical picture, the phase velocity at the radius $w(t)$ is faster (self-focusing) or slower (defocusing) than the phase velocity on axis. As shown in Fig. 2.2, if $d\eta/dr < 0$, the phase fronts tilt inward causing self-focusing to occur, since the pointing vectors associated with these fronts converge. An equation of motion which includes the effects of the radial refractive index channel can be written as,

$$\frac{d^2}{dt^2}w(t) = \frac{4}{k_0^2}w(t)^3 - \theta \simeq \frac{4}{k_0^2}w(t)^3 - \frac{\left(v_\phi(r=w) - v_\phi(r=0)\right)}{c}. \tag{2.43}$$

In this equation, the angle θ was assumed small so that $sin(\theta) \simeq \theta$. From Eqn. 2.40, the phase velocity can be written as,

$$v_\phi = \frac{c}{\eta} \simeq c\left[1+\frac{1}{2}\frac{\omega_p^2}{\omega_0^2}\left(1-\frac{\langle a^2\rangle}{2}+\frac{\delta n}{n}\right)\right]. \tag{2.44}$$

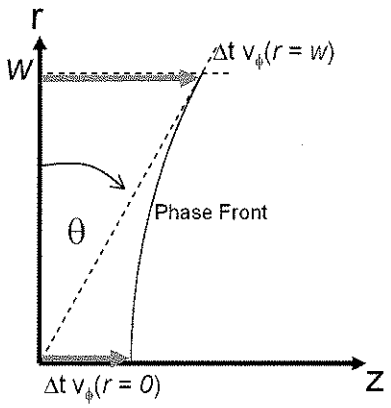

Figure 2.2: Physical picture of phasefront tilt caused by a radial dependence on refractive index

Plugging the phase velocities from Eqn. 2.44 into Eqn. 2.45 results in,

$$\frac{d^2}{dt^2}w = \frac{4}{k_0^2 w^3}\left[1 - \frac{1}{2}\frac{\omega_p^2}{\omega_0^2}\frac{k_0^2 w^2}{4}\left(\frac{\langle a^2\rangle}{2} + \frac{\delta n}{n}\right)\right]. \tag{2.45}$$

From Eqn. 2.45, it is clear that the right hand side must be negative if self-focusing is to occur. Since $w_0^2 a_0^2 \propto P$, this can be thought of as a power scaling. Allowing only for relativistic effects, one can solve for the critical power for relativistic self-focusing.

$$\frac{P}{P_c} = \frac{\omega_p^2}{\omega_0^2}\frac{k_0^2 a^2 w^2}{32}. \tag{2.46}$$

Here we have used the fact that $\langle a^2\rangle/2 = a^2/4$. Solving Eqn. 2.46 recovers the exact well known critical power for relativistic self-focusing P_c =17GW $\frac{\omega_p}{\omega_0}$.

Keeping only the density depression term in Eqn. 2.45 the following form can be written,

$$\frac{d^2}{dt^2}w = \frac{4}{k_0^2 w^3}\left(1 - \frac{1}{2}\frac{k_p^2 w^2}{4}\frac{\delta n}{n}\right). \tag{2.47}$$

Looking at Eqn. 2.47, by inspection the threshold for self-focusing (self-guiding) should be $\frac{\delta n}{n} \geq \frac{8}{k_p^2 w_0^2}$. A rigorous analysis of plasma channel guiding revealed that the true expression is[63, 62],

$$\frac{\delta n}{n} \geq \frac{4}{k_p^2 w_0^2}. \tag{2.48}$$

An image of the density wake excited using a laser pulse with an 11μm spot with a power $P/P_c = 1.2$ is shown in Fig. 2.3. The background density was 1.5 $\times 10^{19}$ cm$^-$3. The density wake is shown as a 2D slice of the 3D simulation in Fig. 2.3(a). The radial density depression is highlighted by plotting a slice of the depression shown in Fig. 2.3(a) in Fig. 2.3(b). From Eqn. 2.48, the required δn is 1.4$\times$10^{1}8 cm$^-$3, this is about 1 grid division of the plot. The density channel alone formed by such a pulse shows how effective self-guiding (self-focusing) is, even for pulses with powers only slightly above P_c.

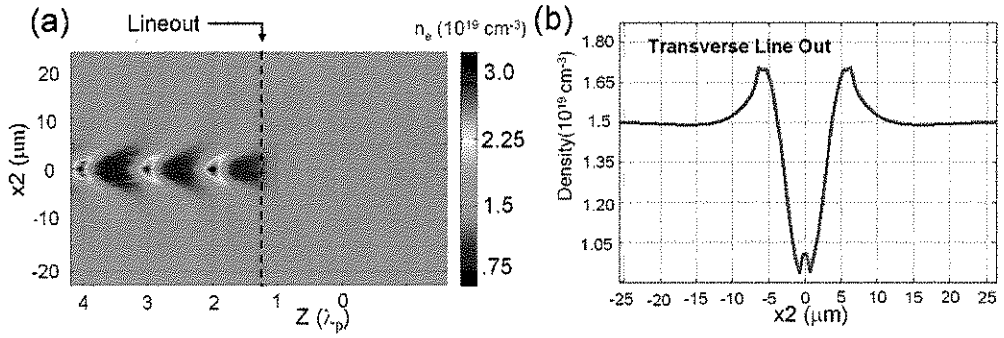

Figure 2.3: Fig.(a) shows a 2D slice from a 3D particle simulation. Fig.(b) is a plot of a lineout taken from the point indicated in (a)

2.4 Diffraction, Laser Head Erosion

In the late 1980s and early 1990s, the 1-D quasi-static theory was developed for laser produced wakefields. The major result of this theory was a set of equations which described both wake and laser evolution for underdense plasmas over a wide range of parameters as reviewed in earlier sections. In this section, some

applications of the theory will be discussed for the special case of ultrashort laser as well as interpretation. In many of the problems outlined in this section, analytic solutions are either not possible or too cumbersome to discuss. For these cases, numerical solutions will be presented.

From quasi-static Eqns. 2.26 and 2.27, Sprangle et. al. argued that self-guiding of ultrashort laser pulses ($c\tau \leq \lambda_p$) was not effective[65, 15]. Recognizing that Eqn. 2.26 can be expanded, in normalized units this becomes,

$$\frac{\partial^2 \psi}{\partial \zeta^2} = \frac{1}{2}[1 - (1 + a_y^2)(1 - 2\psi + 3\psi^2 - ...)]. \tag{2.49}$$

Making the approximation of a small amplitude wake, $|\psi| << 1$, Eqn. 2.49 was reduced to,

$$\frac{\partial^2 \psi}{\partial \zeta^2} - \psi = \frac{a^2}{2}. \tag{2.50}$$

It should be noted that the right hand side of Eqn. 2.50 represents the potential due to the oscillating laser field. Here $a_0^2/2 = \tilde{a}^2/4[1 - \cos(2\omega_0 \zeta)]$. The potential ψ can now be divided between the fast and slow terms $\psi = \psi_f + \psi_s$. Taking the derivatives of the fast response, it is easy to see that $\psi_f << \psi_s$. In terms of the slow response only, dropping the slow subscripts, we get the following form.

$$\frac{\partial^2 \psi}{\partial \zeta^2} - \psi = \frac{\tilde{a}^2}{4}. \tag{2.51}$$

Here the right hand side $\tilde{a}^2/4$ is noted as the ponderomotive potential. To solve Eqn. 2.51, ψ was given the form,

$$\psi = \int_{-\infty}^{\infty} G(\zeta, \zeta') a^2(\zeta') d\zeta \Rightarrow \int_{-\zeta}^{0} \sin(\zeta - \zeta') a^2(\zeta') d\zeta'. \tag{2.52}$$

Solving for a short laser pulse of the form $a_L = a_L 0 \sin(\pi \zeta / L)$ produced a wake of the following form in the limit of $L << \lambda_p$,

$$\psi = \left(\frac{a_L 0 k_p}{4}\right)^2 \left[\zeta^2 - 2\left(\frac{L}{2\pi}\right)^2 + 2\left(\frac{L}{2\pi}\right)^2 \cos(\frac{2\pi\zeta}{L})\right]. \tag{2.53}$$

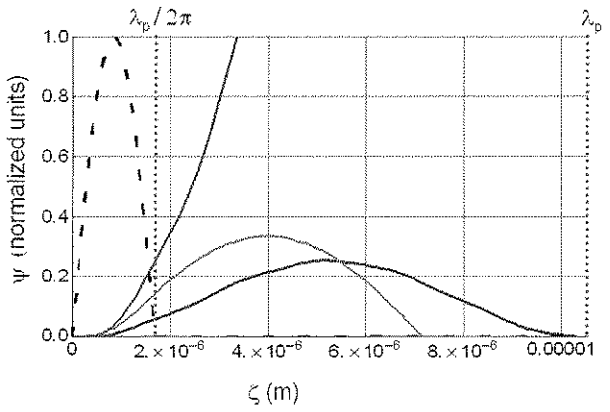

Figure 2.4: The dashed plot is the short pulse laser driver from Sprangle's 1990 Physical Review Letter[65]. The other curves are the wake response. The red curve is the analytic solution. The blue curve is the extreme solution for $L << \lambda_p$ as shown in Eqn. 2.53, and the green curve is a numerical solution to the fully nonlinear model.

In Fig. 2.4, the drive pulse is plotted along with the wake response. The green curve is the numerical solution to Eqn. 2.26 with the short length $\lambda_p/2\pi$ driver described above in dashed black. The red curve in the approximate analytic solution using the Green's function form descibed in Eqn. 2.52. The blue curve is the short pulse limit given in Eqn. 2.4. The plot size is one plasma wavelength. Refering to Fig.2.4, from Eqn. 2.48, the required $\Delta n/n = 0.452, 0.314, 0.231, 0.176, 0.139, 0.113, 0.093, 0.078$ for spots with $w0 = 5, 6, 7, 8, 9, 10, 11$ and 12 μm respectively and a plasma density of 10^{19} cm^{-3}. The largest trial spot size here will not be guided or focused until 1 μm into the pulse. This is in agreement with the assertion that short pulses can not be self-guided. Indeed, for very short pulses with $a_0 \leq 1$, this seems true. What this shows is that the wake response which is (by definition) slow, does not respond fast enough to allow for the building up of the refractive index channel necessary to guide the pulse.

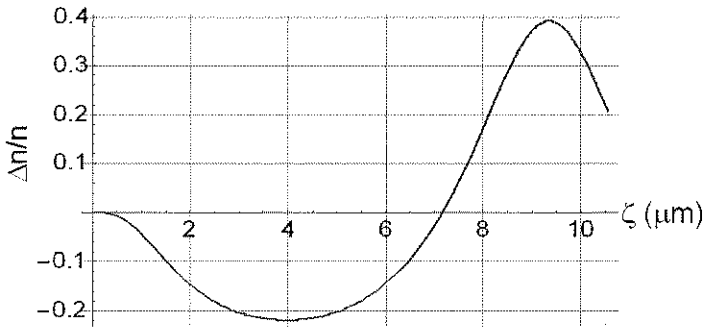

Figure 2.5: Normalized Density for a pulse driven using the truncated sin driver described above.

It was extrapolated, that the head of long pulses would experience diffractive erosion. From this analysis, an etch rate based on this diffraction was estimated as $v_{erosion} \simeq (\lambda_p/z_R) * c$, where $z_R = \pi w_0^2/\lambda$[65, 64, 72]. This basically, states that pulses in which $c\tau_{laser} \leq \lambda_p$ cannot be self-guided. Also, this conclusion is a result based only on 1d.

Assuming a 50 fs full-width-half-maximum (FWHM) gaussian laser pulse driver, numerical solutions to the 1d wake are shown in Fig.2.6. As the amplitude of the vector potential is increased, the amplitude of the wake (static potential) increases. Additionally, the front of the wake moves earlier. There are two reasons for this, the first is that a higher amplitude pulse excites a stronger wake which responds earlier. But, another way to think about this is that, the a given amplitude of the physical gaussian pulse moves earlier. The end result is that a much larger portion of the pulse can be guided as shown by the green dashed curve which assumes a w_o =5.5μm. The points where the green dashed curve crosses the wakes represent the point along the pulse where guiding and self-focusing begin. The lowest amplitude pulse, $a_0 = 1$, shows no guiding for this w_0. However, as the amplitude of the laser increases, the region where guiding

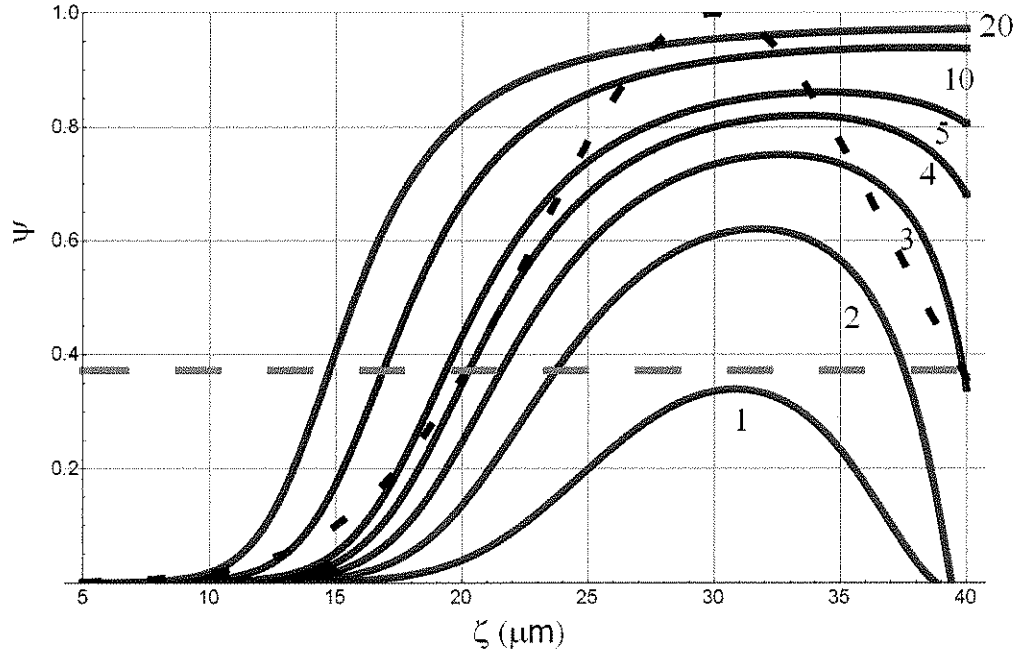

Figure 2.6: The various color curves represent 1d wakes driven by 50 fs full-width-half-maximum laser pulses with normalized vector potentials of 1, 2, 3, 4, 5, 10, 20. The black dashed curve is the normalized laser pulse driver. The green dashed horizontal line is the potential representing where guiding will occur for a 5.5 μm spot in a plasma with a density of 10^{19} cm^{-3}.

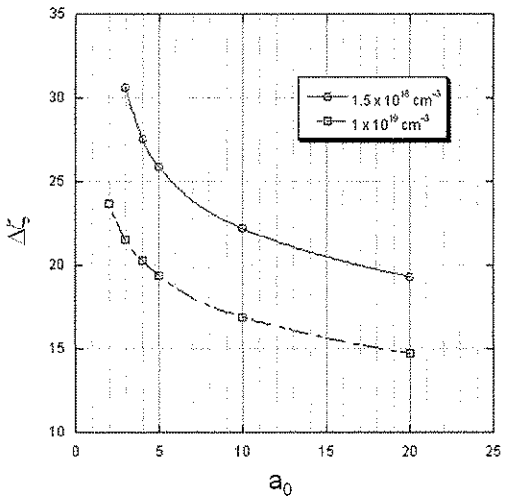

Figure 2.7: Plots showing the distance from the first $1/e$ in the pulse until the guiding condition is met as a function of laser pulse amplitude for a 55 fs laser pulse in plasma with densities of 5×10^{18} cm^{-3} and 1×10^{19} cm^{-3}.

occurs also increases. This also demonstrates how the effectiveness of self-guiding changes throughout the length of the short pulse. This was also pointed out by Sprangle[65]. Clearly the middle portion of the pulse is well guided for $a_0 > 2$.

A summary showing the distance in the laser pulse $\Delta\zeta$ until the guiding condition is met is shown if Fig. 2.7. These plots quantify the results shown in Fig. 2.6 for electron plasma densities of 5×10^{18} cm^{-3} and 1×10^{19} cm^{-3} and a w_0 of 5.5 μm which were the conditions for the experiments, described later. Both cases show that as the a_0 of the laser pulse is increased, the distance to the point where the guiding condition is met decreases. Comparing the two plots, the difference in $\Delta\zeta$ is relatively constant through out the range of a_0.

As mentioned earlier, the lack of guiding at the head of the pulse results in erosion. Essentially, the front of the pulse is unfocused and diffracts away. It should be noted that the longitudinal ponderomotive force on the electrons

pushes some electrons forward. In fully explicit particle codes, this appears as a bump in density ahead of the pulse. It was argued that the relativistic effects which would lead to self-focusing are almost exactly canceled by the increase in density of these fast electrons which is predominantly on axis[64]. As a result, the early portion of the pulse diffracts as if in vacuum.

2.5 Pump Depletion and Nonlinear Longitudinal Modulation of short pulses

As mentioned earlier, since ultrashort pulses are of interest in this paper, pulses where $c\tau > 2\lambda_p$ are not considered. As a result, longitudinal instabilities (such as laser hosing and Raman Forward Scattering which grow from the head of the pulse to the tail of the pulse) and which might normally inhibit, or otherwise add complexity to, propagation of longer laser pulses do not have the opportunity to grow for such short pulses. There are, however some very important nonlinear longitudinal effects which do need to be considered.

The two primary effects discussed here lead to changes in the shape of the pulse longitudinally and changes in the frequency of the laser pulse(which in turn lead to changes in the shape of the pulse). One way to understand these longitudinal effects is by considering the plasma as a refractive medium in which a wave moving close to the velocity of light is moving with the laser pulse. In an underdense plasma, the refractive index can be written as, $\eta \simeq 1 - n/2n_c$. Here n_c is the critical density of the plasma where the laser frequency is equal to the plasma frequency. The plasma wave (wake) can be thought of as a refractive index wave moving with the laser.

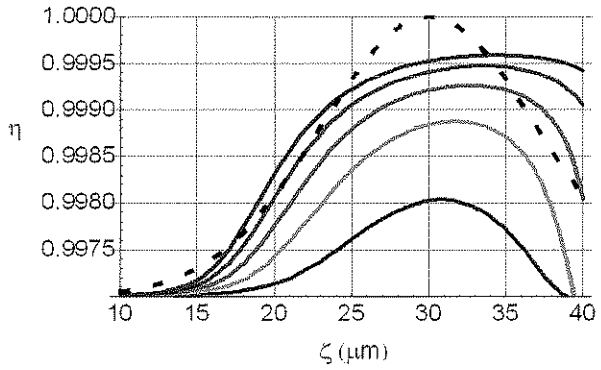

Figure 2.8: The axial refractive indices of plasma wave wakes as a function of $\zeta = z - ct$. The dashed curve is the normalized drive pulse. The red, orange, green, blue and purple curves correspond to the indices of wakes excited by drive pulses with amplitudes a_0 = 1,2,3,4 and 5 respectively.

2.5.1 Longitudinal Bunching

Consider the index of refraction for our examples from the previous section. Using the gaussian laser driver and the quasi-static approximation, a 1d wake solution was found numerically for several initial a_0. The index of refraction was calculated from Eqn: 2.38 and is shown in Fig. 2.5.1. Using this solution with the understanding that the frame is moving with velocity c, one can begin understand the fundamental nonlinearities which occur with time. One of primary nonlinear effects is longitudinal bunching in which the local group velocity $v_g = \eta c$ of photons traveling in a lower index (like those photons at the very front of the pulse) will move slower than those traveling in a higher refractive index (such as those traveling in the middle of the wake). The result is that photons bunch up in the density wake leading to an increase in intensity. One way to think about this, as described by Mori[53], is to consider two nearby locations along the traveling wave and compare the group velocities to get a local rate of bunching. The

distance between the locations is defined as ΔL and can be described by,

$$\Delta L = (v_{g2} - v_{g1})\Delta t. \tag{2.54}$$

As ΔL is decreased, the expression takes the form,

$$\Delta L = L\frac{\partial v_g}{\partial z}\Delta t = -\frac{L}{c}\frac{\partial v_g}{\partial \zeta}\Delta t, \tag{2.55}$$

or simply,

$$\frac{\partial L}{\partial t} = -\frac{L}{c}\frac{\partial v_g}{\partial \zeta}. \tag{2.56}$$

Referring to Fig. 2.5.1, which shows the indices of the wakes created by pulses with varying a_0. In all cases, the the local group velocity of photons in the front of the pulse is the linear group velocity given by $v_g = c\sqrt{1 - \omega_p^2/\omega_0^2}$. For higher a_0, since the magnitude of the wake is larger, the total change is refractive index is also larger, thereby increasing the effect of bunching. This effect also begins earlier in laser pulse with increasing a_0 since the wake builds up earlier as was shown.

2.5.2 Photon Deceleration and Pump Depletion

Photon acceleration and deceleration, as described earlier are the kinetic description of the photons traveling with the wake. As these photons shift in wavelength(frequency), their associated group velocity changes causing them to move faster (from blue shifting) with respect to unshifted photons (acceleration) or alternatively (from red shifting) slower (deceleration). The rate of this wavelength shift is given by,

$$\frac{1}{\lambda}\frac{\partial \lambda}{\partial t} = -\frac{1}{c}\frac{\partial v_\phi}{\partial \zeta}. \tag{2.57}$$

In terms of frequency, the rate of change is

$$\frac{1}{\omega}\frac{\partial \omega}{\partial t} = \frac{1}{c}\frac{\partial v_\phi}{\partial \zeta} = -\frac{1}{c\eta^2}\frac{\partial \eta}{\partial \zeta}. \tag{2.58}$$

A plot of $\partial\eta/\partial\zeta$ vs. ζ is shown in Fig. 2.9 for 50 fs FWHM pulses with peak

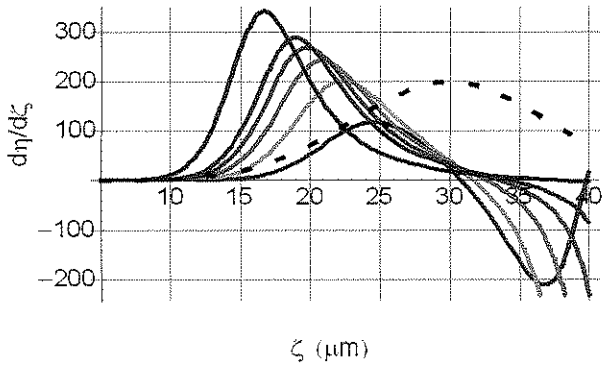

Figure 2.9: Plot of the rate of change of the refractive index of wakes driven by 50 fs lasers pulses. Peaks of a_0 of the laser driver were 1, 2, 3, 4, 5 and 10 which correspond to red orange green blue, purple and dark purple respectively. The dashed black curve shows the normalized $a(\zeta)$ envelope of the laser pulse.

a_0 ranging from 1 to 10. From Eqn. 2.58, the rate of change of the local laser frequency is proportional to the rate of change of the refractive index with ζ. In

Fig. 2.9, the frequency modulation early in the pulse increases with increasing a_0. Also the peaks (which represent the largest local change in frequency) move earlier in the pulse with increasing a_0. As the laser frequency shifts locally to lower frequencies, these regions shift backward in the pulse because the these photons have a relatively lower group velocity v_g. This is termed photon deceleration[53].

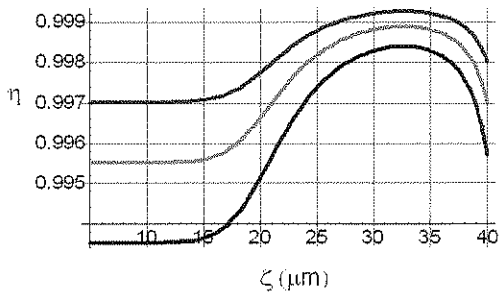

Figure 2.10: Refractive index of a wake created by 50 fs FWHM gaussian pulse with an $a_0 = 3$ for the wavelengths of 0.8 μm 1.0 μm and 1.2 μm shown in blue, orange and red (respectively)

Fig. 2.10 shows the indices of the wake for 3 different wavelength (0.8, 1.0 and 1.2 μm). These correspond to wavelengths commonly seen in experiment and 3D PIC simulations. Also, the separation between these curves is greatest early in the pulse where plasma density is the highest and therefore the dispersion is highest. As a result the photon deceleration effect tends to bunch up the photons at the front. This increases the local laser amplitude which can lead to steepening in the front as these early red shifted photons slip back. These effects have been seen in simulations simulations[60, 27, 40]. As a result, this also leads to pulse shortening, in addition to longitudinal bunching and diffraction at the head of the pulse. Additionally, it should be noted that the contribution to the laser potential is higher for these photons, since the ponderomotive force, which initially pushes

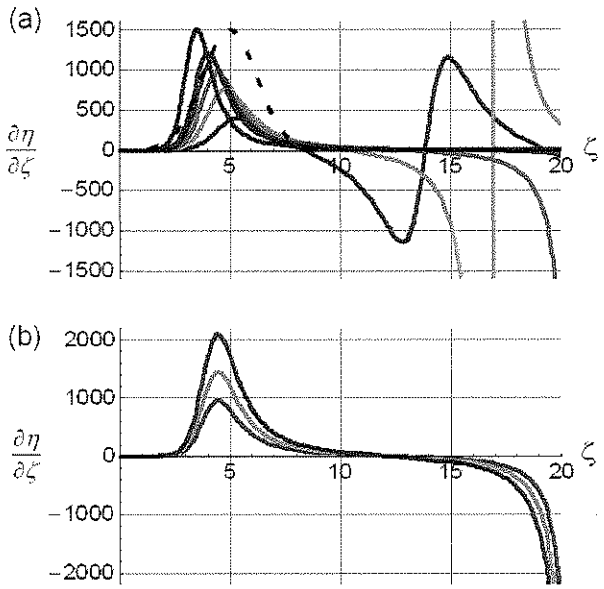

Figure 2.11: (a) The rate of change of the refractive indices of wakes excited by short pulses with $c\tau = \lambda_p/2$ and peak a_0 of 1,2,3,4,5 and 10 which are plotted in red, orange, green, blue, purple and dark purple respectively. The normalized contour of the laser pulse is shown in dashed black to show the relative location and width of the laser pulse. (b) The rate of change of the refractive indices of wakes excited by the a short pulse with $c\tau = \lambda_p/2$ and a peak a_0 of 3 for wavelengths 0.8, 1.0 and 1,2 μm shown in blue, orange and red respectively.

the electrons forward and radially, $F_p \propto \lambda$.

Now consider a shorter pulse, one that has, for example, evolved but remained gaussian. Plots of the change in the refractive index with ζ are shown in Fig. 2.11(a). The rate of change with ζ has now increased dramatically when compared to Fig. 2.9. For example, the laser pulse with a peak a_0 of 3 resulted in a peak $\partial\eta/\partial\zeta$ of 250 when a 50 fs pulse was used as shown in Fig. 2.9. This compares to a peak $\partial\eta/\partial\zeta$ of $\sim$1000 when an 8.5 fs pulse was used as shown in

Fig. 2.11(a). As a result the photons in the front are shifting and hence slipping back at a much faster rate. This effect is further amplified once the pulses have shifted red as shown in Fig. 2.11(b). The blue curve is the index for a wavelength of 0.8 μm and a_0 of 3 and is the same as the green curve in Fig. 2.11(a) with a peak of 1000. The orange curve is the change in index for a wavelength of 1.0 μm and the red is the change in index for a wavelength of 1.2 μm. This shows that as the wavelength shifts to longer wavelengths, it continues to shift at an even faster rate. With respect to self-guiding, these red-shifted photons also can be guided in a smaller wake.

Until now, only the frequency(wavelength) shifting of photons have been considered with no direct consideration of the pulse energy. In a preformed underdense plasma, it is assumed that the number of photons are conserved. With respect to energy, as the photons loose energy through red shifting, the wake gains energy. These photons are exciting the wake in the process. So far, it has been shown that pulses with higher a_0 transfer energy at a greater rate than lower a_0 pulses and this energy transfer occurs earlier in the laser pulse. Additionally, the transfer of energy to the wake is more efficient for shorter pulses with the same peak a_0. And, finally, the transfer of energy to the wake is higher for lower energy photons. This process of transfer of energy becomes more localized to the front of the laser pulse with increasing a_0. It has been shown by Decker and Mori through a combination of theory simulation and physical insight that, if the laser pulse is short and intense, that the localized energy transfer from the laser pulse to the wake causes the laser pulse to "deplete" its energy in that region [9]. The physical process for this in 1D is that the lasers ponderomotive force F_p pushes electrons forward. These electrons form a density spike with a width of ΔL which moves with the laser pulse if the laser pulse has an $a_0 > 1$. This localized depletion causes the front of the laser pulse to etch backward. An estimate of the etch

velocity is given as,

$$v_{etch} \simeq \frac{\Delta L}{\Delta \tau} \simeq \frac{\omega_p^2}{\omega_0^2} c. \tag{2.59}$$

Here $\Delta\tau$ is the time required to completely "Deplete" the laser energy within the density spike.

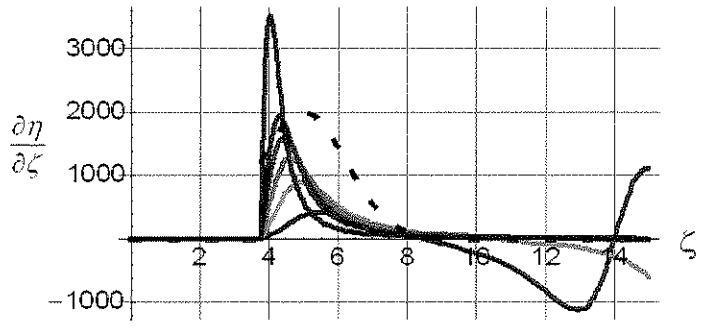

Figure 2.12: Plots of the refractive indices of plasma wakes excited by short laser pulses with peak a_0 of 1,2,3,4,5 and 10 shown in red, orange, green purple and dark purple respectively which have a sharpened (step) front.

As the pulse depletes locally, it forms a very steep front. In the work by Decker and Mori[9], the resultant pulse was approximated using a step at the front. In Fig. 2.12, the refractive index model shows that this steep pulse indeed depletes rapidly and with the highest rate. Comparing the $a_0 = 3$ curve in green in Fig. 2.12 to the short pulse green curve in Fig. 2.11, there is a 20% increase in the peak rate of pump depletion, however, the dark purple, which represents an a_0 of 10, from the two figures shows an increase of ~100%. The rate of energy transfer increases with pulse steepening.

From the Eqn. 2.59, we get the nonlinear phase velocity of the wake. This is the linear group velocity minus the velocity of the etching at the head of the

pulse.

$$v_f \approx 1 - \frac{1}{2}\frac{\omega_p^2}{\omega_0^2} - \frac{\omega_p^2}{\omega_0^2} = 1 - \frac{3}{2}\omega_p^2\omega_0^2. \tag{2.60}$$

This etch velocity was later verified in 3D. And a rough range over which this rate is valid was found to be $2 < a_0 < 2\sqrt{\omega_0^2/\omega_p^2}$[41].

As an aside, one can see here the application to accelerators. For a trapped electron moving with velocity c, the electron, self-trapped in the rear of the 1st nonlinear plasma wavelength will be accelerated until it outruns the wave. The total distance where the electron continue to be accelerated is known as the dephasing length and can be estimated by,

$$L_{dp} \approx \frac{c}{c - v_f}\lambda_w \approx \frac{2}{3}\frac{\omega_0^2}{\omega_p^2}\lambda_w. \tag{2.61}$$

Of course Eqn. 2.61 assumes that nonlinear pump depletion at the head of the pulse is the only loss to the laser pulse.

Finally, the total length a laser pulse can continue to drive a strong wake is known as the pump depletion length and is given by,

$$L_{pd} \approx \frac{c}{v_{etch}}c\tau \approx \frac{\omega_p^2}{\omega_0^2}c\tau \tag{2.62}$$

After a distance L_{pd}, the front of the pulse has etched through the pulse.

2.6 Self-Guiding and Electron Blowout

The term blowout regime, as described in recent publications, refers to the case where an ultrashort relativistically intense laser pulse creates a region where the electron density is nearly 0 in the first plasma wave (wake) period. The idea of electron cavitation through ponderomotive blowout from a laser pulse was first

recognized in a paper by Sun et. al.[69]. In this paper, a region of complete electron cavitation was theorized for laser pulses with powers greater than P_c. In this theory, the laser pulses were short enough to assume that the ions were fixed. As a result, this condition on blowout has relevance for very short pulses.

Recently, a phenomenological theory was developed which can be applied to electron drivers and ultrashort short laser pulses $c\tau < \lambda_p$ in the blowout regime[38, 39, 41]. In this theory, electrons are blown out radially by the lasers ponderomotive force F_p. In 3D, the equation of motion for a cold plasma driven by an intense laser pulse can be written[51],

$$\frac{d}{dt}\mathbf{P_i s} = q_i \left(\mathbf{E_s} + \frac{V_s}{c} \times \mathbf{B_s}\right) + \mathbf{F_p} \tag{2.63}$$

The ponderomotive force is described as,

$$\mathbf{F_p} = -\frac{q_i^2}{\hat{\gamma}_i m_i c^2} \frac{mc^2}{e} \nabla \left|\frac{a^2}{2}\right|. \tag{2.64}$$

Here $\hat{\gamma}_i = (1 + \frac{P_i^2}{m^2c^2} + \frac{|a^2|}{2})^{\frac{1}{2}}$. The terms here denoted with the subscript s, represent the slow time scale terms associated with the quasi-static approximation as described earlier. Using this basis of force balance, Lu was able to find a solution for the wake potential ψ in terms of the blowout radius as well as defining the blowout radius R_b in terms of the laser driver.

In much of the theory presented in previous sections, a 1D quasi-static model was used. Here, by contrast, a fully 3D model has been developed. This theory applies to laser pulses which are much shorter than the first plasma period $c\tau \sim \lambda_p/2$ and with $2 < a_0 < 5$. As we show in simulation and experiment, the laser parameters, used in the experiment do not begin with parameters which fit this theory. Theory, as described in the previous sections shows that laser pulses

which begin with a peak $a_0 > 1$ and a length approximately λ_p will shorten through a combination of diffraction at the head, longitudinal bunching, and photon deceleration (acceleration). This longitudinal evolution eventually results in a pulse which does fit into this theory and creates a clear blowout.

The condition for self-guiding in an underdense plasma was given in Eqn. 2.48. An estimate for guiding condition in the case of complete cavitation (or blowout) can be obtained by allowing $\delta n/n = 1$. The requirement on guiding reduces to $k_p w_0 > 2$. It can be shown that in order to create a well defined ion channel in which a narrow electron sheath surrounds the ion channel, the laser pulse spot size must be chosen to match the radius of the ion channel, $w_0 \simeq R_b$[38, 39, 40, 41]. This is because the radial extent ponderomotive force of the laser pulse extends only to approximately the laser spot size. The blowout radius R_b is determined from the balance of the radial forces of the ion column $E_r = k_p R_b$ and transverse laser ponderomotive force $F_{p\perp} \sim k_p \nabla a_0^2/\gamma \sim a_0/(k_p w_0)$. Equating these provides an estimate of the matched spot size, $\frac{1}{\gamma_0}\frac{a_0^2}{k_P W_0} \sim k_p w_0$. For $\gamma \approx a_0$, this yields,

$$k_p R_b \simeq k_p w_0 \simeq 2\sqrt{a_0} \tag{2.65}$$

Here, an exact result could not be found. As a result the factor of 2 in Eqn.2.65 was determined from simulation. This, however is only the condition for self-guiding in the blown-out region. In this region the density of the plasma $n_e \sim 0$, and so the laser pulse residing in the ion column does not significantly evolve. As a result, the interaction primarily happens at the front of the laser.

2.7 Highly Nonlinear Self-Guiding

Although, recent phenomenological theory can explain the wake response to the propagation of an ultra-intense pulse $a_0 > 2$ under certain conditions, the very front region of the laser pulse, where the laser is not as intense and where it is interacting with the plasma electrons can not be understood from this theory. The blowout regime, however, exemplifies the conditions where local pump depletion occurs. In 3D, the transverse ponderomotive force leads to a larger $\delta n/n$ than was found in the 1D cases[41, 9].

Since the laser itself is creating its own guiding structure, there must be some portion of the head of the pulse where the guiding does not occur. As explained earlier, Sprangle et. al. estimated this distance as λ_p[65], which was later refined to a plasma skin depth by Esarey[14] resulting in a head erosion rate of $v_{erosion} \simeq ((c/\omega_p)/z_R) * c$. This estimate neglects any dependence on a_0 shown numerically in previous sections.

In the work by Decker and Mori[9], a suggestion that self-guiding short pulses might be possible in the case where the head of the laser pulse was depleted before diffracting. More recently an estimate by Lu[40, 41] on the threshold where diffraction could be entirely mitigated by pump depletion allowing for self-guided propagation of short laser pulses was found by considering the 1D index of refraction from Eqn.2.38 and 1D quasi-static wake Eqn. 2.26. Here $1 - \frac{1}{1+\psi} \simeq \psi = \frac{4}{(k_p w_0)^2}$. For $|\psi| << 1$, which is the case early in the laser pulse, a first order approximation of Eqn.2.26 can be made giving,

$$\frac{\partial^2 \psi}{\partial \zeta^2} \simeq -\frac{k_p^2}{2} a^2. \tag{2.66}$$

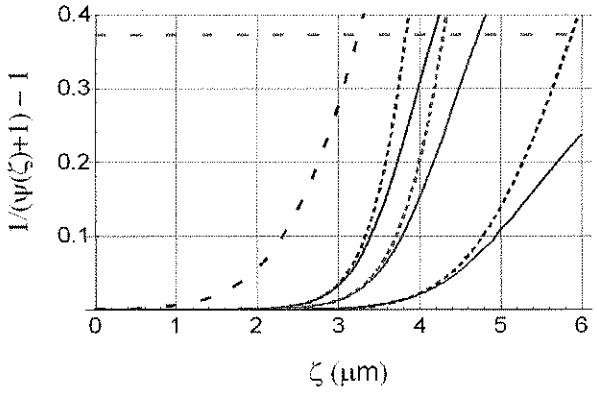

Figure 2.13: A series of curves showing the actual (solid) and 1^{st} order estimate (dotted) of the wake potential. The horizontal orange dashed line is the necessary condition where guiding begins for a w_0 of 5.5 μm in a plasma with density 10^{19} cm^{-3}. The wakes effect on the refractive index $\frac{1}{1+\psi(\zeta)} - 1$ is plotted for wakes excited by short $c\tau = \lambda_p/2$ pulse with a_0 of 1, 3 and 5 (red, green and blue). The dashed black curve is the normalized envelope of the laser pulse.

As can be seen in Fig.2.13, this provides a reasonable approximation early in the laser pulse but in this case diverges from the actual solution before reaching the threshold for guiding indicated by the orange dashed line. Additionally, one can see that as the amplitude of the laser pulse increases, this approximation approaches the numerical solution at the point where the threshold for self-guiding begins. Assuming the length of the laser pulse lost to diffraction is a skin depth, the loss to the head of the pulse due to diffraction each Rayleigh length Z_R scales as $(k_p a_0^{3/2})^{-}1$. An approximation of the distance from the front of the laser pulse to the point where the wake provides a sufficient index of refraction for guiding $\Delta\zeta$ based on the linearized wake can be estimated as $\Delta\zeta \approx \left(k_p^2 w_0 a_0\right)^{-1} \sim \left(k_p a_0^{3/2}\right)^{-1}$. $v_{etch}/c \simeq \frac{3}{2}\frac{\omega_p^2}{\omega_0^2} \approx \frac{\Delta\zeta}{Z_R}$. This leads to requirement for guiding on the pulse intensity given by,

$$a_0 > \left(\frac{\omega_0^2}{\omega_p^2}\right)^{\frac{1}{5}} \propto \frac{1}{n^{1/5}} \tag{2.67}$$

According to the above requirement the laser intensity a_0 is weakly dependent on the inverse of the density.

2.8 Designing a Self-Guiding Experiment

To determine the conditions necessary for self-guiding, one needs to apply the theory developed so far in this chapter. Start with conditions for the blowout regime. First, the laser pulse length should be on the order of a plasma wavelength, $c\tau_{laser} \sim \lambda_p$. Here, a 50 FWHM laser pulse has a length of 15μm. For the laser pulse to be between $\lambda_p/2$ and $2\lambda_p$, the experimental density should range from 1.3×10^{18} cm^{-3} to 2×10^{19} cm^{-3} respectively. Given a laser power of 10 TW, (500 mJ, 50 fs), a further limitation must now be put on the density to maintain

a power above $P_c = 17\frac{n_c}{n}$ GW. Here n_c is the critical density. For the case of a laser with a wavelength of 815 μm, $n_c = 1.68\times10^{21}$ cm^{-3}. The critical factor $P_c =$ 10 TW at a density n_e of approximately 3 $\times10^{18}$ cm^{-3}. For a $P/P_c = 1$, (density of 3 $\times10^{1}$8 cm^{-3}), using the conditions for matched guiding from Eqn.2.65 and the definition for P_c from Eqn.2.46, a matched a_0 can be determined,

$$\frac{P}{P_c} = \frac{\omega_p^2}{\omega_0^2}\frac{k_0^2 a_0^2 w_0^2}{32} \rightarrow \frac{a_0^2 k_p^2 w_0^2}{32} \rightarrow \frac{a_0^2(4a_0)}{32} \rightarrow \frac{a_0^3}{8} \tag{2.68}$$

We can now write a_0 as,

$$a_0 = 2\left(\frac{P}{P_c}\right)^{\frac{1}{3}} \tag{2.69}$$

For $P/P_c = 1$, a_0 should be 2. Next, the matched spot size, in this case is $w_0 = 2 \times \sqrt{a}/k_p = 8.7$ μm. To meet the necessary criteria on intensity given in Eqn.2.67, an $a_0 = 3.5$ is required.

2.9 Comparison Between Theories

In this section a comparison between some leading theories will be presented with respect to pump depletion and loss mechanisms of the laser pulse. In the LWFA community, there are three prevailing theories for determination of the pump depletion length based on energy loss of the laser pulse. Additionally, the laser may erode away due to diffraction.

In Fig. 2.14, several plots are presented which show the length limitations of high intensity laser pulse propagation with respect to the plasma density n_e. The green, red-dashed and blue curves are the pump depletion lengths given by the 1D nonlinear[14], 3D nonlinear[40, 41] and 3D highly nonlinear[26] respectively. All these plots assume a 55 fs laser pulse. The other plots assume a loss rate dominated by diffraction at the head of the pulse. These plots correspond to pulses with lengths of 30, 50 and 100 fs and are shown in blue-green, orange-

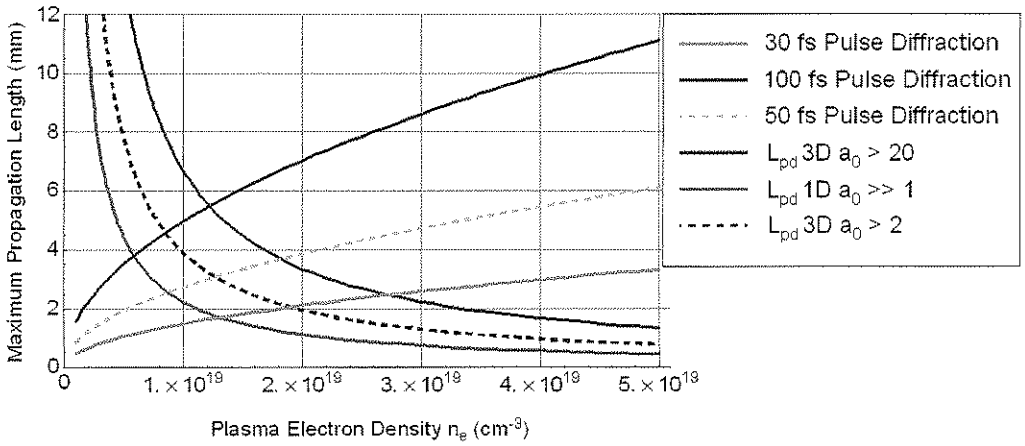

Figure 2.14: Curves showing short laser pulse loss mechanisms according to several theories

dashed and blue respectively. The dashed curves correspond to pulse lengths close to the experimental conditions. Here these plots assume initial an initial spot size of 5.5 μm with an initial a_0 of 1.7.

The formula used to plot the diffraction dominated curves was,

$$L_{diffraction} \approx \left(\frac{\omega_p}{c}\right) Z_R c\tau. \tag{2.70}$$

The formula for the highly nonlinear $a_0 > 20$ case, developed through the application of similarity theory to laser wakefields by Gordienko and Pukhov is[26],

$$L_{pd} \approx a_0 \frac{\omega_0^2}{\omega_p^2} \omega_p \tau. \tag{2.71}$$

The 1D formula used here was[14]

$$L_{pd} \approx \frac{a_0}{3} \frac{\omega_0^2}{\omega_p^2} \omega_p \tau. \tag{2.72}$$

The 3D nonlinear $2 < a < 20$ formula used in Fig. 2.14 which was given by Lu was[40]

$$L_{pd} \approx \frac{\omega_0^2}{\omega_p^2} \omega_p \tau, \tag{2.73}$$

which is independent of a_0.

Referring to Fig. 2.14, the most striking aspect of these theories is that pump depletion and head diffraction scale trend in opposite directions with respect to density. If one considers only the case of matched spot guiding in which the spot is always matched to the corresponding density, the curves all trend the same way (that is down with increased density). As there is reason to assume this requirement, the plot of diffraction dominated loss is shown as in Fig. 2.14.

CHAPTER 3

Simulations

With todays advances in parallel computing power, the role of simulations has evolved to the level where fully 3 dimensional simulations of real experiments are possible. This new development has had a profound impact over the past 10 years in the field of plasma accelerators. Indeed, it could be argued that many of todays fastest computers were developed for plasma physics simulations.

Since, simulations presented here are very close to the parameters of real experiments, several diagnostics have been developed which mimic experimental diagnostics. By looking at these simulation diagnostics in conjunction with all the additional information one gets from simulation data, we can use these simulations to more readily interpret experimental results. This also allows for very close comparisons between simulations and experiment.

To simulate plasma based acceleration, kinetic models are required. This is especially true when highly nonlinear wakes are excited. The particle-in-cell (PIC) algorithm handles this nonlinear physics quite naturally by reducing the problem to the microscopic level where only the equation of motion and Maxwell's equations need solving[8]. In the PIC algorithm, a spatial grid is setup. The electromagnetic fields are distributed on the grid much in the same way as is the case when using finite difference algorithms. The grid spacing must be such that the smallest spatial features of interest are resolved. At the first time step, using the field distribution of the grid, the charged particles within the grid are

	n_e (10^{18} cm^{-3})	τ (fs)	w_o (μm)	L (mm)	P (TW)	$\frac{P}{P_c}$
1. LPHD	15	50	11.2	2	2.1	1.3
2. HPHD	20	60	18	1	6	4.2
3. HPLD	4	50	6	4.6	10	1.4
4. HPM	7	50	6	4.6	10	2.4

Table 3.1: A summary of the 4 PIC simulations presented. The acronyms LPHD, HPHD, HPLD and HPM have been used to represent Low Power High Density, High Power High Density, High Power Low Density, and High Power Matched respectively.

pushed around by solving the equation of motion on a time scale Δt, which is the characteristic timescale of the simulation. This results in new positions and momenta of the particles which become the initial conditions for the next step. The new charge density (or current density) interpolated on to the grid results in new fields which are distributed on the grid according to Maxwell's equations. The simulation evolves for as many steps as are needed.

The simulations presented in this section are fully explicit 3D simulations launched with help from the UCLA plasma simulation group, using the PIC code OSIRIS[21]. Results presented in this chapter focus on the relationship between wake formation, self-guiding, pump depletion and energy balance. It should be noted that these the simulations do not include the effects of ionization as this feature was not available.

The cases presented follow the evolution of the wake and laser pulse in four distinct cases. In all cases, some self-guiding is observed when compared to vacuum diffraction of the laser pulses.

In, Table 3.1, a summary of the four sets of simulation parameters is presented. The parameter space for the simulations represent four cases of short pulse laser propagation in a plasma. By understanding these four cases presented in these simulations aids understanding our experimental results. The propagation of short laser pulse in each of these cases will be related to the nonlinear description provided in the theory section of this thesis.

The degree of nonlinearity of interaction of a laser pulse in an underdense plasma is a function of power with respect to the critical power for relativistic self focusing P/P_c and the vector potential a_o of the propagating laser pulse. We have seen already in the theory section that, for $a_o > 1$, as the vector potential increases, the wake forms earlier and that this creates a larger wake with a larger $d\psi/d\zeta$. A faster rise time and larger wake (larger ψ) indicates a larger transfer of energy to the wake. In this section, we look at the transverse and longitudinal nonlinear effects associated with this wake and how the degree of the nonlinearity affects self-focusing and self-guiding through the use of new simulation diagnostics, some of which mimic experimental diagnostics, and some which take advantage of the details that are observable only through simulations.

3.1 Transverse Evolution of the Laser Pulse

The analysis software used this section essentially takes an image of the energy distribution in the forward direction. This is what is seen when using a charge coupled device(CCD) camera since each pixel on the camera is sensitive to the energy integrated over the capture duration. Likewise, for a direct comparison(shown later), the raw Osiris data must be presented in units which can be measured. Initially, the simulation provides data about the laser in the form of a transverse electric field. The analysis code first squares the electric field, than

integrates in the z direction of the entire Osiris data box for each x-y grid spacing. This essentially results in a "pixel" or simulation "quant" with units of energy. It is assumed that since the box is actually a spatial representation (the camera is a temporal integration), the laser pulse does not significantly evolve over the course of traversing that small space. The resulting image is shown below in figure 3.1. The curves shown along the image show an integrated sum (white), a narrow box out taken through the peak of the intensity(green and yellow), and finally, the red dashed curve is a nonlinear least square fit to a gaussian of the green or yellow lineout. The spot size measurements (from experiment and simulation) are taken from the $1/e^2$ (radius) of the fitted curve.

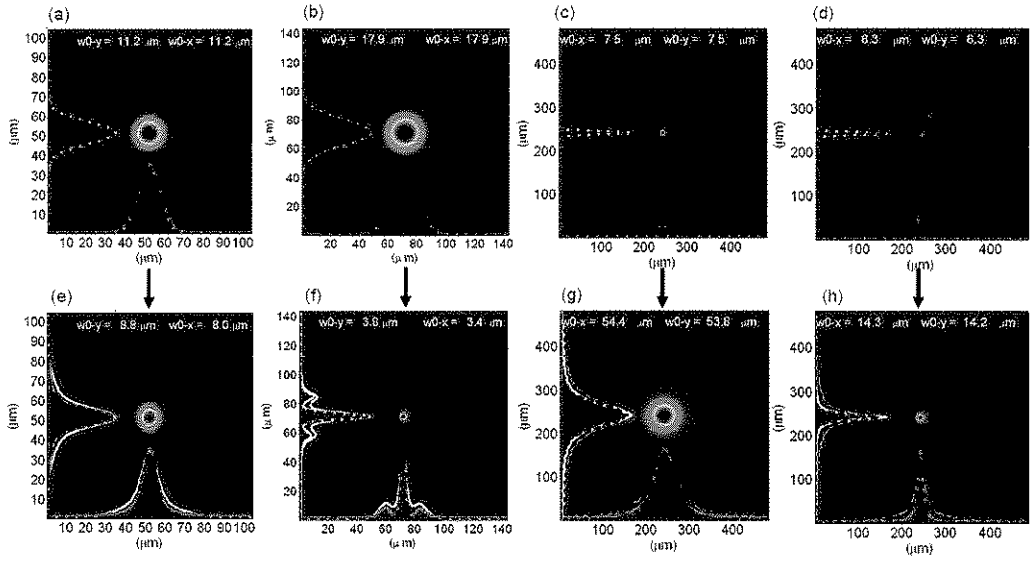

Figure 3.1: Images laser spot at the initial focus of the laser pulse and the end of simulation.

In Figs. 3.1,(a)-(d) the initial focused spot image is shown. In Figs. 3.1(e)-(h) the corresponding spots at the end of the simulation are shown. Here, referring to the simulation parameters, Figs. 3.1(a) and (e) are from the $n_e = 1.5 \times 10^{19}$

cm^{-3} simulation. Figs. 3.1(b) and (f) are from the $n_e = 2 \times 10^{19}$ cm^{-3} simulation. Figs. 3.1(c) and (g) are from the $n_e = 4 \times 10^{18}$ cm^{-3} simulation. Figs. 3.1(d) and (h) are from the $n_e = 7 \times 10^{18}$ cm^{-3} simulation.

Comparing the initial symmetric 11.2 μm spot in Figure 3.1(a) with Figure 3.1(e), the spot size after 2 mm of propagation or ~4 Rayleigh Lengths $Z_r = \pi w_0^2/\lambda$, determined from the red fitted curve, has decreased to 8 μm along x and 8.8 μm along y. This is to be expected, since the initial spot size w_o is large compared to the plasma wavelength λ_p and blowout radius R_b, but with power $P > P_c$, self focusing occurs. This guiding, however, is imperfect. Comparing the curves along the side the images, in Figure 3.1(a), all the curves lie on top of each other. When this is the case, all the energy of the laser pulse resides in the spot. This is always the case for the initial (gaussian) spot. In the corresponding figure 3.1(e), however, the white curve along both axes has broadened while the green, yellow and red curves have narrowed. Since the white curve represents the entire sum along each axis, this difference indicates that a portion of the laser pulse has not been guided. This is to be expected since, in this case, P/P_c is only slightly greater than 1, and since the initial spot size is large, this results in an $a_o = .8$. Consequently, the nonlinear wake builds up more slowly than would be required to guide the entire pulse as explained in the theory section.

Comparing the initial spot and spot after only 1 mm of propagation, Figures 3.1(b) and (e) reveal a dramatic change. The initial 17.9 μm is reduced to only 3.4 μm. Here, $n_e = 2 \times 10^{19}$ cm^{-3} with $P = 6$TW. This results in $P/P_c \approx 4 >> 1$ since both the density n_e and the laser power are greater than that of the previously discussed results. The family of curves shown reveal that, even in this case, not all the energy was propagated in the focused spot.

The last two sets of figures are from the L = 4.6 mm simulations. Each

of these simulations also has a $200\mu m$ ramp in density. Here Figures 3.1(c) and (g) are with $n_e = 4 \times 10^{18}$ cm^{-3} while Figures 3.1 (d) and (h) are with $n_e = 7 \times 10^{18}$ cm$^{-}3$. Although both simulations begin with $P = 10$TW. The important parameter P/P_c is 1.4 and 2.4 respectively for the lower and higher n_e cases. In the low density case, although $P/P_c > 1$, significant diffraction still occurs. This happens since the self-focusing forces cannot fully balance the diffraction forces since $w_o < w_m$, where w_m is the matched spot size, resulting in a large spot of $54\mu m$ as discussed earlier. The forth case presented in Figures 3.1(d) and (h) is very close to the matched case given as $k_p w_o \approx 2\sqrt{a_o}$. Here, the change in spot size varies from the initial spot by a factor of two over a distance of 4.6 mm (or 32 Z_R). Again, in these cases comparing the red, white and yellow/green curves reveals that the guiding was not perfect. In later sections, an effort will be made to explain why and where the guided pulse looses energy.

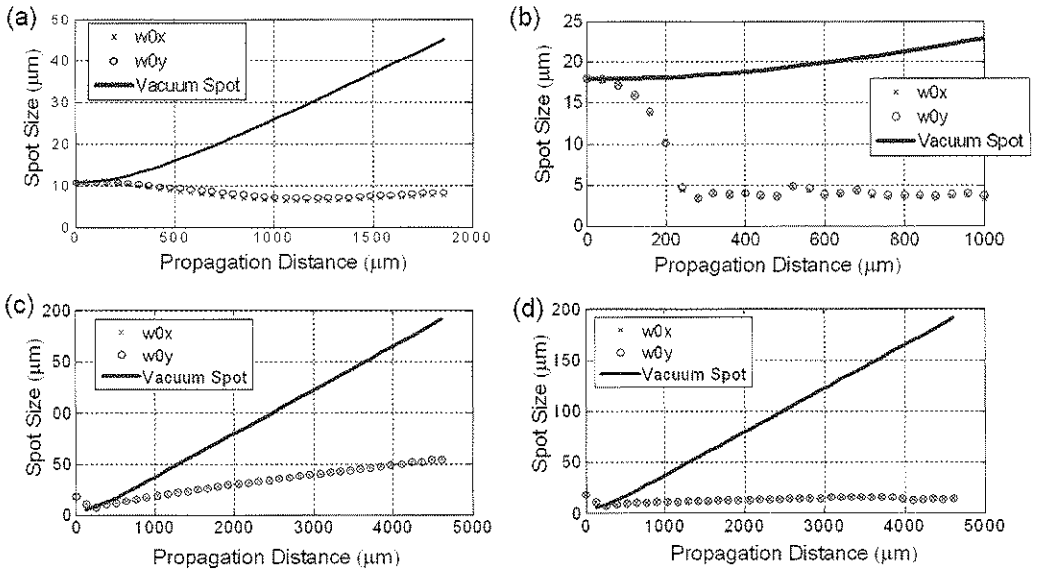

Figure 3.2: Spot size vs. Propagation Distance Z

In Figure 3.2, the spot size $w(z)$ determined from the $(1/e^2)$ red curve of

the above images is plotted for each of the simulations described above. Also plotted for each case is the spot size for the case of vacuum diffraction $w(Z) = w_o(1 + Z^2/Z_R^2)$. Here, all simulation results show a decrease in diffraction from the vacuum case. In Figure 3.2(a), simulation 1 (as described in the table above), $w_o > w_m$, and since P/P_c is only slightly larger than 1, the spot is weakly focused reaching a "waist" spot size of 6.5 μm after propagating $\sim$ 1.3 mm. In later sections, we will see that in this case, the front of the laser pulse could not be self-guided and was continuously eroded due to diffraction.

In Figure 3.2(b) simulation 2 (as described in the table above), $w_o > w_m$, however, here $P/P_c >> 1$. Early in the propagation, the spot dramatically self-focuses from w_o of 18.9 μm until it reaches an equilibrium at $\sim$3.5μm. From this point it propagates as a matched spot with relatively little variation throughout the remainder of the simulation. Here, although, the initial spot size was large, the focusing force was strong enough to guide a 3.7 μm spot. For this spot size $Z_R \approx 50\mu m$ which propagates for $\sim$750 mm or $\sim$ 15 Z_R. The calculated matched spot size for the initial parameters is $\sim$3 μm, however this matched spot does not consider evolution of the laser pulse. Since $P/P_c >> 1$, significant longitudinal compression in addition to self-focusing may result in an increase in power. This in turn would lead to an increase in R_B and therefore w_o.

In Figure 3.2(c), which corresponds to simulation 3, $w_o < w_m$, here $P/P_c = 1.4 > 1$. Here we see that the diffraction forces cannot be fully compensated by the focusing forces. The initial $w_o \approx 7$ μm grows at a constant rate, but which is slower than that of vacuum diffraction through the full extent of the simulation.

Finally, in Figure 3.2 (d), which corresponds to simulation 4, $w_o \approx w_m$. Although the spot grows slightly, the spot size does not fluctuate considerably. In this case, $Z_R \approx 141$ μm based on the initial 6 μm focus, so the propagation

distance of 4.6 mm corresponds to 32 Z_R.

3.2 Spectral Analysis of the Propagating Laser Pulse

The physical mechanisms responsible for the nonlinear modulation of the spectrum for a relativistically intense, but ultrashort laser pulse have been discussed in detail in the theory section. Many simulation papers extract physics from the spectrum of a lineout through the center of the electric field of the pulse. In these simulations, physical mechanisms such as blue shifting (photon acceleration) and red shifting (photon deceleration or pump depletion) have been identified. Additionally, this process has allowed for in depth study in to the photon kinetics by using diagnostic tools like the Wigner transform which can follow the evolution of photons longitudinally. Here, however, we present images in which the modulation of the spectrum is a function of radius.

For the case of a bi-gaussian profile, the on-axis vector potential a_o is greatest. The wake builds up earliest on-axis resulting in the density channel which guides the laser pulse. As a result, photons residing near the axis would be expected to demonstrate the greatest spectral modulation.

In each of the figures presented in this section, the spectral image presented is of the sum along x and ζ of the entire box. This diagnostic also allows for representation of the image produced by summing only a range of x. This latter process is similar to introducing a "slit" as on an imaging spectrograph. Images taken this way will be used later to compare simulation and experimental results. What is presented here is not exactly analogous to opening the slit on a spectrograph, since the spectral resolution of the simulation relies upon the ratio of sample points per distance d and is therefore limited by the Nyquist sam-

pling criteria which essentially requires a minimum of 2 sample points to resolve a wavelength. In an experiment, the slit width, grating spacing, camera pixel size, optical setup, and optical alignment all play a role in the overall resolution of the spectrometer. Images in this section show an image of the entire energy spectrum, since in simulation, the "slit" can be opened entirely without compromising spectral resolution. Here the spectrum has been obtained using the Fast Fourier Transform and is presented after multiplying the conjugate resulting in a power spectrum.

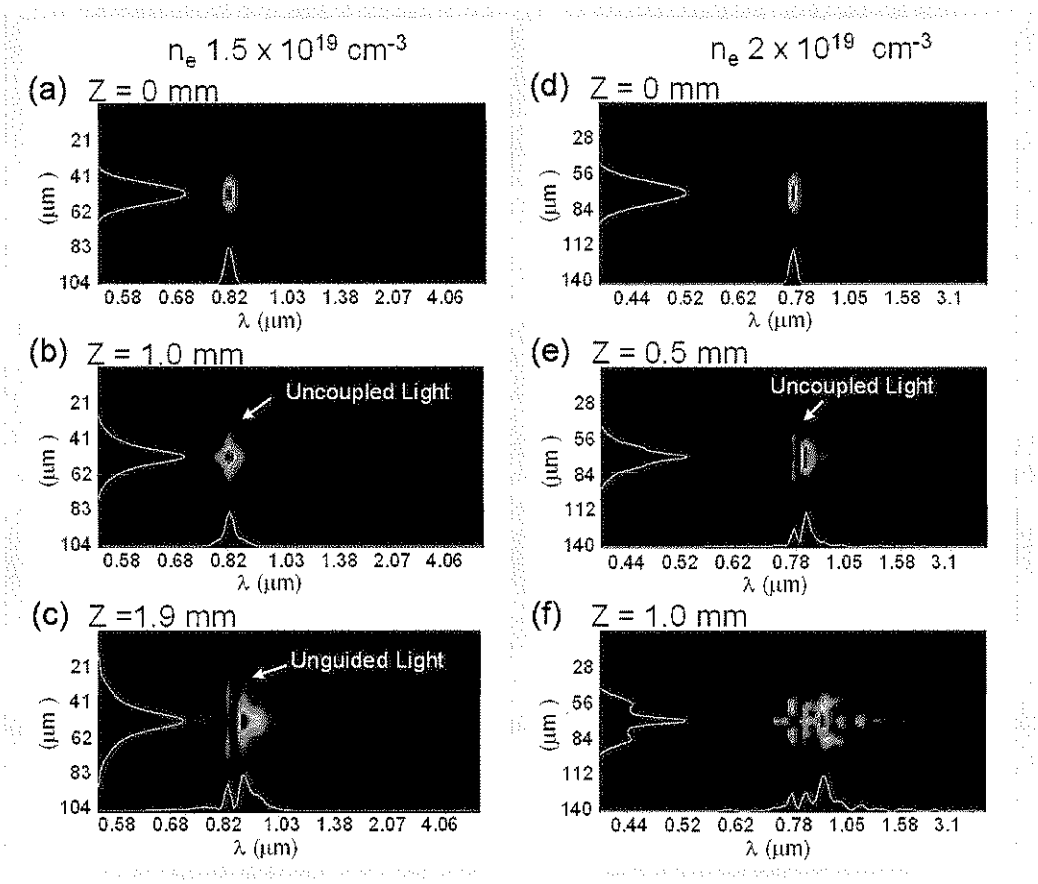

Figure 3.3: Spectral images of the laser pulse from the 1.5×10^{19} cm^{-3} density and 2×10^{19} cm^{-3} simulations.

In Figure 3.3, the imaged spectra are presented from simulations 1 and 2 as described in Table 3.1. Figures 3.3 (a) - (c) show the spectral evolution of the laser pulse from simulation 1 while Figures 3.3 (d) - (f) show the spectral evolution of simulation 2. The white curve along the side of each image is the sum over λ and provides approximately the same information as the white curve along the side of the spot images in Figure 3.1. The white curve along the λ axis is the spatial sum and represents all the spatial sum of the power spectrum.

In Figures 3.3 (a) and (d) show the spectral image of the initial spot. In all simulations, the initial central wavelength was 0.8 μm as seen by looking at the white λ curve. Figure 3.3 (b) shows simulation 1 after 1 mm of propagation. The pulse modulation in this case is relatively weak as P/P_c is only sightly greater than 1. However, from this image, the unguided light is seen as the diffracted feature which is relatively unshifted. This light is "uncoupled" and therefore unaffected by the relativistic plasma wave. This uncoupled light is lost and can be seen as the spreading of the spatial sum. Figure 3.3 (c) shows simulation 1 after 1.9 mm of propagation. The blue shifted light on axis comes from interaction with the back of the wake (photon acceleration). Additionally, a new diffracting feature is seen. This feature must come from the front of the laser pulse, since it is red shifted and the pulse length $\tau \sim \lambda_p$, where here $\lambda_p = 2\pi c/\omega_p$. This feature shows preliminary evidence for diffraction at the head of the pulse. Finally, looking at the balance of red shifted vs. blue shifted light indicates that the pulse is loosing energy as it propagates.

In simulation 2, $\tau > \lambda_p$, this complicates the interpretation of the spectral image. That being said, there are similarities in spectral features between the two simulations. In Figure 3.3 (e), although z=500 μm into the plasma, a great deal of spectral modulation is present, but is confined to a small region. This spatially

narrow broadband feature represents the self-guided portion of the laser pulse which is residing in a large amplitude plasma wave. Referring to Figure 3.2 (b), it should be noted that by this point in the simulation, the pulse has self-focused from an initial spotsize of 18.9 μm to 3.7 μm. Again, the uncoupled feature is present. This feature diffracts slowly, however, since w_o is large. Finally, Figure 3.3 (f) shows a highly modulated spectrum with large portion of the total energy on axis. Here again, the broad spatially narrow feature is present.

In Figure 3.4 (a) - (f), the evolution of simulation 3 is shown as a function of propagation distance Z. In Figure 3.4 (g) - (l), the corresponding evolution of simulation 4 is shown. Here the yellow curve along the spatial axis is a sum of the spectrum. The white curve along the λ axis gives the spatial sum. Each white and yellow curve have been individually normalized.

In, simulation 3, recalling that $P/P_c \approx 1.4$, but that as $w_0 < w_m$ self-guiding (self-focusing) could not occur. In moving from Fig. 3.4 (a) - (b) a spatial distance of 1 mm, the beginnings of spectral modulation are seen. As large portion of the pulse has shifted red to greater than 0.81 μm and blue shifted tail appears. This is a result of initially setting up a large amplitude wake due to the large $a_o > 3$ at focus. Again moving from (b) to (c) (z = 2 mm), the pulse has slightly shifted red and blue, but has also grown in size resulting in a smaller a_o which drives a smaller wake as described earlier. Referring to Figs. 3.4 (d) - (f), it is noted that the spectral modulation has saturated by 2 mm. This results from the inability to self-guide and therefore maintain a highly nonlinear wake.

Lastly, the spectral evolution of simulation 4, wherein $w_0 \approx w_m$ is shown in Figs. 3.4(g)-(l). These figures are analogous to the corresponding Figs. 3.4(a)-(g), although it should be noted that the spatial scales differ.

In this case, evidence for driving a strong wake throughout the plasma is seen.

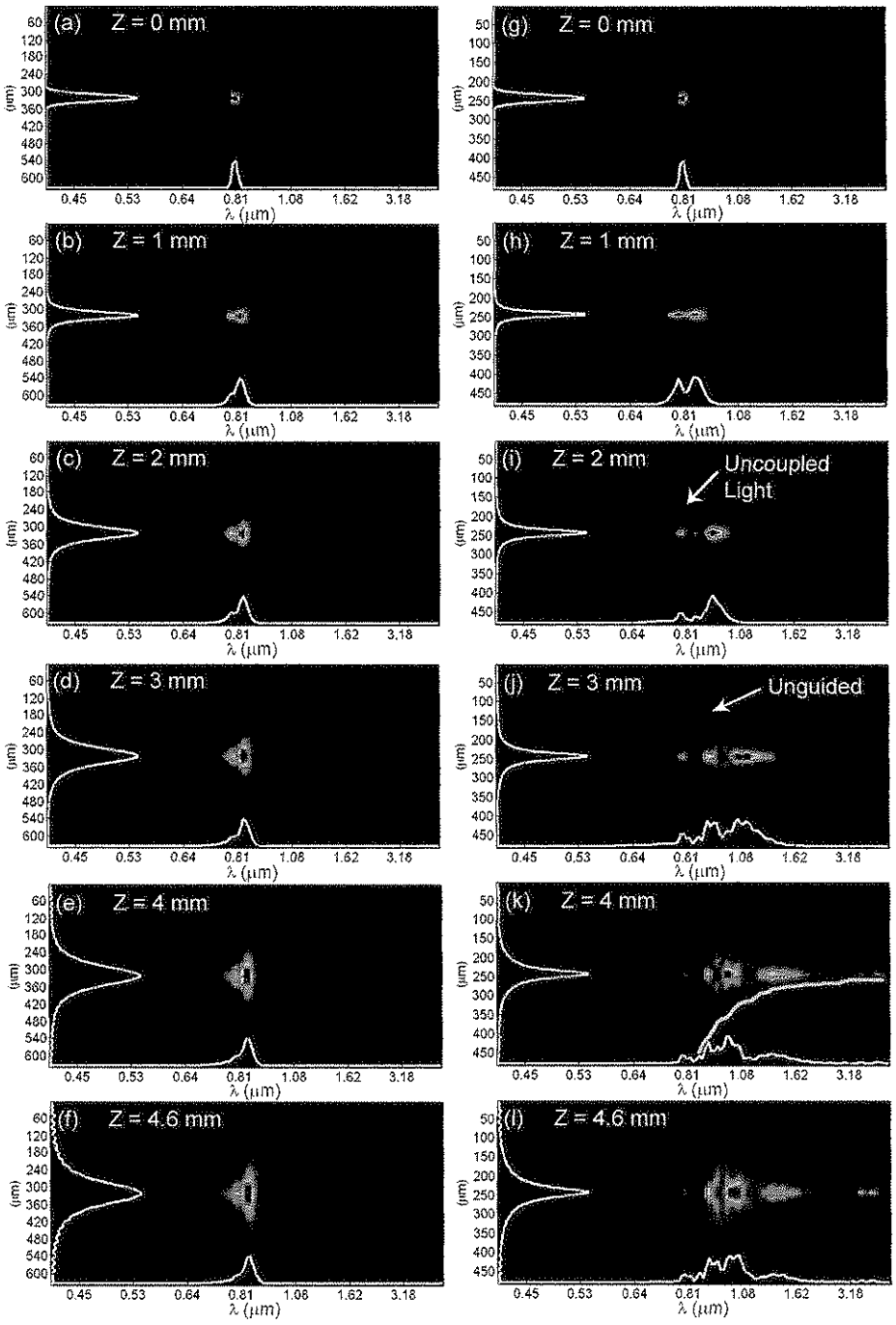

Figure 3.4: Spectral images of the laser pulse from the 4×10^{18} cm^{-3} density and 7×10^{18} cm^{-3} simulations.

Indeed, from the density data (shown later) there is a large amplitude wake. After 1 mm of propagation, blue shifting occurs since the laser pulse length $c\tau \sim \lambda_p$, so the back of the laser pulse initially interacts with the density spike at the back of the first period. This blue shifting continues until the pulse has shortened so that the photons at the back of the pulse, no longer interact with the wake. This occurs at approximately, 3 mm of propagation.

After 2 mm of propagation, the uncoupled light can be seen as the diffracting, but unshifted feature Fig. 3.4(j). As the pulse evolves longitudinally, some portion of the front the pulse, which has a local power which is lower than P_c can not be guided. This is seen as unguided light in Fig. 3.4 (j). After this initial evolution Fig. 3.4 (k), the portion of the light which was unguided in (3) continues to diffract, but as the light shifts red, less light is diffracting. This continuous red shifting acts as a kind of time stamp, which helps in interpretation of experimental results.

3.3 Laser Pulse Energy Loss Mechanisms

In this section, an attempt will be made to understand the relationship between the energy loss and self-guiding. We have seen already seen evidence for diffraction at the head of the pulse from the forward spot images combined with the imaged spectra. Here an attempt is made to quantify, in terms of the initial energy, what portion of the laser energy is diffracting compared to the portion that is self-guided. Additionally, a third loss mechanism will be identified as coupling loss. This has also been seen in previous sections as the energy lost in the initial evolution of the pulse before reaching a steady self-guiding state.

Plots of energy vs. propagation distance are shown in Fig. 3.5. The individ-

ual plots (a) through (d) correspond to simulations (1) through (4) respectively. The blue dashed curve is the energy of the laser pulse U_{pulse}. This energy was derived from the transverse electric field of the laser pulse. The process can be described as $U_{pulse}(z) \propto \int_X \int_Y \int_\zeta d\zeta dY dX \left(E(z)_y^2\right)$. Since the transverse boundaries in OSIRIS are not yet absorbing, the electric field energy is conserved even if the pulse expands to the size of the transverse box. The plots shown have all been normalized to the initial energy of the laser pulse. To get the energy in the self-guided pulse, first the guided pulse has been defined as pulse described by the red curves along the sides of Fig. 3.1, which are the gaussian fits of the green lineouts. From these x and y gaussian fits, a new virtual spot was created (without normalization), which essentially represents the self-guided spot. Finally, the same process described above to get U_{pulse} was again performed on the virtual spot to obtain the energy $U_{guided}(z)$ which was also normalized to the initial virtual spot energy. Of course, since the initial pulse was approximately a pure gaussian, $U_{guided}(z = 0) = U_{pulse}(z = 0)$. The green curves in Fig. 3.5 represent the energy of the laser pulse assuming conservation of photon number. In this case, the white curve along the bottom of the spectral images shown in Figs.3.4 and 3.3 which represents the spectral content of the total energy was used to find the average photon energy $U_{h\nu}(Z)$. This energy should scale with the total energy of the pulse as it propagates through the plasma. Assuming conservation of photon number, the total energy deposited in the plasma $T_{wake}(Z)$ can be written simply as, $T_{wake}(Z) = U_{pulse}(Z = 0) - U_{pulse}(Z)$.

From simulation 1, where $w_o >> w_m$, $P/P_c \simeq 1$, and $a_o = .8$ the total energy loss is less than 3% shown in Fig. 3.5(a). The fraction of the guided pulse which initially looses energy showed no nonlinear interaction with the wake seen in Fig.3.3 (b), is again shown here as the sharp decrease of guided energy. After a distance, this curve begins to show a smaller loss. In this case, that is primarily

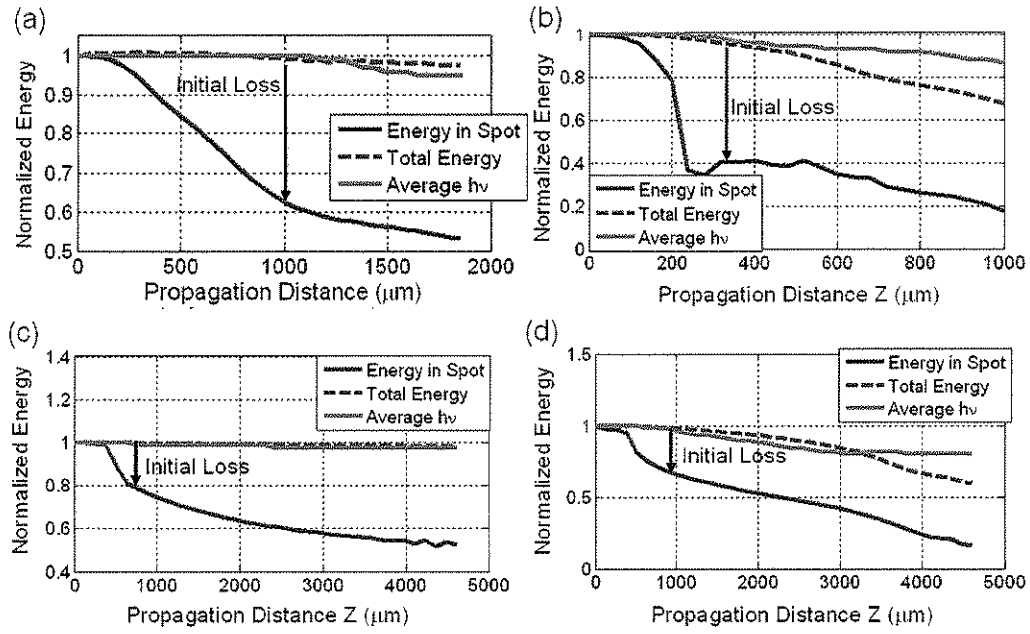

Figure 3.5: Plots of Energy, Guided Energy, and Energy Determined from Spectrum vs. Propagation Distance for the 4 Simulations

due to the fact that the pulse begins to grow in size again as seen in Fig.3.2 (a), thereby reducing the loss in energy when compared to portion of the pulse which is diffracting. Nevertheless, the self-guided portin of the laser pulse has lost nearly half its initial energy after 2 mm. The spectral energy calculation, shown here (green curve) agrees relatively well with the energy calculated by summing the field (blue curve).

From simulation 2, however, where $w_o >> w_m$ and $P/P_c \approx 4$, the dramatic self-focusing of the initial laser pulse seen in Fig.3.2 (b) occurs for only about 40% of the initial pulse energy as shown in Fig. 3.5 (b). One explanation for this is that the pulse length $c\tau > \lambda_p \approx \lambda_w$, so, a density variation with a period of λ_p results in defocusing regions (laser sausaging). Since the initial spot size is so large, another explanation could be that the wake build up near the outer radius of the pulse was too slow, as a result, only the center of the pulse self-guided. The total laser energy after propagating 1 mm was ~70%, compared to ~20% of the self-guided portion. The spetral calculation diverged after ~400 μm of propagation.

Simulation 3, Fig. 3.5 (c), did not self-guide well as was shown in Fig.3.2 (c). As a result, the method outlined above simply finds the energy which is diffracting at a slower rate (red curve). In any case, the initial loss is greater as in Fig. 3.5 (a) and (b).

In the nearly matched case of simulation 4, Fig. 3.5 (d) shows that the guided portion initially looses about 25% of the energy before leveling off. This is considerably less than the initial loss seen in (a) or (b). Here, since the spot is close to matched, the initial loss may come from the front portion of the laser pulse which cannot be initially self-guided. The total laser energy after 4600 μm (blue curve) was ~60%. This compares with only ~20% of the initial energy in the guided spot

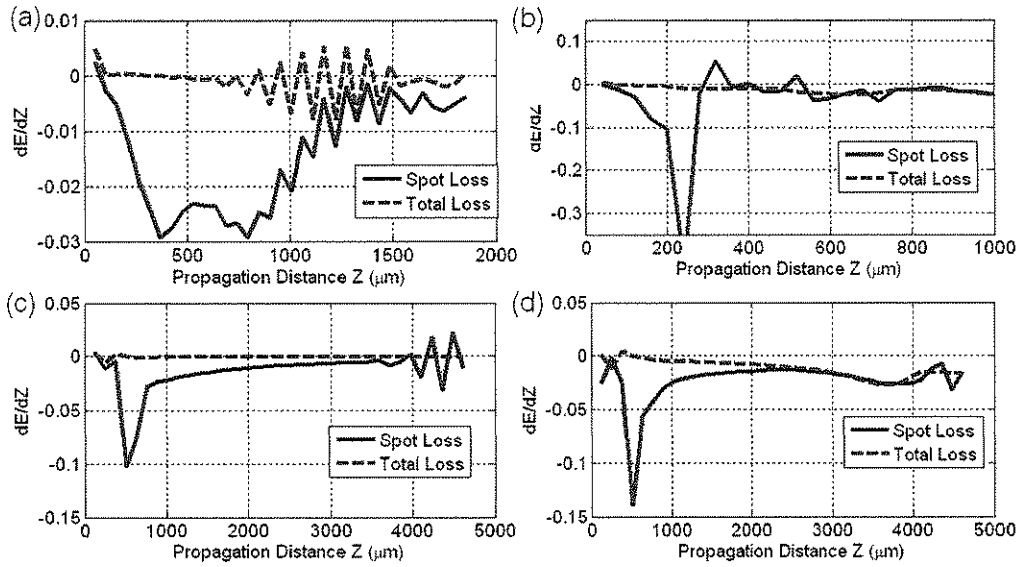

Figure 3.6: The Derivative of the Energy vs. Propagation Distance

(red curve). The majority of the energy loss in the spot was lost in the first 500 μm of propagation. The spectral calculations for the energy diverged significantly at about 3000 μm (green curve). Future efforts will be made to explain this.

The plots in Fig.3.6 show the rate of energy loss dU/dZ of the laser pulse and the self-guided portion. These plots give further insight into whether or not the pulse is efficient self-guided or losing energy due to diffraction. Additionally, these plots help to discriminate coupling loss which occurs while the pulse is evolving and is present in each of the 4 figures (a) through (d), as the initial dip in the red curve. The blue curve is the change in total pulse energy.

For perfect self-guiding to occur, the self-guided laser pulse should only loose energy to the wake. This happens when the rate of energy loss of the total laser energy, which only occurs due to giving energy to the wake, is the same as the energy loss of the self-guided pulse. The difference between the total laser energy loss and the energy loss of the self-guided portion results from two primary

physical processes. The first is coupling loss as described above. The second is diffraction at the head of the pulse during propagation.

Figure3.6 (a), which correlates to Fig. 3.5 (a) and is from simulation 1, is an example of poor self-guiding. The rate of total energy loss is very low. It should be noted that the uneven features seen in both curves starting at 750 μm and ending at 1500 μm result from small high frequency numerical variations which have been amplified by taking the derivative and are not believed to represent any real physical processes. Here, the red curve indicates that the self-guided spot is loosing energy at a higher rate than the total energy. This indicates that, in this case, diffraction at the head of the pulse is the dominant loss mechanism in the self-guided spot.

In Figure3.6 (b), we see that after the initial coupling loss which occurred during the period of rapid self-focusing, the self-guided portion of the pulse settles into a state where the rate of total energy loss is the same as the rate of energy loss from the self-guided portion. In other words, the self-guided portion is not loosing any energy to diffraction. The only loss mechanism of the self-guided pulse after $\sim$300 μm is pump depletion. Additionally, the rate of change of the energy is relatively constant as would be predicted from theory for a pulse in the ultra-relativistic blowout regime[9].

Even in the low density case, there is a coupling loss. The initial dip in the red curve in Figure3.6 (c) signifies that even though in this case where diffraction is not fully balanced by self-focusing, the "self-guided" portion of the pulse experiences a significant loss early. The term "self-guided" is used here to represent the portion of the pulse which is expanding at a rate that is slower than that of vacuum diffraction. Even so, the total energy loss rate remains lower than the "self-guided" loss rate throughout the propagation. Here, as the "self-guided"

portion grows, the gaussian fit picks up more of the energy which explains the general trend toward the blue curve which is essentially zero. This low rate of energy loss was also observed in the spectral images in which spectral modulation, especially red shifting was not observed after a distance of $\sim$2000 μm.

Simulation 4 was the closest to the matched condition of self-guiding. Longitudinally, however, $c\tau > R_B$. As a result, some initial evolution of the laser pulse was necessary before reaching the ideal self-guided regime. The slope of blue dashed curve signifies that the transfer of energy between the laser pulse and plasma wake is increasing for the first 3500 μm. It should be noted that at around this point, self-trapping of electrons occurred. The change in energy of the self-guided portion of the pulse, shows energy loss due to diffraction for the first $\sim$2200 μm of propagation. This result is consistent with the results obtained by looking at the imaged spectra shown in Fig. 3.4 (g) through (l), in which the rate of red shifting could be used as a time stamp and showed that diffraction slowed as the pulse propagated.

3.4 Wake and Pulse Evolution

So far, we have looked exclusively at the evolution of the laser pulse considering only on conjecture, the associated evolution of the wake. Therefore in this section, the evolution of the laser pulse is considered once again. Also, the primary concern of laser plasma accelerators is ability to drive a large amplitude wake over extended distances, therefore this will be considered.

The first situation considered in this section is the wake associated with simulation 1 parameters. Here the density is high and pulse length $c\tau > \lambda_p$. We have shown in previous sections that this pulse is poorly guided and, the rate energy

transfer to the wake is low. Despite these facts, the wake created by such a pulse is surprisingly stable and maintains a high amplitude wake throughout most of the simulation length which is $\approx 4Z_R$.

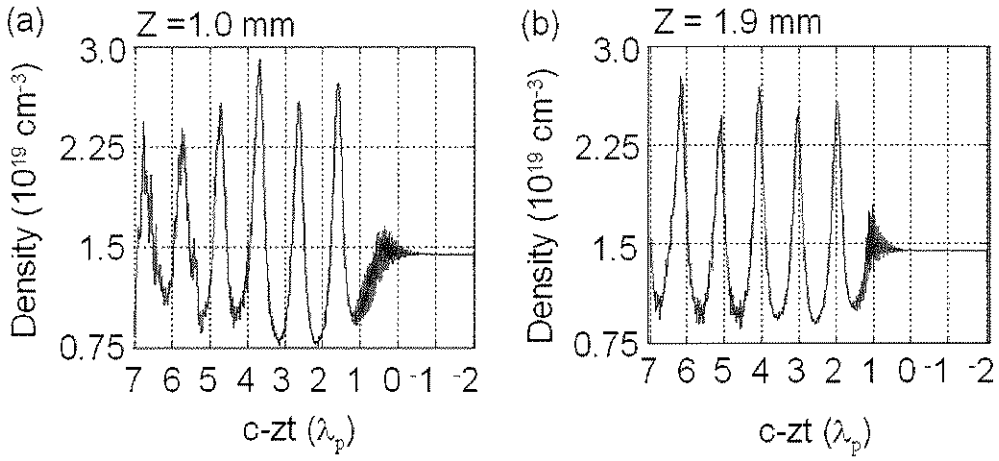

Figure 3.7: (a) shows the density wake after 1 mm of propagation. (b) shows the wake at the end of the simulation

In Fig. 3.7, a comparison between the wake amplitude at 1 mm (a) and 1.9 mm (b) is shown. These figures are density lineouts along the axis of the pump laser. Here, by inspection, one can see that the amplitude of the wake has not significantly changed over the second half of the simulation. Because the gradients are so large for LWFA, these quasilinear wakes are still under consideration by many groups[1]. This simulation shows with the advent of a robust external injector, this regime may prove acceptable for certain accelerator applications despite non-ideal self-guiding.

The density map in Fig.3.8 shows the highly nonlinear wake after 3 mm of propagation of the nearly matched simulation 4. The red curve along the side shows the projection of the density. The wake shown here has nearly reached a state when self-injection occurs. Indeed, it starts on the next simulation time

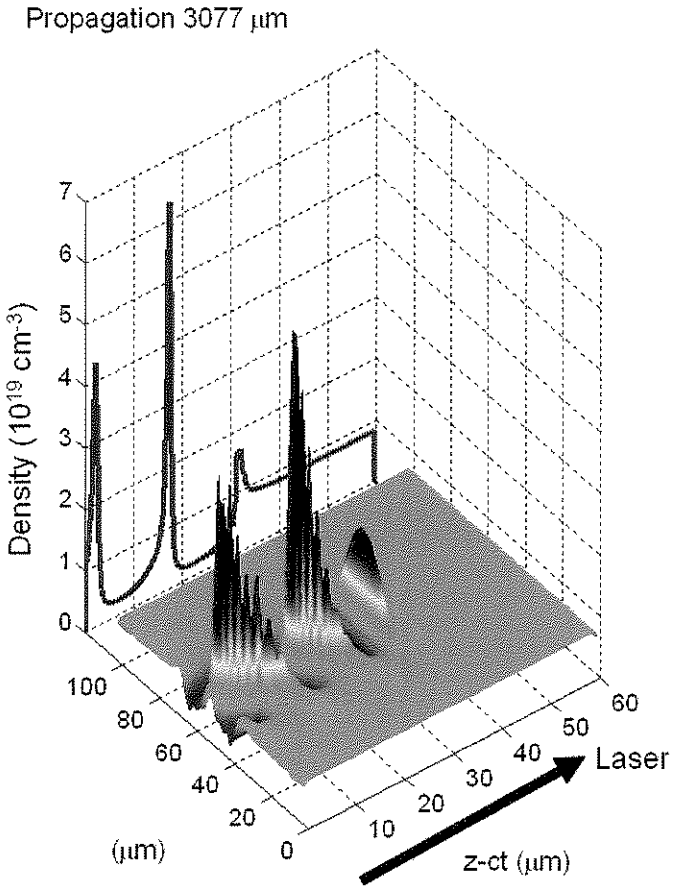

Figure 3.8: Highly Nonlinear wake in a 7×10^{18} cm^{-3} electron density plasma just prior to self-injection

step. To get to this point, the laser pulse has had to evolve considerably. Note the large increase in density at the front of the simulation. this increase, which is due to the longitudinal ponderom

Looking the pulse from a new point of view, Figs.3.9 (a) through (e) show the evolution of the pump pulse from the point of view of power. The curves along the sides are projections of the 3D image. Here the sum over 3 pixels of the square of the laser electric field is shown. This is essentially like taking

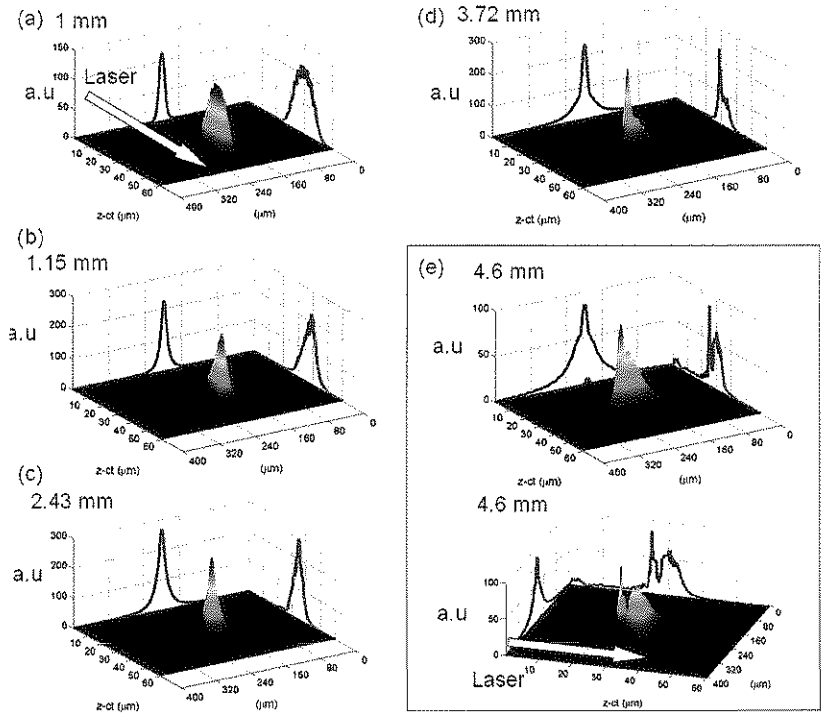

Figure 3.9: Images taken from simulation showing diffraction and pulse shortening of a 10TW pulse in a plasma with a density of 7 10^{18} cm^{-3}.

a 3 pixel slice of the power of the laser pulse through the middle of the pulse. Fig.3.9 (a) is the initial bigaussian laser pulse with the amplitude shown here as 110, however the initial pulse is still focusing at this time. As the pulse enters the plasma, the front of the pulse begins to diffract as shown in Fig. 3.9 (b), however as the front is diffracting the back is steepening, here the maximum is almost twice the initial peak. By half way through the simulation at 2.43 mm or $\sim$15 Z_r, we see in Fig.3.9 (c) the front diffracted portion of the pulse continues to diffract, but looking at the longitudinal projection, the pulse pulse has also continued to steepen and shorten as expected. By 3.72 mm, Fig. 3.9 (d) shows that the compressed portion of the pulse is no longer diffracting at a significant rate. We know this by looking at the longitudinal projection which shows a clear step between the diffracting portion which occurred much earlier (and by now has lost a great deal of intensity) and the compressed portion which had continued to steepen. By the end of the simulation, the "snowplowed" electrons which were pushed forward by the enhanced ponderomotive force due to pulse steepening have essentially separated the diffracting light from the remainder of the pump. We should note, that the intensity of the main pulse here is quite small since it is nearing pump depletion.

The results shown in Fig.3.9, were deduced in earlier sections. Recall the width of the spectrum in the imaged spectrograph told the story through continuous red shifting of the light. There we looked at the red shifted light as somehow encrypting a time stamp. From Fig. 3.4, it was argued that the highly red shifted light was diffracting at a lower rate compared to the initial light. This is indeed what is seen here. Also analyzing the forward spot diagnostic as a function of propagation distance, we were able to deduce the level of diffraction compared with guided light by looking at the associated energy derivative curves. What we have gained is an insight in to interpretation of experimental diagnostics through

simulation.

3.5 On Pulse Etch Rate

In this section, we compare the etch rates we observe from nonideal simulations to those predicted by theory[9, 40]. So far, we have observed that self-guiding can occur even for these nonideal cases to drive a highly nonlinear wake over tens of Z_R. This fact, in and of itself, indicates that the pump pulse has not yet been fully depleted, either through diffractive erosion or through etching of the front of the pulse from pump depletion.

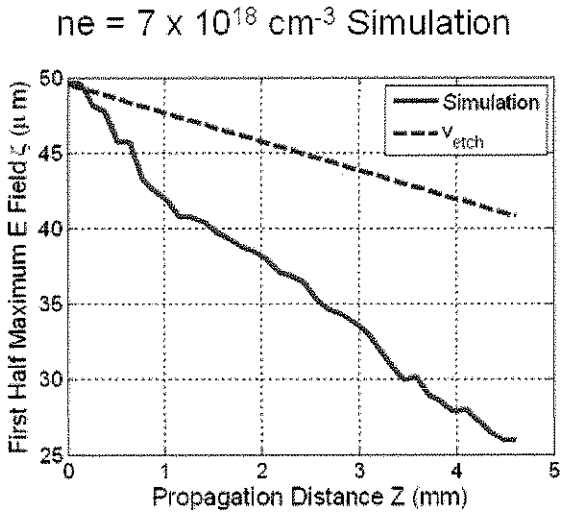

Figure 3.10: the slowing of the first half-maximum of the electric field of the laser vs. v_{etch}

Using the point of the first half-maximum of the contour of the laser electric field as a marker, the slowing of the laser pulse could be assessed. Fig. 3.10 shows the results vs. the etch velocity v_{etch}. The difference between these curve

is probably due the diffraction at the head of the pulse which tends to blurr the boundary beween where the pulse begins.

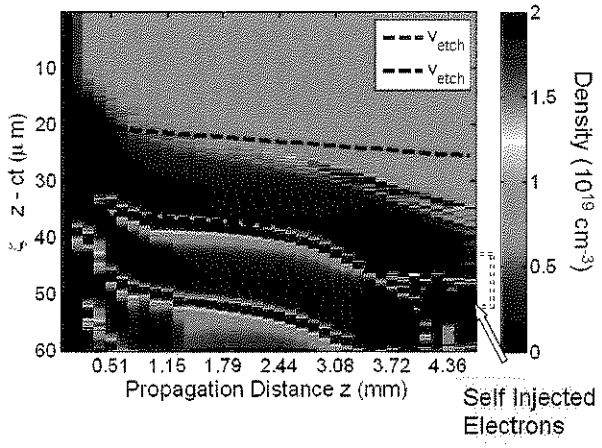

Figure 3.11: A map of the density wake vs. propagation distance in which the wake velocity is compared to the laser etch velocity v_{etch}

Finally, Fig. 3.11 shows the velocity of the relativistic plasma wave. The $\zeta = z - ct$ axis here is the axis of the simulation frame moving at the speed of light. The z axis is the propagation distance. Each z position, there is a plot of the lineout through the centr of the density, with is imaged using a color axis. Essentially, going from left to right is a series of lineouts of the density with the color axis given. The red peaks mark the peaks of the wake amplitude. These peaks are actually far above the limit shown here of 2×10^{19} cm^{-3}, but the color axis has been allowed to saturate in order to bring out the density peaks. Although, in Fig. 3.10, the laser pulse seemed to be etching a a fast rate, Fig. 3.11 tells a slightly different story. Initially, the wake quite slow since the laser pulse is evolving. However, between about .8 mm and 2.44 mm, the wake velocity looking at either the very front of the wake or the first density spike show a constant rate which is close to the predicted v_{etch}. After the pulse propagates further, however,

it slows down again perhaps as it appraoches pump depletion. This dramatic slowing of the phase velocity leads to injection of particles.

3.6 Simulation Conclusions

As mentioned earlier, simulations shown in this section have not represented ideal conditions for acceleration or for guiding. Simulations here are support of experiments. It has been shown through simulation that short laser pulses with sufficiently high P/P_c can evolve to the point where diffraction loss is almost entirely mitigated, even for the case of a pulse which is initially longer than a plasma wavelength.

From the 4 simulation cases shown here the following conclusions can be drawn. For laser pulse with $P/P_c > 1$ and a spot size above the matched spot for that density, two possibilities exist. If $P/P_c \simeq 1$, the pulse may begin self-focusing but never reach the matched spot prior to pump depleting. Such a pulse, once it has lost a sufficient amount of energy will no longer have a $P/P_c > 1$. This will lead to defocusing. Additionally, a laser pulse in this case continuously evolves. And since, (through simulation), we find that diffraction is greatest durring evolution, this is when the pulse loses a large portion of its energy. In the second case, the laser pulse has $P/P_c >> 1$ and a spot size greater than the matched spot size. In this case, rapid pulse evolution occurs, quickly bringing the spot size down to its matched size (which will be different after the evolution). The amount of energy that is unguided in this case scale with how much the pulse must evolve. In the third case studied here in which the initial spot size was smaller than the matched spot size, the pulse continuously expands, but a a rate lower than that of vacuum diffraction. Finally, the case was shown for a pulse which had a spot close to the matched spot size. In this case, diffraction

at the head of the pulse occurs at a reduced rate while the pulse compresses longitudinally. It would be interesting to see if coupling could be improved using a perfectly matched pulse.

Results outlined in this section show the benefit of forward diagnostics for observing the behavior of the laser pulse in the plasma. And, by understanding as a function of time (distance) how the pulse evolution looks on a variety of diagnostics greatly helps in intepretation of experimental results.

When considering that these results represent real experimental conditions, it is stiking that even in the best case where the spot size was matched, simulations show that at least 25% of the initial energy was lost initially in coupling. Simulation 2 represents one of the dream beam experiments [48] which in fact, produced a monoenergetic electron beam at Rutherford Appleton Laboratory. In that case, 60% of he energy in th self-guided spot was lost in the first 300 μm of propagation (probably more in the real experiment). Minimization of these initial losses could greatly reduce the laser power that is needed to observe monoenergetic beams in experiments. This may be one arguement in favor of plasma waveguides. These plasma waveguides or lenses may collect the diffracting light before it is lost.

CHAPTER 4

Experiment Preparation

4.1 Introduction to Experiments at UCLA

Experiments conducted at UCLA have focused on demonstrating the possibility of self-guiding short laser pulses to extend the interaction length in LWFA as outlined in recent 3D theory[39]. In preparation for the experiment, calculations were performed to determine if such an experiment could be conducted using existing laser facilities at UCLA. These include a laser, plasma source and vacuum chamber large enough to accommodate the experiment.

We start with the minimum conditions necessary for blow-out and self guiding. To achieve blow-out and self-guiding, a minimum power was needed $P/P_{crit} \geq 1$[69]. For an electron plasma density n_e of 7 $\times 10^{18}$ cm^{-3}, the critical power for relativistic self-focusing is 4.22 Terawatts. For a 50 fs pulse length, this requires 211 mJ of coupled laser energy. The vector potential a_0 of the matched spot can be found from $a_0^3 = 8P/P_{crit}$. From this, we can get the matched spot size for minimal spot size evolution as,

$$w_{match} = \frac{2\sqrt{a}}{k_p} \tag{4.1}$$

which for above conditions leads to a matched spot of 5.6 microns. For perfect guiding in which the head erosion scales the same as the diffraction,

$a_0^c > (n_{crit}/n_p) = 3$. This parameter space seemed within reach of the labs capabilities.

To diagnose the experiment, quantitative diagnostics for the experiment were needed. Forward diagnostics would look for a guided spot (imaging microscope) , the spectrum of the tranmitted light (prism spectrograph), and the spatially resolved spectrum of the transmitted light (imaging spectrograph). The transverse diagnostics looked for plasma features (Sclieren Imaging) and plasma density profile (Interferometry). Finally, radiation from self trapped electrons was monitored using an surface barrier detector (SBD) in the forward direction. Additionally, a great emphasis was placed on laser diagnostics.

4.1.1 UCLA Multiterawatt Laser System

The UCLA Ti:Sapphire laser system was originally constructed by Positive Light Inc. as among the company's first high power Ti:Sapphire systems. The system uses chirped pulse amplification CPA to achieve at maximum 20 TW in a 40 fs pulse. These benchmarks have not been reached to avoid damage to the optical system. The maximum power delivered to the experiment was 12 TW in a 50 fs pulse. The energy in the beam was not increased to avoid damage to optical components in the laser system.

A schematic representation of the laser system is shown if Fig. 4.1 as it was during the time period of the experiments described in this thesis. The laser system can be divided in to 6 sub-systems: a self-mode locked oscillator, a stretcher, a regenerative amplifier, a 4 pass amplifier, a two pass amplifier, and a compressor. A thorough description of the laser system can be found F. Fang's dissertation[16]. Here an overview of the system will be given.

The oscillator in our system runs at 40MHz. This oscillator runs freely with

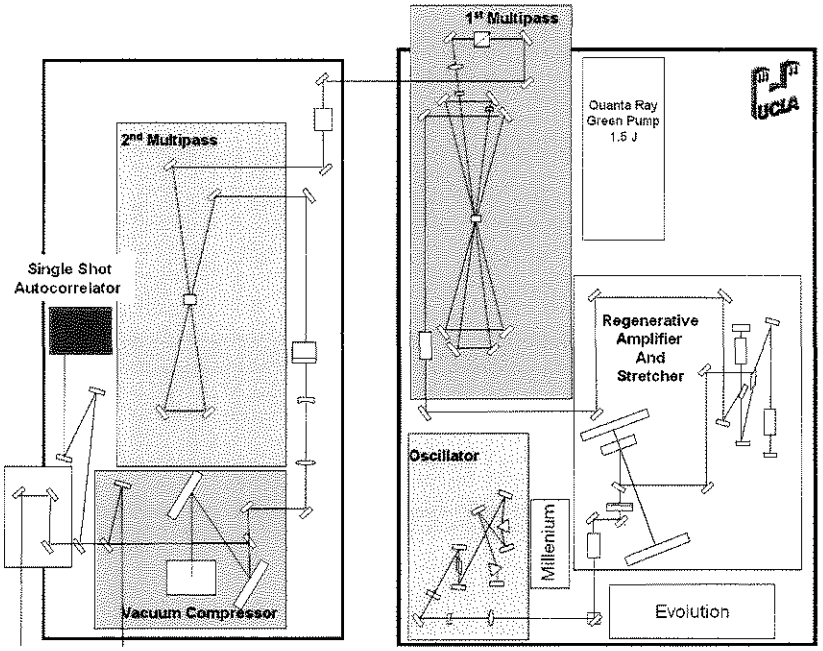

Figure 4.1: UCLA Ti:Sapphire Laser System

no feedback and is pumped using a diode pumped frequency doubled glass laser by Spectra-Physics Inc. (Millennia) which runs quasi cw. Since the oscillator contains no feedback, day to day stability and reproducibility of this system required constant care. Slowly, a systematic procedure for starting and warming up this laser was developed which greatly increased the reliability of this crucial system. The lab system clock originates from the oscillator. A pick off sent to a fast photodiode creates the initial high frequency which once divided down provides the clock from which the system timing originates. This upgrade allows for less jitter in timing of pulse injection and dump Pockel Cells in the regenerative amplifier. However, since the regenerative amplifier pump still jitters on a ± 20 ns time frame, this may slightly affect the gain and amplified stimulated emission ASE from the regenerative amplifier. The oscillator provides pulses with typical bandwidths in the range of 30 to 50 nm centered around 810 nm. The train of

pulses is sent to a grating stretcher which chirps the pulse, sending a blue-to-red ~200 ps (depending on the bandwidth) pulses each with a few nJoules of energy to the regenerative amplifier.

The regenerative amplifier (Positive Light Inc. Spitfire), was pumped using a kHz frequency, diode pumped frequency doubled glass laser (Spectra-Physics Inc. Evolution). A single stretched pulse from the oscillator is injected using a Pockel cell. The injected pulse is timed to be as close as possible to the pump timing while still extracting all the gain. A pulse here which is injected late will be amplified on top of any ASE which built up prior to injection. Weak injection pulses also suffer from ASE. After 10 to 20 round trips through the regenerative amplifier another Pockel cell ejects the pulse which now contains approximately 1 mJ energy. The average power out of the regenerative amplifier is about 1 watt. The bandwidth full-width-half-maximum FWHM out of the regenerative amplifier was typically between 18 and 22 nm centered at 815 nm. At a kHz, this makes an ideal beam for doing any infrared alignment.

The four pass amplifier is configured as a bow tie as shown in Fig. 4.1 and runs at 1Hz. It is pumped using a flashlamp pumped frequency doubled ND:Glass laser (Spectra-Physics Inc. Quanta Ray Pro). After four passes, the pulse is amplified to between 100 and 250 mJ. An isolation Pockel cell located between this amplifier and the next amplifier was removed early in the experiment after it was found that nonlinear effects caused by this limited the pulse compression.

The final amplifier in the system is a two pass bow tie system which uses a large aperture ~4 cm diameter Ti:Sapphire crystal. The pump laser for this amplifier is an independent frequency doubled 1 μm laser system. This system produced up to 5 Joules of 532 nm light to pump the large aperture crystal. However, this system has a maximum repetition rate of 1 shot per every 5 min-

utes. The gain here resulted in pulses amplified to approximately 1 Joule. The transmission through the compressor was around 65% resulting in a maximum of approximately 650 mJ. The measured bandwidth through the system was found to be unaltered through the two multipass amplifiers which follow the regenerative amplifier.

The laser pulse length was measured using a commercial single shot autocorrelator also from Positive Light. The typical day to day variation in pulse widths was 45 to 60 fs. The contrast of the laser was controlled using a fast photodiode which monitored the regen pulse or pulse after the first multipass amplifier. Prepulses seen on this diagnostic which could detect ns scale prepulses on the order of 10^{-3} originated from the regenerative amplifier and typically could be resolved by adjusting slightly the injection or ejection timing of the regen.

4.2 Gas Jet Characterization

The ideal target for this experiment would be a low density plasma at a low temperature of a few EV which rises from 0 density to a density of between 2×10^{18} to 2×10^{19} cm^{-3} in a distance of less than a skin depth. However this type of target is not currently possible, gas jets with steep edges and near uniform density plateaus present a good approximation to this. The rise of the jet should be less than the Rayleigh length of laser to avoid unwanted defocusing due to ionization. The nozzles chosen for experiments here were replicas of the nozzles described in reference[59]. The gas was pulsed using a poppet. The jet ramp up time was found to be 3 ms. The system minimum pulse duration was 11 ms providing a window of between 3 ms and 11 ms where a reasonable profile was produced. Normal operation used a delay of approximately 4 ms. Only nozzles with critical diameters of 500 μm were used(compared to 1 mm). The reason for this was because the poppet type gas jet pulser which was used had an opening of only 800 μm. This aperture would choke the flow of the 1 mm critical aperture nozzles creating a jet with a nonhomogeneous. profile[31, 59]. Gas jet targets used were supersonic. Typically, the higher the Mach number of the flow, the steeper the edge. However, supersonic nozzles are also susceptible to shocks which could originate from imperfections in a poorly machined nozzle or from the nozzle design and create ripples in the density.

To analyze the gas jets, a Mach-Zehnder type interferometer was setup using a Helium Neon laser with a wavelength of 632.8 nm or 530 nm as can be seen in Fig. 4.2. This setup is similar to the setups used by other groups to characterize cylindrically symmetric nozzles[43]. Although He was used in the experiment, Argon was the gas of choice for analyzing the gas jet profiles of the gas jets used in this experiment. The primary reason for this is that the refractive index

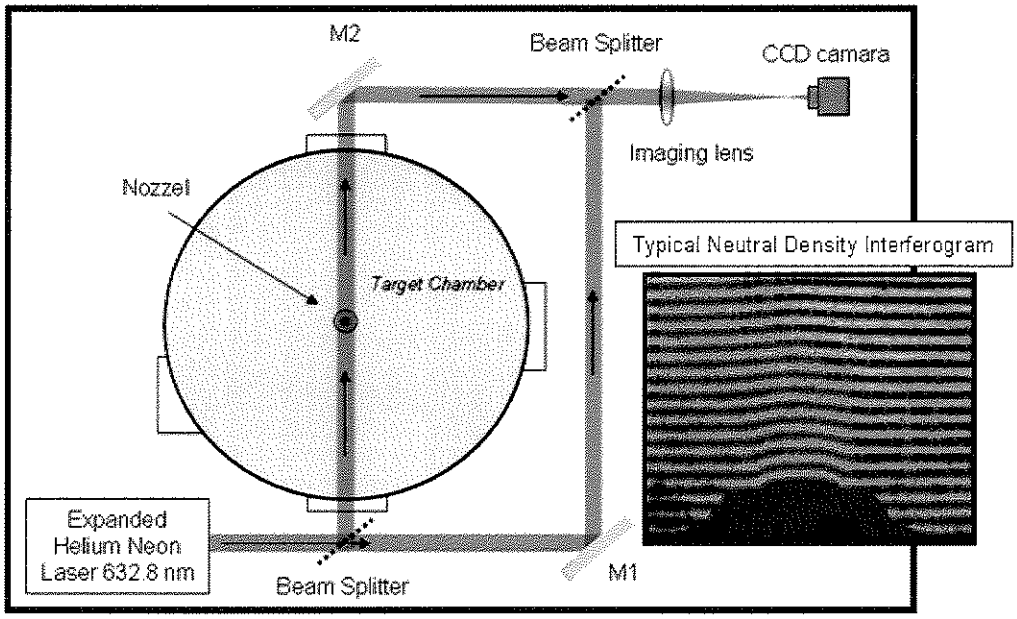

Figure 4.2: Setup of Mach-Zehnder Type Interferometer used to analyze neutral gas jets

of neutral Argon is 1.000281 while the neutral refractive index of He is only 1.00003242600. In other words since we are looking for differences in phase of the beams in the two arms of the interferometer, the He phase shift is about a factor of ten less then Argon. At very high densities it was possible to see a fringe shift using neutral He[16], but not at densities useful for this experiment. The inset of Fig. 4.2 shows a typical interferogram taken from the 3 mm nozzle used in the experiment.

Using a method very similar to the method described later for analyzing plasma density, the phase at each location was first determined. The phase information was then Abel inverted to get the radial density map shown in Fig. 4.3.

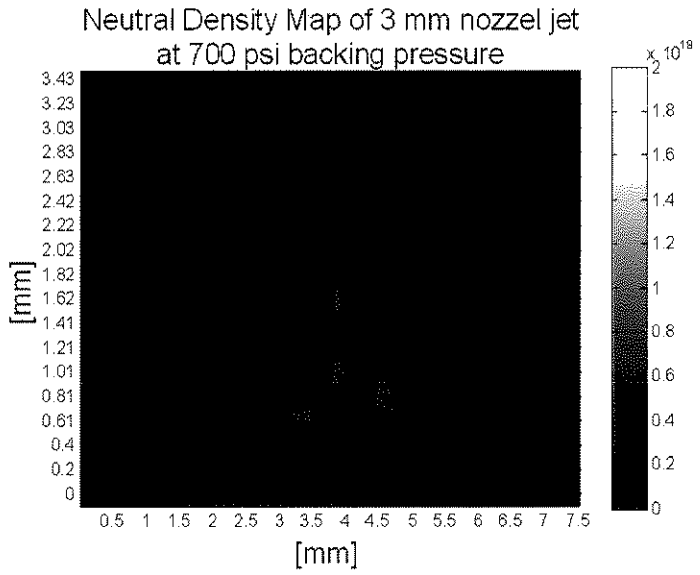

Figure 4.3: Density Map of 3 mm Gas Jet From Interferometry

From the data in Fig. 4.3 a density profile at any height can be obtained. Fig. 4.4 shows the profile of the 3 mm jet a distance of 800 μm above the nozzle. The edges of the jet appear steep with a 10% to 90% rise distance of approximately 250 μm. The uniformity of the profile remains in question however when ones

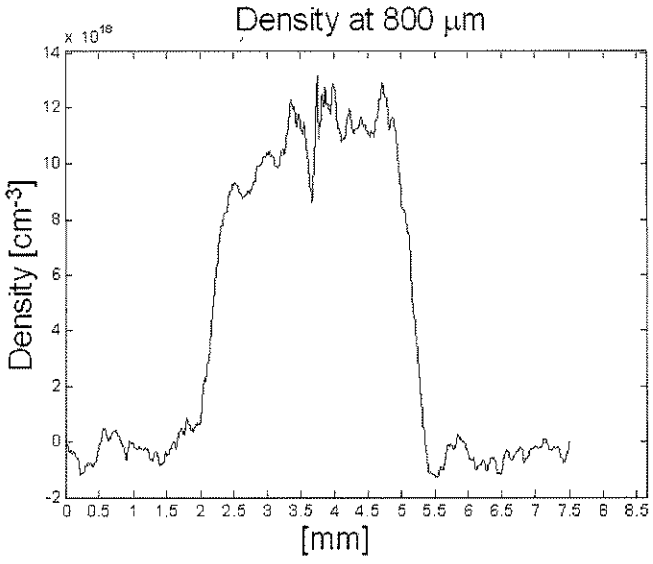

Figure 4.4: Neutral radial density profile of 3 mm gas jet a distance of 800 μm above the nozzle

looks at this image. The "top" of the profile appears to be a ramp from 1 $\times 10^{19}$ to 1.2 $\times 10^{19}$ cm^{-3}. In reality, it is far more likely that the error is in the analysis. The sharp spikes seen on the edges are probably real. Abel inversion alway results in a dip at the center and can be seen at 3.5 mm. This is not a real density depression.

Finally, the results of the peak neutral gas densities of the 3 mm and 2 mm nozzles are plotted as a function of backing pressure in Fig.4.5. Plasma densities obtained from Lloyd mirror interferometer durring the experiment for the 5 mm and 1 cm nozzles were far more reliable and will be shown later.

The neutral gas flow of the jets using Helium should be close to the that of neutral Argon. As a result, the density of the doubly ionzed plasma should be about 2 times the neutral gas density of Helium.

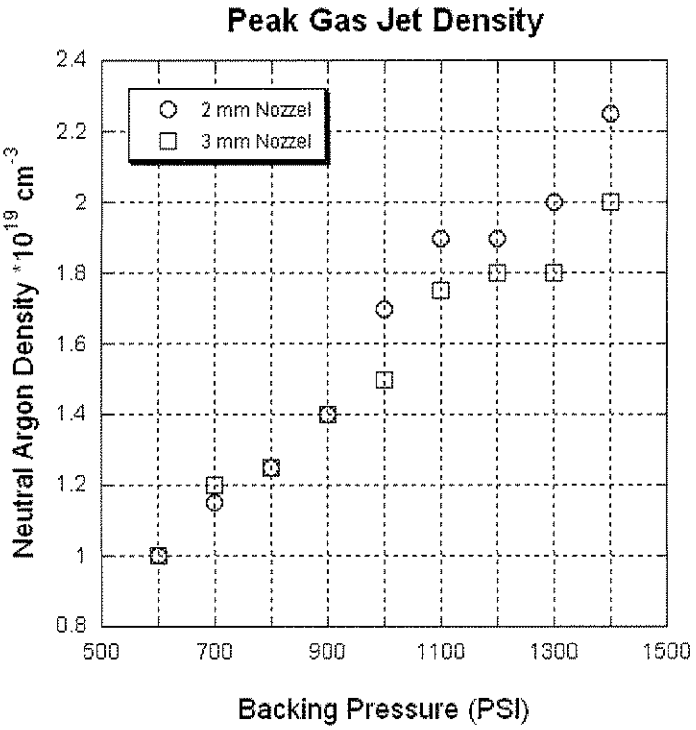

Figure 4.5: Plots of the neutral Argon density with backing pressure for 2 mm and 3 mm conical gas jet nozzles

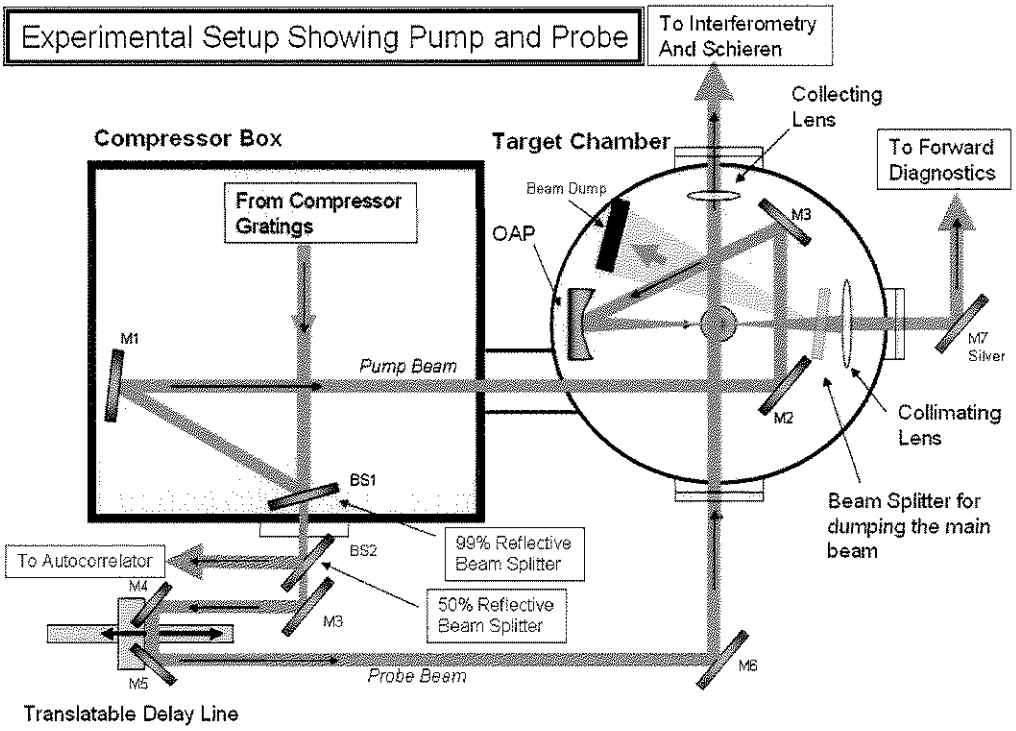

Figure 4.6: Schematic representation of the Experimental setup showing Vacuum Chamber, Pump and Probe beam paths from the compressor.

4.3 Experimental Setup

A schematic representation of the experimental setup is shown in Fig. 4.6. The compressor chamber and target chamber were connected as shown and share a common pump system capable reaching a vacuum of 5 $\times 10^{-5}$ Torr if left to pump over night. A typical vacuum for running the experiment was in the range of 10^{-4}.

Referring to Fig. 4.6, the compressed pulse was split by a 99% reflecting beam spltter. The main pump pulse was reflected off 2 mirrors in the compressor chamber in order to match the path length of the pump with the probe. The

next 2 folding mirrors were used to align the 3" diameter, 30^0 off axis parabolic mirror (OAP). The focal length of the OAP was 22 cm. The size of the beam was about 5 cm in diameter giving an approximately f/4 focusing. A 2 inch lens with a 25 mm focal length recollimated the beam after dumping 99% of the transmitted light. The collimated beam was then sent to forward diagnostics where it was reimaged by additional lenses. The focal spot from the OAP is shown in Fig. 4.7. This image was taken using a 12 bit CCD camera and 20× microscope with a resolution of $2\mu m$ and was placed directly in the vacuum chamber with no additional optics. To obtain this image, the beam was attenuated up stream.

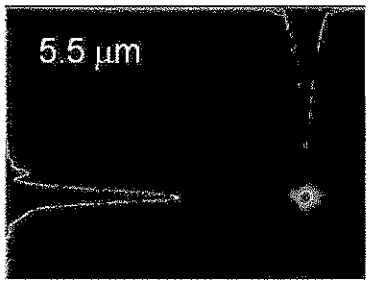

Figure 4.7: Vacuum focus image with 2 μm resolution 20 × microscope

The probe beam is seen in Fig. 4.6 as the 1% transmitted through the beam splitter in the compressor chamber. A second beam splitter splits off an additional 50% which is sent to the autocorrelator as a pulse length diagnostic. The remaining 50% is used as the 90^0 probe beam via a trumbone style delay line. The translation stage used on this delay line was a high accuracy stepper motor with submicron precision. This stage was mounted on a rail for course adjustment. The probe beam was centered so that half the beam passed directly over the gas jet. This allowed the other half to be used as the reference portion of the folded wavefront interferometer described later.

4.4 Transverse Diagnostics

Two transverse diagnostics were used in this experiment. Schlieren imaging and interferometry. These diagnostics provided a side view of the laser produced plasma. A photograph showing the setup of these diagnostics is shown in Fig. 4.8. The pump beam in this figure comes in from the top and focuses on the front edge of the gas jet. The collimated 3 cm diameter probe beam comes from the left passes through the plasma and passes through a 3 inch lens. This 30 cm focal length lens creates an image of the plasma at infinity, but focuses the collimated probe 30 cm away. The focusing probe is split. The reflected probe focuses on a knife edge while the transmitted probe focuses near the edge of the Lloyd mirror. Both Diagnostics create an image of the plane of the image the plasma on their corresponding cameras. The Sclieren imaging was slightly demagnified and the interferometry had no magnification. It should be noted that the setups of both the target chamber and diagnostics did change slightly during the experiment, however the primary functions of all diagnostics remained the same.

The transverse diagnostics used in this experiment were important not only to the overall understanding of the interaction, but also played a critical role in detecting short scale (< 10 ps) prepulses which were large enough to cause ionization. The origin of these prepulses may come from fluctuations in the spectral shape of the laser pulse.

The schematic side view of the experiment is shown as an inset in Fig. 4.8. Here the pump is going from left to right. The probe beam is represented by the pink circle. The thick yellow is the plasma line.

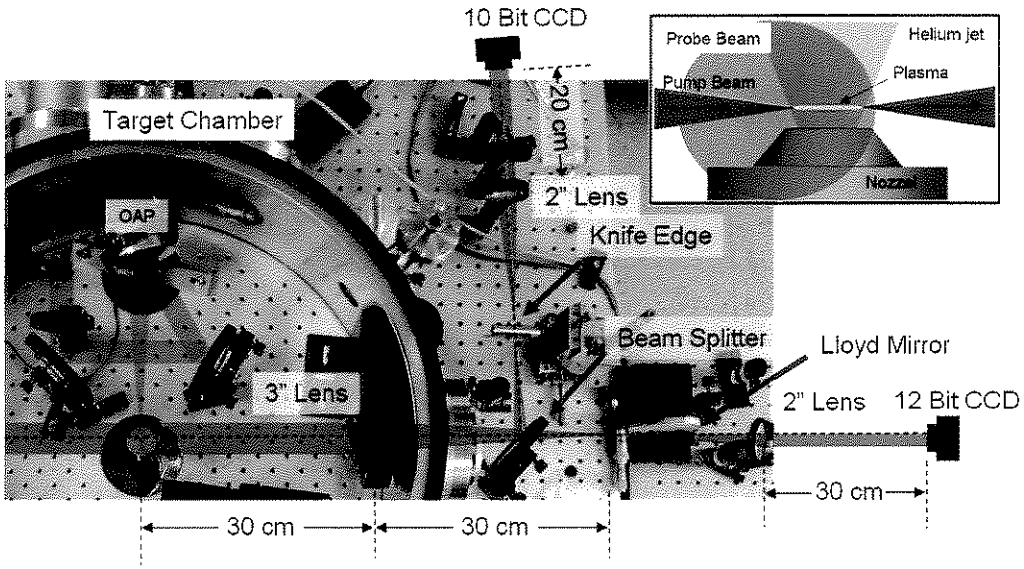

Figure 4.8: A photograph of the setup showing transverse Schlieren and Interferometry diagnostics, the inset shows a side view cartoon of the probe beam, nozzle, pump beam and gas jet

4.4.1 Plasma Density Measurements

Interferometry can be used to measure and quantify the relative phase of a coherent or partially coherent light source. We used interferometry in this experiment to obtain information about the density, density distribution, spatial dimensions, shape, as well as information about any preionization due to a long or short prepulse. The interferometry technique employed was a folded wavefront Lloyd mirror type interferometer. This type of setup uses only a single collimated large size probe beam, in which half of the beam overlaps the gas jet and the other half does not. In our setup, the probe beam was aligned so that the center of the probe beam passed approximately at the point where the pump laser enters the jet as seen in Fig. 4.8. The exit could also have been used as long as no plasma "spills" out with the laser which effects the reference portion of the probe. In considering a setup for a Lloyd mirror, it was crucial to separate the focus of the collimated beam with the image of the plane of the plasma. This is because it is between these two points that the Lloyd mirror must be placed.

A lens was placed 30 cm away from the center of the jet providing an image at infinity, but a focus (of the collimated beam) 30 cm after the lens as seen in Fig.4.8. The Lloyd mirror was placed so that the surface was close to parallel to the direction of propagation and so that the edge of the mirror was at or slightly after the focal location. A final 30 cm lens recollimated the beam and produced an unmagnified image 30 cm away where a 12 bit camera was placed.

This type of interferometry setup was well suited to our experiment. Since the same beam was used for both arms of the interferometer, temporal overlap to a high degree was automatic. This was critical since the pulse length of the probe was only 60 fs (or 18 μm). To use a Mach-Zehnder type interferometer with these short pulses would have required the path lengths of the 2 beams

to be within $\sim 2\ \mu m$ for good overlap to occur. Secondly, since only one probe beam path was needed, a significantly smaller setup was required, more space was left for additional diagnostics. Finally, alignment time was significantly less than required for other types of interferometers.

For the densities used in this experiment, there was no need to frequency double the probe beam. In fact, this would have lead to smaller fringe shifts (by a factor of 2) which are more difficult to analyze. For plasmas, the following equation governs phase shifts for light in a plasma.

$$\Delta\phi = \Delta \int_0^L k \cdot dl \tag{4.2}$$

If the ionizing pump laser pulse is radially symmetric, it should form a radially symmetric plasma. This allows us to get the radial profile of the plasma using an Abel inversion. Approximating the refractive index η model of a highly underdense plasma where $n_e << n_c$, given by $\eta = 1 - 1/2(\omega_p^2/\omega_0^2) = 1 - 1/2(n_e/n_c)$. The change in phase $\Delta\phi$between the two overlapping beams of the interferometer can be rewritten as,

$$\Delta\phi = \frac{2e^2\lambda}{mc^2} \int_0^L n_e(r)dy. \tag{4.3}$$

Here $n_e(r)$ is the electron density as a function of radius of the laser produced plasma. The Abel inversion applied to the plasma is given as,

$$n_e(r) = \frac{1}{\pi} \int_r^{r_0} \frac{d\Delta\phi/dx}{\sqrt{x^2 - r^2}} dx \tag{4.4}$$

Here a numerical approximation of Eqn.4.3 was used to perform the following Abel inversion in Eqn.4.4 to obtain the density. In contrast to Fourier series approximations to the shape of the plasma, here only a simple rectangle rule is

used. The inherent singularity is ignored by truncating the last delta x in the integral. This is justified by the fact that the absolute integral does not produce a singularity. Results are consistent with calculations.

To obtain the phase information from the interferograms, an algorithm was utilized to track the individual fringes. To avoid unwanted noise in variation of amplitude. The method first finds the second derivative zero crossing. Active thresholds assure that only real phase differences are registered. This point is effectively, the inflection point between each half fringe, providing two accurate phases for each fringe. The change in phase is computed by tracing each fringe from some point at the edge where there is only neutral Helium. At these densities, as discussed earlier, the neutral Helium does not effect does not effect the fringe shape and thus, can be ignored.

The images of the 5 mm plasma shown in Fig. 4.9 are produced automatically by the analysis code described above. The top is a raw interferogram. The middle is an analyzed interferogram and the bottom is the line through the center. Since the center is the most numerically unstable region, the peak density shown at the top of Fig. 4.9 was found using off axis data. As a result of following the fringes, some phase information was lost, this shows up as dramatic changes in the calculated density.

Finally, a summary showing the backing pressure in PSI vs. the plasma density is shown in Fig. 4.10. Here the data from all shots has been collected. Slight variation in nozzle y (up down) position may account for some of this variation. Even so, the variation was typically less than 1×10^{18} cm^{-3}.

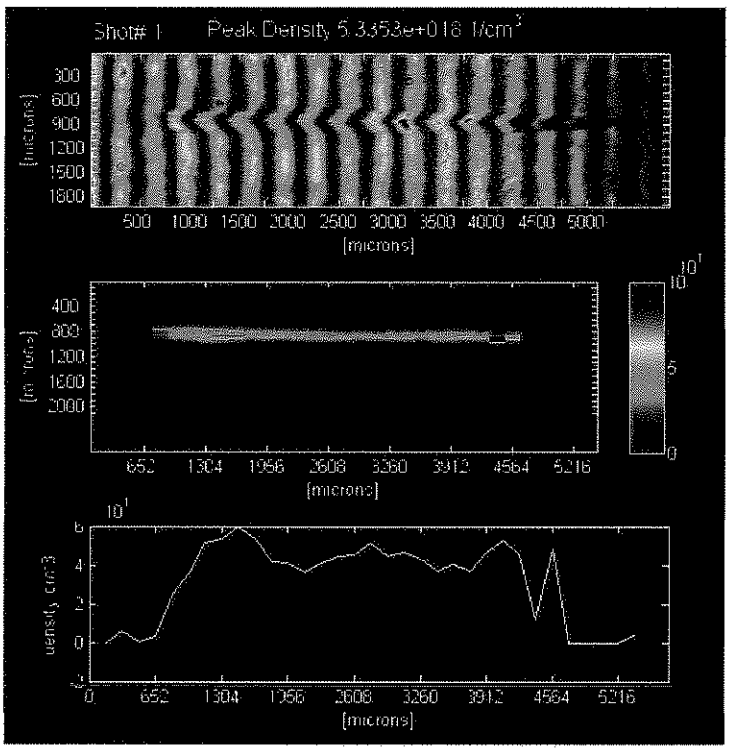

Figure 4.9: Typical screen shot from fringe analysis program showing from top to bottom: the raw interferogram, an image of the plasma density after phase analysis and a lineout through the center of the density image.

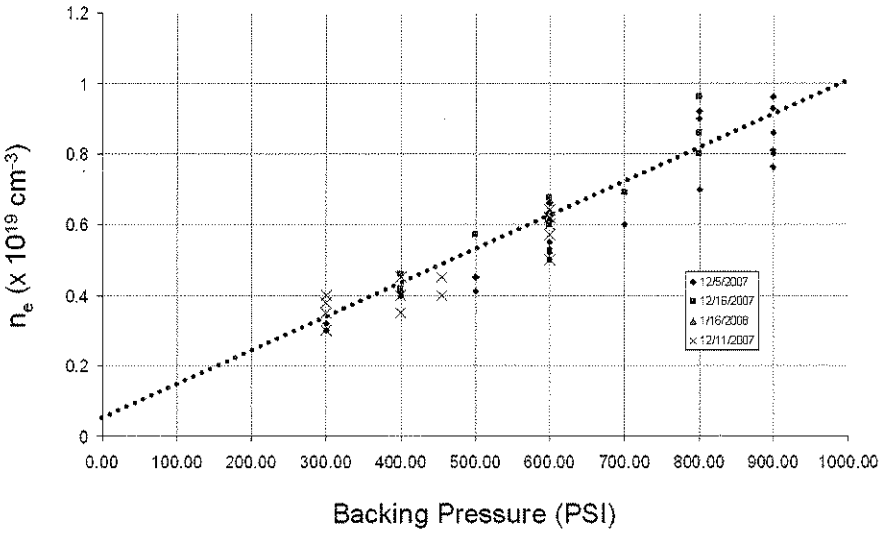

Figure 4.10: 5 mm plasma density measurements vs. backing Pressure. Data points valid within $\pm 0.05 \times 10^19$ cm^{-3} due to resolution of diagnostic. The spread in data is due to shot-to-shot variation in plasma density.

4.4.2 Schlieren Imaging

In photography, one can visualize very small phase shifts such as those seen by a leaky gas pipe, or even the heat rising off a persons hand. This high degree of sensitivity, when applied to low density plasmas provides an image from which one can easily enable visualization of the entire region of ionization which even at low densities represents a relatively large refractive index change when compared to the background neutral gas. By using a 60 fs probe pulse, this diagnostic additionally provides a means of visualizing preionization due to any prepulse. Any detectable prepulse has been found to sufficiently disrupt the plasma at the entrance leading to breakup of the main pulse.

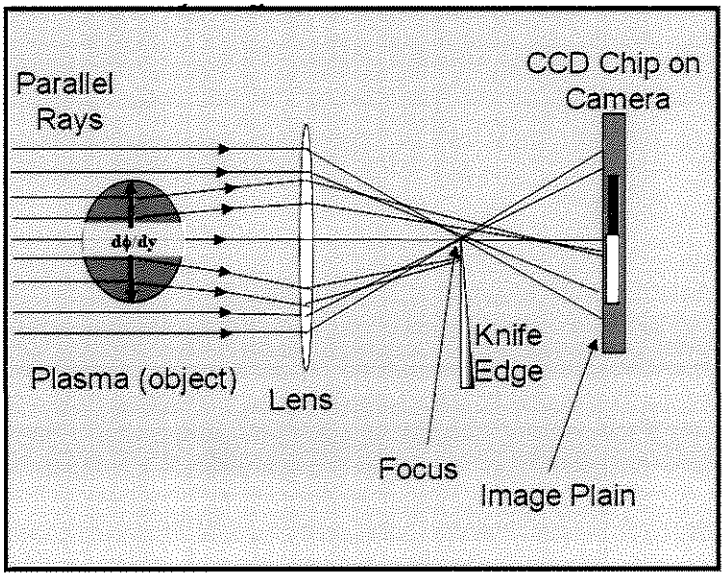

Figure 4.11: Ray Diaggram of Schlieren Imaging showing how the effect of plasma lensing on a parallel probe beam can be imaged

The basis for Schlieren imaging resides with the ability to transform phase information into amplitude information. Other diagnostics in this category in-

clude dark field, phase contrast and shadowgraphy. Each of these diagnostics rely upon the perturbation of backlight due to a phase change at the object plane. Whereas dark field, phase contrast and shadowgraphy are not orientation specific, Schlieren imaging sees phase changes only along a single orientation. This orientation is determined by the amplitude gradient inserted at the Fourier conjugate plane. If a knife edge is used to provide the amplitude gradient, the Schlieren image appears as dark and bright regions. These regions are associated with the derivative of the phase along density gradient. Figure 4.11 shows a schematic representation of the Schlieren setup used in our measurements.

The schematic representation shows how plasma acts like a 'weak' lens. The portion of the light refracted up by positive gradient part of the the plasma lens, misses the knife edge and appears bright. The portion of the light refracted down by the negative gradient portion of the plasma lens is stopped by the knife edge and appears dark. Moving the knife edge along the conjugate spot effectively modifies the gradient threshold for dark and bright regions. Throughout the measurements in this experiment, the knife edge was positioned as close as possible to the zero point of the gradient. Thereby, providing a reference for the central axis of the plasma, which occurs at the point where the dark and light regions meet.

In Fig.4.12 Schlieren images of the laser produced plasma are shown. In Fig.4.12(a), the knife edge was set horizontal producing the usual dark region at the bottom and light region at the top of the approximately cylindricaly symmetric plasma. In Fig.4.12(b), the knife edge was rotated to vertical. Additionally, this figure shows the temporal resolution of the 60 fs probe. Here the probe has been timed to intercept the pump during the transit time of the pump. Therefore, in Fig.4.12(b), the white portion represents the ionization front of the pump

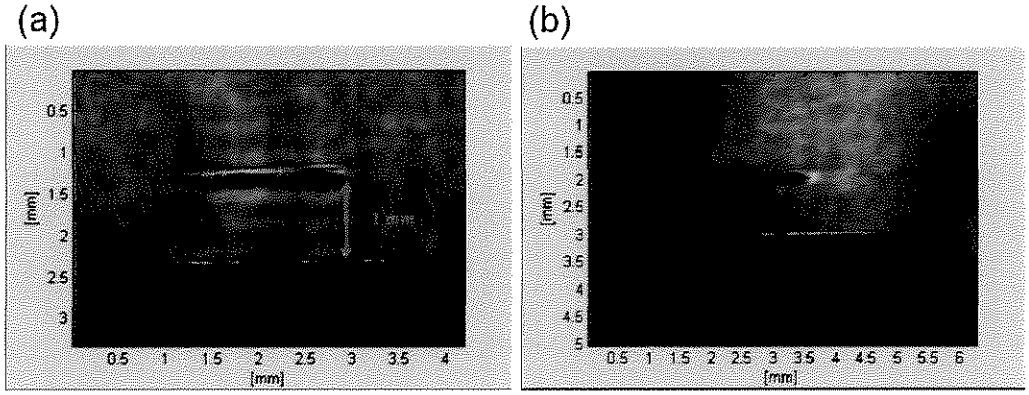

Figure 4.12: Sclieren Images using the horizontal knife edge Fig.(a) and vertical knife edge Fig.(b)

laser pulse and shows no prepulse.

4.5 Forward Diagnostics

Three forward optical diagnostics were used in the experiment. Each of these utilized the image relayed from either the entrance or exit plane of the gas jet in use. The spectrum of the laser pulse exiting the plasma was obtained using two complementary spectrographs, a 1/3 meter imaging spectragraph with a 12 bit CCD camera and a broadband infrared prism spectrograph which uses an infrared camera with a cutoff $\sim 2.2\ \mu m$. Additionally, the quality and spatial features of the guided spot at the exit were captured with a 12 bit CCD camera.

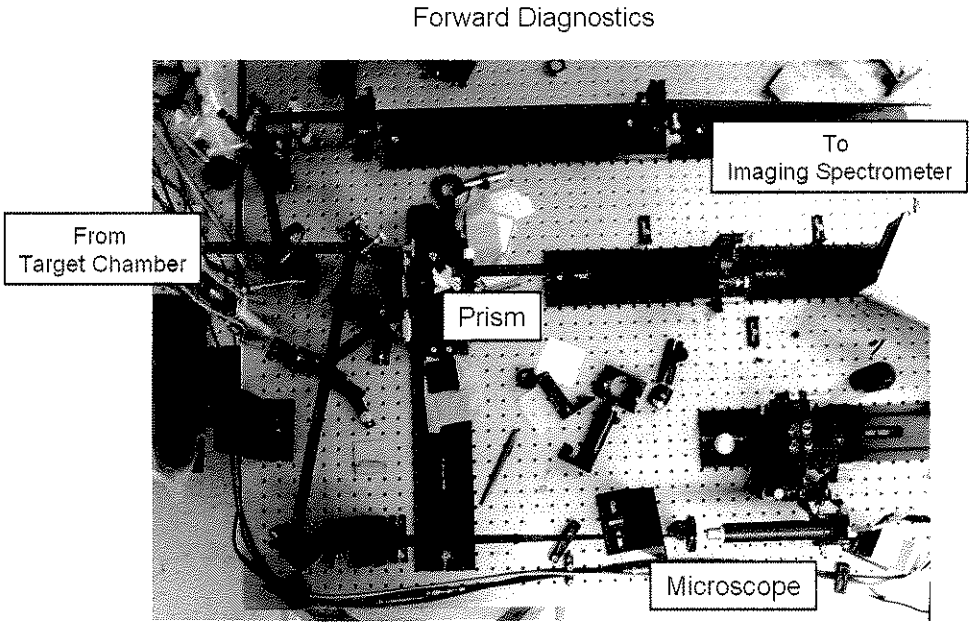

Figure 4.13: Photograph of the Forward Dignostics Setup

The longitudinal magnification of each diagnostic was obtained by mounting a resolution target at the image plane in the target chamber. The resolution target was mounted at the exact location of the interaction and could be translated along x, y, and z. An image was formed on each of the three diagnostics in the forward

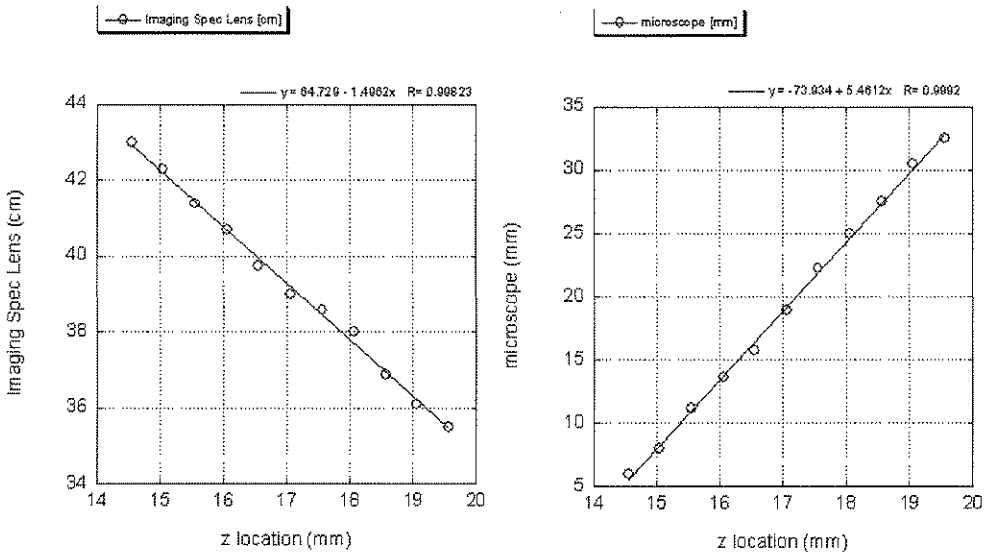

Figure 4.14: Plots of longitudinal typical longitudinal calibrations of the imaging spectrometer and the forward mode imaging diagnostic

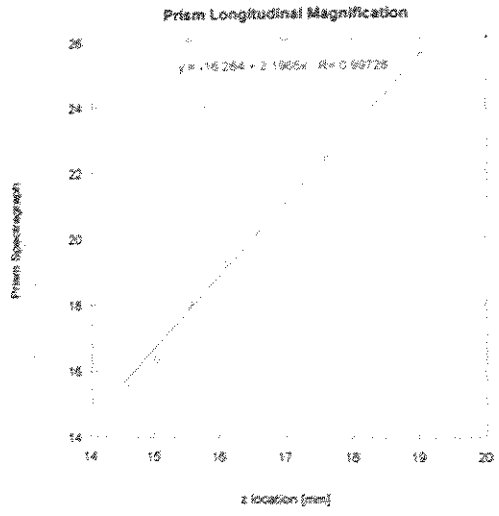

Figure 4.15: Longitudinal calibration of the prism spectrograph

direction. As the target was moved, the image on each of the three diagnostics was brought back into focus. On the imaging spectrograph, this was accomplished by translating the final imaging lens. In this way, the image plane could be mapped out. This allowed for one to change the image plane from the input to the exit of the nozzle (or anywhere in between), and know with confidence where exactly the image plane was. This was accomplished on the forward imaging system and the the prism spectrograph by translating the cameras instead of the lens. On the prism spectrograph, the camera was mounted on a rail. The microscope and camera in the forward exit mode imaging system was mounted on a translation stage and a rail, for fine and course adjustment respectively. Fig. 4.14 shows the plots obtained from a typical calibration of longitudinal magnafication of the forward imaging spectrometer and forward imaging camera. The associated plot obtained for the prism is show in Fig. 4.15.

4.5.1 Forward Exit Imaging

Imaging in the forward direction is an essential diagnostic for determination of laser guiding of any type. The primary purpose of this diagnostic was to determine the spatial quality of the guided beam. This diagnostic additionally provided an essential zeroth order look at whether or not the laser was well coupled to the plasma.

The camera used was a 12 bit CCD camera with either an 8 $\times$ microscope objective or a 4$\times$ objective. The image was relayed to the microscopes image plane with 2$\times$ magnification. In order to be able to translate through focus, the camera was mounted on a rail as seen in Fig. 4.13 for rough alignment. The camera was mounted in such a way that it had 5 axes of motion, two rotation and x,y and z.

A 2 inch diameter lens with a 25 mm focal length was located in the vacuum chamber 25 mm from the gas jet to provide an image at infinity. A second 2 inch lens with a 45 mm focal length reproduced the image. The microscope magnified the image depending on the set magnification. The measured resolution of this optical system was 9 μm. An estimate of the resolution $R = \lambda/(2 \times N.A.)$ gives a resolution of 2 μm assuming that all rays are collected after the first lens. Here N.A. is the numerical aperture of the first collection lens. In our system, due to spatial constraints, the second lens (imaging lens) in the imaging system was not placed to optimally collect all the light. As a result, the resolution was limited to between 6 and $8\mu m$.

4.5.2 Prism Spectrograph

The prism spectrograph used in the measured described in this dissertation was designed to encompass as much of the guided light spectrum as possible. This was especially important since as the laser approaches pump depletion a large red shift was expected.

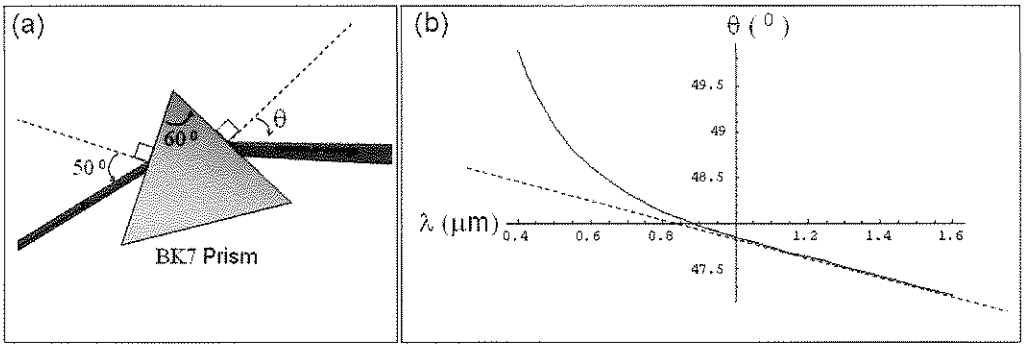

Figure 4.16: Prism spectrograph dispersion designed for linear region for longer wavelengths.

The camera used in this spectrometer was an infrared camera (Electrophysics Inc. Micronviewer) with a bandwidth of $0.4\mu m$ to 2.2 μm. The spectrometer was designed looking at many dispersive materials. Since the goal was to design a spectrometer which could be used for a wide bandwidth, especially the red shifted light, a 60^o BK7 glass prism was chosen. Using standard Sellmeyer equations for BK7. An input angle was chosen which had the proper dispersion for viewing as well as a somewhat linear range in the infrared as shown in Fig. 4.16.

In Fig. 4.16 (a), schematic of the prism design is shown with the incidence angle of 50^o and angle of the dispersed light θ. In Fig. 4.16 (b), the dispersion angle θ vs. wavelength λ is plotted from calculations, the red dashed curve accentuates the linear region. The spectrometer was calibrated using known filters and a broadband source. The filter cutoffs fit very well to the calculated dispersion allowing for good calibration.

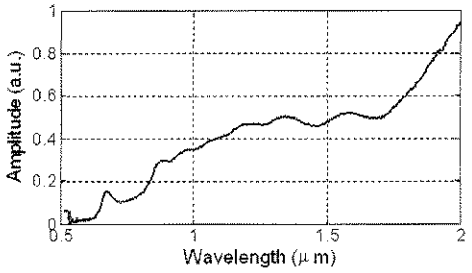

Figure 4.17: Prism spectrograph transfer function

This optical system was such that the transfer function reaching the prism spectrograph looked like the spectrum shown in Fig.fig:PrismTFunction. Dividing the measured spectrum by this transfer function results in an accurate spectrum. Since the bandwidth of the spectrum was over 1 μm, the dispersion in the optical transport required consideration. To compensate for varying focal lengths, the camera was set at an angle as seen in Fig. 4.13. The resolution of

the prism spectrograph was approximately 15 nm. Metallic neutral density filters were used for most results because they do not distort the spectral transfer function.

4.5.3 Imaging Spectrograph

The imaging spectrograph used was a 1/3 meter imaging spectrograph fitted with a 12 bit scientific camera. The imaging lens used had a 1 m focal length. The spatial resolution of the imaging spectrograph better than 15 μm. The wavelength resolution was determined primarily by the slit width, not the spectrometer length or camera. Here a 70 μm slit was commonly used giving a resolution of 7 nm.

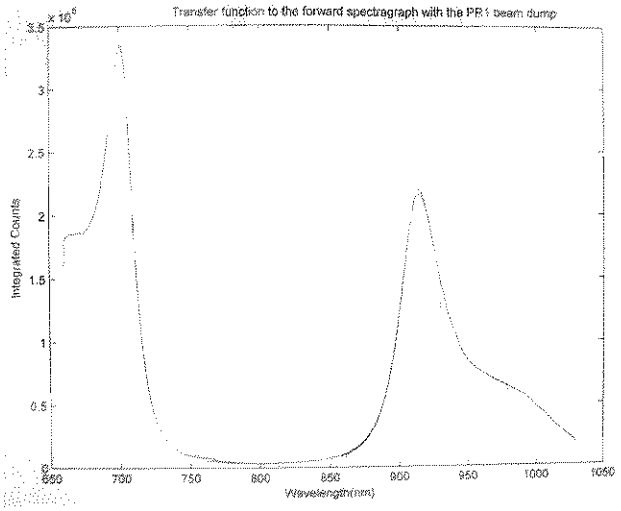

Figure 4.18: Transfer Function to the imaging spectrograph

Figure 4.18 represents the transfer function of the light relayed to the imaging spectrograph obtained using a slit located at the object plane of the experiment(above the nozzle). The slit was backlit with a bright broadband incandescent (tungsten) lamp. The transfer function of the neutral density filters used

was also used to determine the overall transfer function. By dividing by this transfer function, an accurate absolute spectrum was obtained.

Another concern with this diagnostic was imaging over a broad spectral range while using dispersive lenses to image relay to the slit of the spectrograph. In Fig. 4.19, an image of a 20 μm pinhole located at the object plane (above the nozzle), back lit with a broadband incandescent lamp is shown. The optical path was identical to the path used in the experiment. The image shown in Fig. 4.19 has been normalized over each spectral bin. What we see is that a contour image of the 20 μm pinhole. The smallest contour represents the smallest feature. The size of this small red contour remains uniform across the range of 746 μm to 915 μm without significant spatial broadening due to dispersion in the lenses used for imaging. This test assures that the spatial information is accurate regardless of the wavelength.

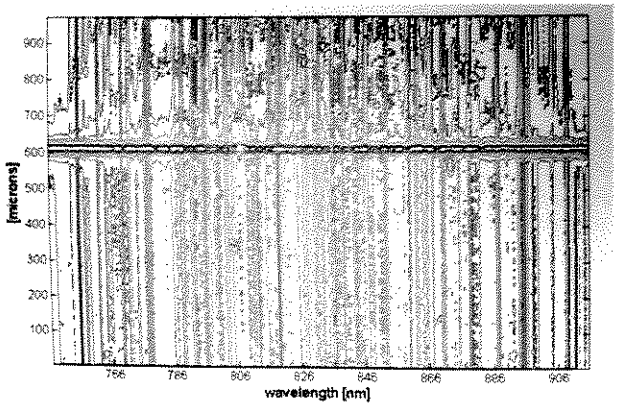

Figure 4.19: Normalized image from imaging showing good imaging over a broad spectrum

4.6 Surface Barrier Detector

The last diagnostic, not shown in Fig. 4.6 was a surface barrier detector SBD located at approximately 5^o off-axis in the forward direction outside the vacuum chamber. The SBD used in this experiment was a $200\mu m$ thick Silicon detector and was biased to between 40 and 200 volts. This detector is very sensitive to charged particles, but was used in this experiment to detect X-Rays. A calibration of the diagnostic was not performed since the detector was used only to determined if X-Rays were present or not durring any one shot. Any X-Rays detected may have resulted from Bremstralung radiation from accelerated electrons colliding with objects in the forward direction such as optics[29], or from betatron oscillations of the accelerating electrons in the plasma[75]. In this way, the SBD functioned as an indirect diagnostic for detecting the presence of any high energy electrons.

4.7 Experimental Preparation

Prior to recording each data set, careful attention was paid to ensuring that the quality of the laser met a certain level of acceptable operation. Using a photodiode in the stretched beam prior to compression, any prepulse originating in the regen Pockel cell could be monitored. By tuning the timing of Pockel's cell located between the regenerative amplifier and the 1st multipass amplifier, this prepulse was mitigated prior to shooting on the gas jet. Experimental observation revealed that the prepulse effectively disrupts the self-guiding. This could be from preionizing or changing the boundary conditions at the entrance to the gas jet.

The next step was to monitor the quality of the unfocused 2 inch spot prior to compression using a fluorescent card to visualize any hot spots or aberrations

which could lead to damage on the surface of the compressor gratings or a poor quality focal spot. Last, the compressor gratings were scanned under vacuum while monitoring the single shot autocorrelator. Pulses less than approximately 60 fs were acceptable with typical pulses less than 55 fs.

4.7.1 Nozzle alignment

To align the gas jet nozzle, the chamber was filled to approximately 5 Torr of Nitrogen. Using an approximately 2 TW pulse, a dumbbell shaped plasma was formed, see Fig. reffig:Top View Alignment. At these pressures, the plasma closely follows the ionization contour of the laser which is proportional to the laser intensity. The nozzle was positioned so that the plasma bisected the nozzle and the center of the dumbbell was at or slightly inside the front edge of the nozzle opening.

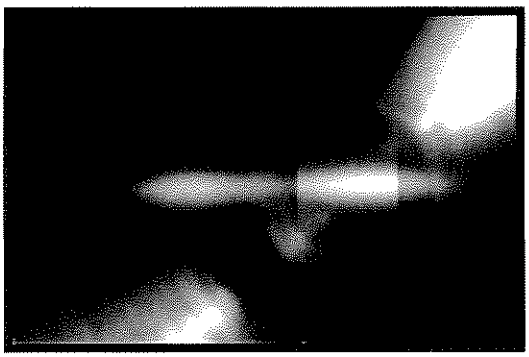

Figure 4.20: Nitrogen backfill showing typical dumbbell shape used here to align the 2mm nozzle. Here, the laser is propagating from left to right.

A small correction in the position along the z-axis a.k.a. laser propagation direction was often necessary to achieve guiding. This correction was on the order of 50 to 100 μm. Corrections to the height of the nozzle were made during the

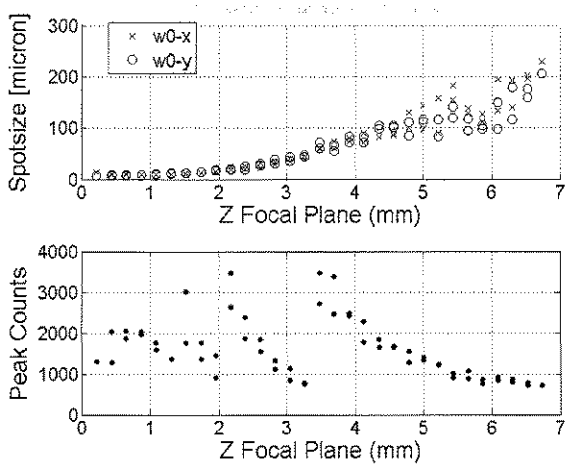

Figure 4.21: Typical Z vacuum Z-scan plots.

run using the Schlieren images.

4.7.2 Vacuum Diffraction

The first data on during a run was a scan of the laser spot starting near best focus and moving down stream towrds the exit of the gas jet. This revealed any misalignment, for example in the OAP which may have occurred. It also provided a real time estimate of the initial spot size. This scan was performed by translating the forward imaging camera fitted with a microscope objective along the propagation direction of the laser pulse. By calibrating the longitudinal magnification, a plot like figure below could be made. This was also important for day-to-day comparison between the entrance spot, the vacuum spot at the jet exit, and the self-guided spot. The best focus, determined from this scan, provided longitudinal reference in the input spot location. To determine the exit location, the microscope was translated to a position corresponding to the exit of the gas jet using the point of best vacuum focus as a reference.

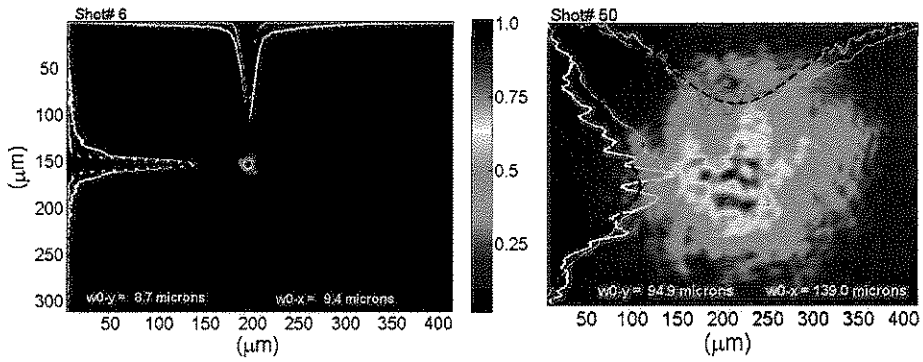

Figure 4.22: Images of the spot at best focus and 5 mm in vacuum.

Using this imaging system a typical best vacuum spot was measured as 9μm and is shown in Fig. 4.22(a). The image plane was then translated to the where the exit of the gas jet be which depended of the nozzle in use. An image of the exit plane of the 5 mm nozzle in vacuum (located 5 mm from best focus) is shown in Fig. 4.22(b).

CHAPTER 5

Experimental Results

Although recent experimental work has demonstrated that it is possible to self-guide ultrashort relativistically intense laser pulses in the blowout regime over short distances (2 mm) [71], the results presented in this thesis constitute the culmination of a systematic study of the self-guiding of such pulses over a range of plasma densities and lengths to determine what limits the self-guiding process.

In addition, although a hint of a correlation with 3D theory was suggested in reference[71], the results presented in this section show a clear correlation with theory over wide range of parameters. Early experiments relied heavily on transverse diagnostics to deduce not only whether self-guiding occured, but the length and quality of self-guiding [6]. These findings using transverse phase diagnostics (shadowgraphy) alone suggested that diffraction at the head of the pulse limited self-guiding in agreement with quasistatic theory[6]. It should be noted that the study presented here was not able to demonstrate a correlation between self-guiding as observed by a well formed spot in the forward direction with associated spectrum and features seen in using a transverse probe. It is the conclusion of this study that transverse diagnostics including imaging of the self-scattered light, shadowgraphy, interferometry etc. by themselves are not sufficient to prove that self-guiding is occuring.

In this experiment, the fact that the full array of diagnostics presented in the previous section were online for all the data presented in this section allows for

a more complete picture to be developed than was possible in prior self-guiding experiments. For example, by combining data from an energy meter, single shot autocorrelator and the plasma interferometry, an accurate value for P/P_c was available on each shot to a relatively high degree of accuracy. The addition of an imaging spectrometer provides compelling evidence as to the extend of the self-guided beam and the relative spatial extent of the wake. The prism spectrometer provides data showing significant red shifting of photons associated with the self-guided pulse.

Finally, careful attention, as described in the previou section, was paid to produce similar experimental conditions on multiple days which could be compared and reproduced.

5.1 Self-Guiding in a 2 mm long plasma

The results presented here from shooting in the 2 mm gas jet were taken using 2 to 3 TW laser pulses. In this case, the laser repetition rate was 10 HZ. This allowed the experiment to carried out at a rate which was limited by the pumping system which must pump out the Helium between puffs of the gas jet. Typically, between 30 and 40 seconds was needed to acheive background pressures in the vacuum chamber of approximately 10^{-4} Torr. Experiments requiring the use of a second Ti:Sapphire amplifier (P >3 TW) were limited to a repetition rate which was determined by the high energy pump laser used for pumping the second amplifier. This rate was approximately one shot every five minutes. However, since the power here was relatively low, the required density to achieve a $P/P_c > 1$ was also higher. And, since the pulses were not shorter than the high power pulses, the case was often that $\lambda_p < c\tau < 3\lambda_p$. This leads to difficulties in explaining the loss mechanisms and correlating the spectrum. Since the pulse is relatively long,

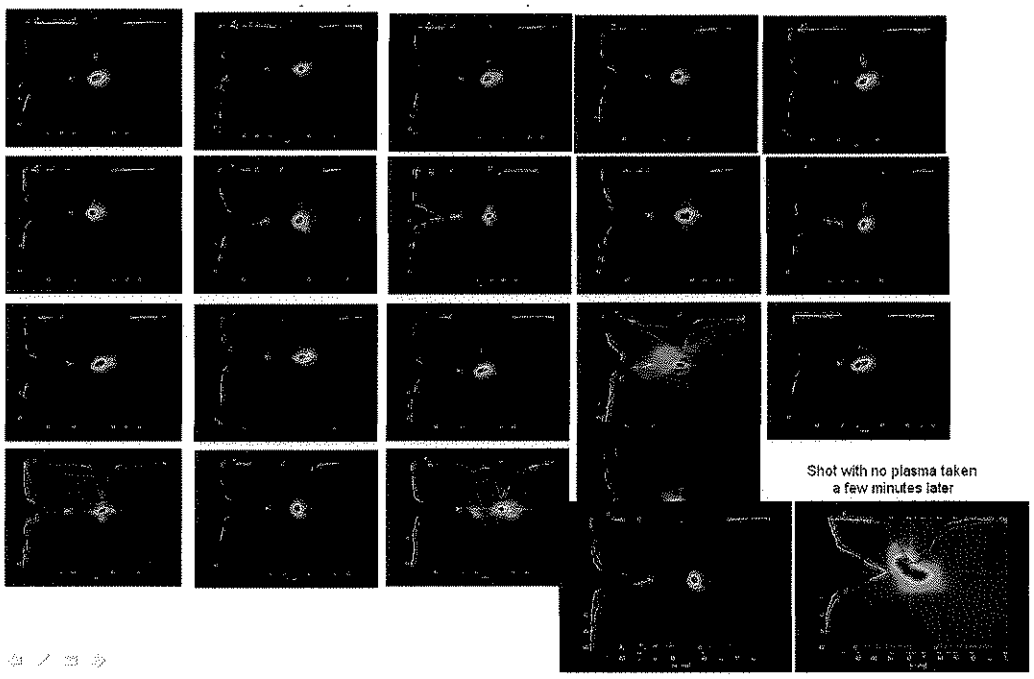

Figure 5.1: 20 consecutive shots showing small spots at the exit of the jet and a shot taken with no plasma for comparison.

it overlaps multiple periods and is therefore succeptible to Raman and hosing instabilities, as well as laser sausaging[53]. These new processes add complexity to the self-guiding process as well as interpretation of the data. Finally, since the laser power was low and the density where $P/P_c > 1$ occured was higher, the matched spot size $w_m \simeq R_b$ for $P/P_c = 1$ was smaller than the focal spot size w_o. Therefore, to acheive matched guiding in the blowout regime, for this case, required significant transverse and longitudinal evolution of the laser pulse in the plasma. Recall from the simulation and theory sections that losses are the greatest during this period of evolution. One benefit to running the experiment at a higher repetition rate was the stability of the laser system and ability to make small changes to the position of the jet, laser power and plasma density

rapidly. In Fig. 5.1, twenty consecutive guided shots are presented. These can be compared to the image of pulse at the exit of the jet with no plasma (gas jet off) in the lower right. The vertical exit spot size variation was measured to be between 8.5 μm and 12 μm over these 20 shots which suggests a degree of stability. However, the horizontal variation in exit spot size was measured between 10 μm to 20 μm. This large variation is attributed to laser sausaging and hosing[53]. In laser sausaging, the beam breaks up in longitudinal intervals of λ_p as a result of longitudinal bunching as well as defocusing, which occurs along the laser pulse at the high on-axis density regions every λ_p. The two spots seperate slightly as they propagate. This seperation may be caused also by a slight spatial chirp on the laser pulse which has recently been shown to lead to drifting of the entire plasma wake structure[1].

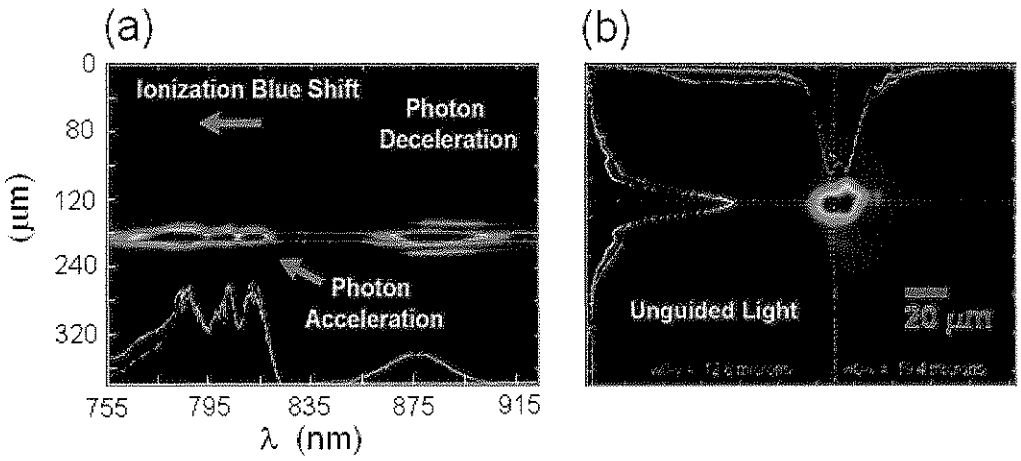

Figure 5.2: Figure (a) is of a typical imaged spectrum of the exit of the 2 mm gas jet showing a guided spot with evidence for photon acceleration and photon deceleration as well as ionization blue shifting. Figure (b) is the associated image of the exit from a CCD camera.

In Fig.5.2(a), a typical imaged spectrum from a 2 mm guided spot is shown.

This spectral image taken using an approximately (2 TW pulse) is illustrative of the nonlinear interactions expected from a self-guided ultra-short laser pulse. The density for this shot was 1.6×10^{19} cm^{-3} which gives a matched spot size of approximately 4 μm. Here, the pulse length was 52 fs (or $\sim$17 μm). After factoring in the portion of the beam which is in the central gaussian, this spot was obtained with a $P/P_c = 1$. For this density, the pulse length was 1.9 times the plasma wavelength λ_p. As a result of this relatively long length, some evidence for beam sausaging and hosing is seen in Fig.5.2(b). Here the spot size is asymetric. This is probably a result of guiding in two plasma periods where the spot has seperated into two guided spots. For lower density cases where the pulse length is shorter compared to the plasma wavelength, these types of spot distortions disappear.

Refering again to Fig.5.2(a), the interpretation of the features recorded on the imaging spectrograph have been labeled. The guided feature shown here as the bright spatially narrow feature with both blue and red shifted regions represents the self-guided pulse. Within this spatially narrow self-guided feature, the red shifting is present as a result of photon deceleration which primarily occurs in the wake excitation region of the pulse. The narrow blue shifted portion is the result of photon acceleration which occurs at the back of the first plasma period as explained in the theory chapter. The spatially broad blue shifted feature is due to ionization blue-shifting of the unguided portion of the laser pulse[34] and is seen to some degree in all spectral data. The red curve along the bottom is of the laser pulse with no plasma. The green curve shows the spectrum of guided spot or equivalently, the image of the laser spot exiting the plasma. And the white curve is a the spectrum obtained by integration over the entire CCD chip. The three curves have been normalized for the purpose of spectral feature comparison. From these curves as well as the spectral image, one can deduce that a portion

of the light was well guided and excited a high amplitude plasma wake. The fact that the spot remained small indicates that the self-guiding and therefore the plasma wake lasted for the duration of the full 2 mm of plasma propagation. Finally, a portion of the pulse was not guided either through losses due to initial coupling or diffractive head erosion as was shown in the simuations.

5.2 Self-Guiding in a 3 mm long plasma

Obtaining results from the 3 mm gas jet proved to be challenging, since the length of the nozzle was not long enough for significant pump depletion to occur for many densities, but was long enough for bunching (shortening) to occur. This led to a significant increase in intensity as seen in simulations and resulted in continous damage to down stream optics. It should be noted that these optics were not damaged by running the highest energy (power) pulses through the system with no plasma. The damage to these optics occured on the reflective coatings which were ablated off during the experiments. Without these coating, the high intensities may have caused nonlinear frequency modulation in windows and lenses resulting in unusable spectral data. Furthermore, the ablated region effectively distorted the exit image resulting in unusable forward images.

Even with the challenges presented above, some good data was obtained with the 3 mm jet. Results of the 3 mm jet experiment will be used now to show that transverse Schlieren images alone cannot be used to determine whether guiding occured on a given shot. In Fig. 5.3, two shots are compared. In Fig. 5.3(a), the Sclieren image shows that the laser propagated and ionized through the length of the plasma. The scale given shows that the plasma was 3 mm. The laser spot at the exit, which is shown as the inset of the figure shows, however, that the laser pulse broke up at some point during the propagation. In our experience, the

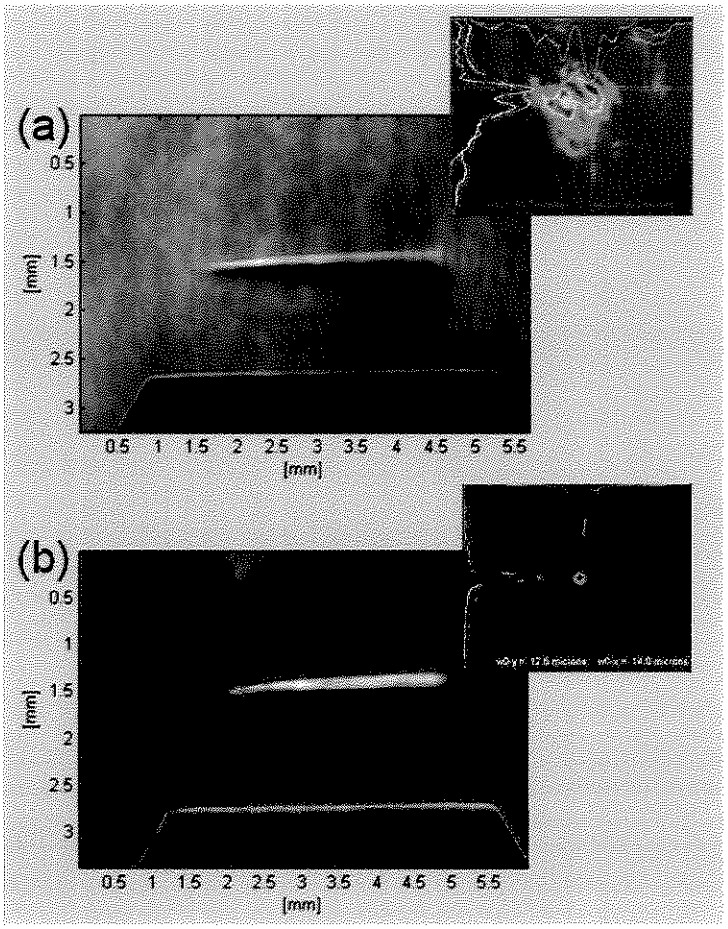

Figure 5.3: 3 mm jet plasma Schlieren images and associated exit images. A Schlieren image and unguided spot is shown in (a). A Schlieren image and guided spot at the exit is shown in (b).

primary cause for this type of spot was a laser prepulse. The prepulse, which is typically longer than the main pulse preionizes the jet. An since the prepulse is intense enough to ionize, it also is intense enough to drive its own plasma waves. Although small in amplitude compared to those driven by the main pulse, these waves can create ripples in plasma density which disturb the propagation of the main pulse. In Fig. 5.3(b), the Schlieren image shows again, that the pulse has propagated through the entire length of the plasma and has ionized. Unlike the the shot from Fig. 5.3(a), the inset from Fig. 5.3(b) shows a single, well-defined guided spot. As a result, experiments here rely entirely on the forward imaging diagnostics to determine whether the pulse has self-guided.

5.3 Self-Guiding in a 5 mm plasma

Experiments using the 5 mm jet resulted in the highest quality data from the experiments. There are several reasons why the 5 mm jet presented the clearest data. To begin with, the length of the nozzle was such that significant pump depletion occured even for the matched case. If the beam was not matched laser energy was lost to coupling. As a result, damage to optics was not an issue. Also, for the densities of interest, the pulse length, which was typically around 50 fs, resided primarily in the first plasma period. This eliminated the multiple or distorted spots seen at higher densities in the 2 mm jet and produced spectrum which could be mapped back to the effects caused by interaction of the laser pulse with the first plama period (wake). The fact that the pulse was in the first plasma period also allowed us to use our intuition gained from the nonlinear theory developed in the theory chapter of this thesis.

5.3.1 The Effects of Density and Power changes on the Percentage of Self-Guided Light

Self-guiding in the 5 mm jet was very reproducible. This allowed us to scan parameters while maintaining self-guiding even at a reltively low repetition rate. By scanning the density and looking at the contrast of the guided portion of the pulse and the background unguided portion, the effect of initially coming with a spot-size which is matched to the blowout radius $w_0 = w_m = R_b$ can be seen.

The 3D surface plots of the intensity distribution on the forward spot imaging diagnostic are shown for increasing density in Figs. 5.3.1(a) through (f). Each image was normalized to the total counts of the pixels after subtracting the background noise. This effectively divides out variation in laser energy. This process was confirmed as legitemate after the scaling of pixel count with energy (monitored on a seperate Joule meter) prooved to be linear. Next, each of the individual results were then compared and normalized to the highest value which was in turn normalized to 1. This set of data represents typical data at these densities which were reproducible.

The initial spot size for the data presented in Fig. 5.3.1 was 5.5 μm $1/e^2$ radius. In Fig. 5.3.1(a), the density is only 3×10^{18} cm^{-3}. At this density, from the condition for guiding in a plasma channel and assuming complete cavitiation initially, the requirement $k_p w_o^2 > 2$ is not satisfied. Therefore the pulse continues to diffract at some rate. After some distance of diffracting in the plasma, the peak intensity of the pulse is reduced such that the pulse can no longer drive a plasma wave. As a result, a small spot is not observed for this density. A hint of a spot begins to appear above the noise and is just barely visible in the projections at a density of 4×10^{18} cm^{-3} as seen in Fig. 5.3.1(b). At this density $k_p w_o^2 \sim 2$. Fig. 5.3.1(c) reveals the first obvious spot above the background noise.

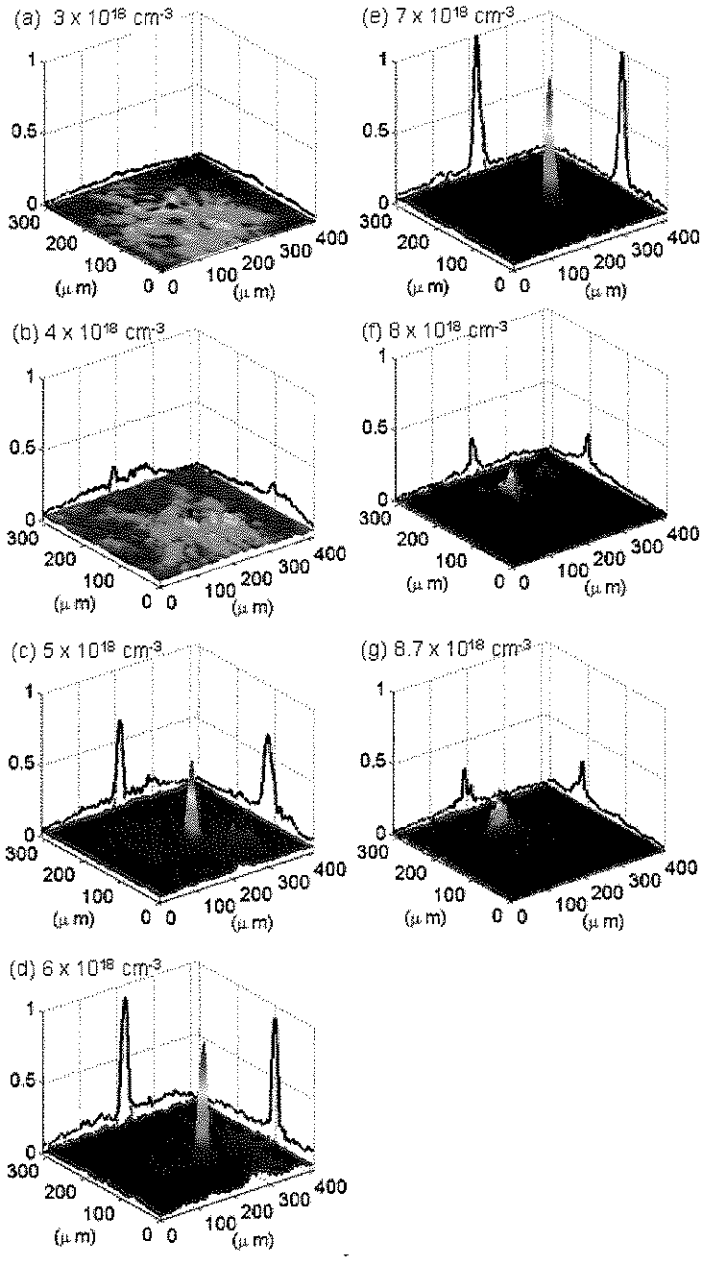

Figure 5.4: typical 3D Images of the exit of the 5 mm gas jet showing the effect of density on the contrast of the self-guided spot. The lines plotted on the axes are projections (shadows) not sums.

For $P/P_c = 1$, the matched spot size for this density is still larger than the measured w_0 of 5.5 μm and so perfect guiding is not expected. At 6×10^{18} cm^{-3}, the transmission in the spot is clearly well above the background light as is shown if Fig. 5.3.1(d). At this density, w_o is closer to the matched spotsize w_m but still smaller for $P/P_c = 1$. Finally, at 7×10^{18} cm^{-3}, the $w_o \simeq w_m$. Here the greatest contrast is achieved. As we saw in simulations, the matched spot requires only longitudinal evolution of the laser pulse which minimizes coupling losses. This minimization in losses results in a high contrast of the guided spot. As the density is increased above the matched spot condition, the pulse will evolve transversely as well as longintudinally increasing coupling losses. Additionally, loses due to nonlinear pump depletion are expected to result in less contrast. Fig. 5.3.1(f) shows the dramatic reduction in the contrast of the guided spot with respect to the background noise over a density increase of just 1×10^{18} cm^{-3}. The peak in Fig. 5.3.1(f) is 25% of the that in Fig. 5.3.1 where the spot size was matched. In Fig. 5.3.1(g), where the density was 8.7×10^{18} cm^{-3}, the spot is less well defined. The spot here has begun to break up and diffract. This is expected since this length is beyond the pump depletion length defined in the theory section as $L_{pd} = \frac{n_c}{n} c\tau$. Here n_c is the critical plasma density of 1.7×10^{21} cm^{-3}.

The plots presented in Fig. 5.3.1 are from data taken on the same day. These plots show the sum along a single axis. Here the distribution of energy can be seen. Again a peak in energy can be seen at 7×10^{18} cm^{-3}. Additionally, the important parameter P/P_c has been labeled for each of plots. The lower peaks of the lower densities can be attributed partially to lower P/P_c. At 8×10^{18} cm^{-3}, a confirmation of reduction in energy in the spot is seen as compared to the surrounding energy as the pulse nears pump depletion. From the projections alone, we can deduce a peak, however, by looking at the sum, it becomes clear that a substantial percentage of the total energy was in the guided portion of the

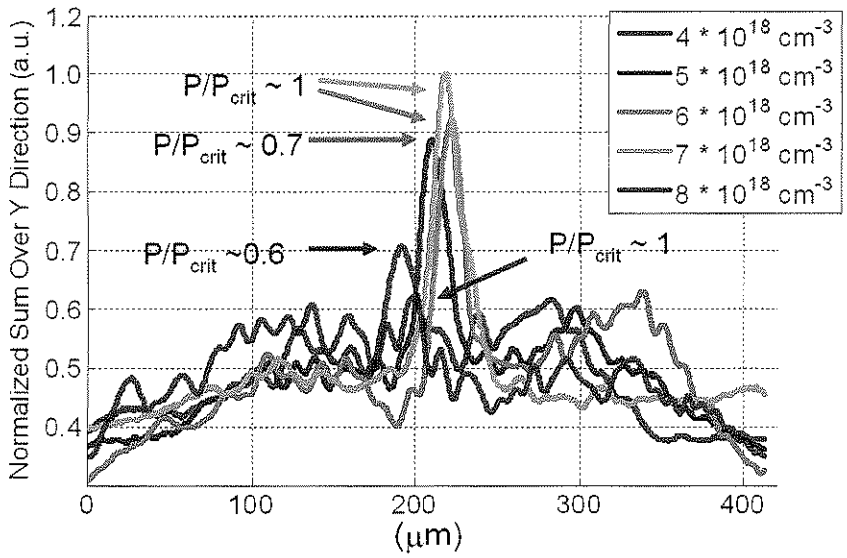

Figure 5.5: data is presented as sums of the data along the x-axis of the forward imaging camera for various densities

pulse compared to the surrounding.

In Fig. 5.6, the transmission results have been quantified. These plots show the amount of light in the guided portion of the plasma exit image compared to the amount of light in the central spot of the vacuum focus. To quantify this, each image of the exit guided spot was first analyzed by taking a line out throught the peak pixel value in both the x and y directions. Gaussian fits were performed on the line outs as described in simulation chapter. From these gaussian fits, the spot size of the exiting spot was determined. Then, a virtual spot was created from these fits and scaled so the peak is the same as the peak of the real spot. By dividing the virtual spot from the real image a percentage of energy in the guided portion at the exit was obtained. This percentage was scaled to the value of the same procedure performed on the vacuum best focus spot.

Refering again to Fig. 5.6, the total percentage of energy in the transmitted

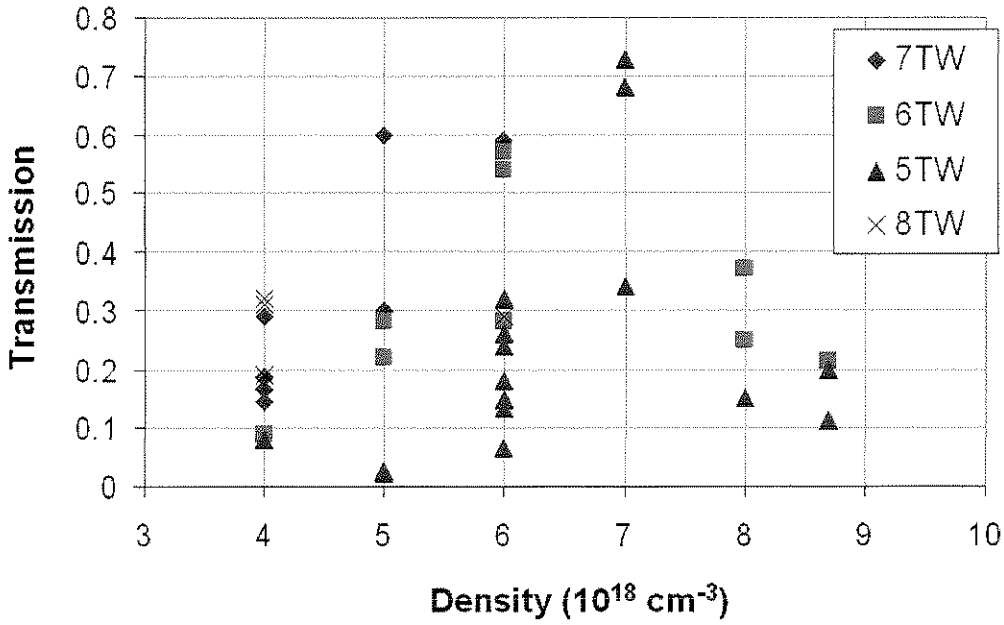

Figure 5.6: A plot of the fraction of energy in the guided spot compared to total collected transmitted light. The error here is smaller than the scatter in the data.

spot has been plotted as a function of density for powers between 5 and 8 TW. The highest percentage of power in the spot at the exit occured at the matched condition at a density of 7×10^{18} cm^{-3} with a power in the central spot near 5 TW. As the density increases from the matched density, the energy in the central spot drops off rapidly. Also, for lower densities, the energy also drops off rapidly. This behavior was also seen in the simulations presented in this dissertation. Very little energy was in the central spot at densities below 4×10^{19} cm^{-3}, and above 8.5×10^{19} cm^{-3}.

If one considers shots in the 5 TW range in Fig. 5.6, the peak at 7×10^{18} cm^{-3} becomes even more pronounced. The maximum at ~ 0.7 drops to below 0.2 at 8×10^{18} cm^{-3}. At a density of 6×10^{18} cm^{-3}, the best shot resulted in a transmission of a little greater than 0.3.

In Fig. 5.6, the data is presented as a function of density. The same data is presented as a function of pump power in Figs. 5.7(a)-(f). In Fig. 5.7(a), the density is at 4×10^{18} cm^{-3}. The fraction of energy in the guided spot appears to scale with power, but reaches a maximum of ~ 0.3 at 8 TW. Likewise Fig. 5.7(b), at a density 5×10^{18} cm^{-3}, the transmission increases with power reaching a maximum of over 0.6 at a power of 6.6 TW. At a density of 6×10^{18} cm^{-3}, Fig. 5.7(c) shows that a lot of data was taken at this density. This was a result of a mismeasured initial spot size of 7.5 μm. This spot size would have put the matched spot at closer to 6×10^{18} cm^{-3}. The lowest transmission percentage occurs for the lowest powers. The highest power also showed a significant dip. The blue curve follows data taken during the same run date. During this run, the laser pulse length was very short $\sim$ 48 fs. Fro these swhort pulses, the guiding turned on at $\sim$ 5 TW and quickly reached a semi plateu until $\sim$ 7 TW before falling off. This high power fall off could be due to the effects of

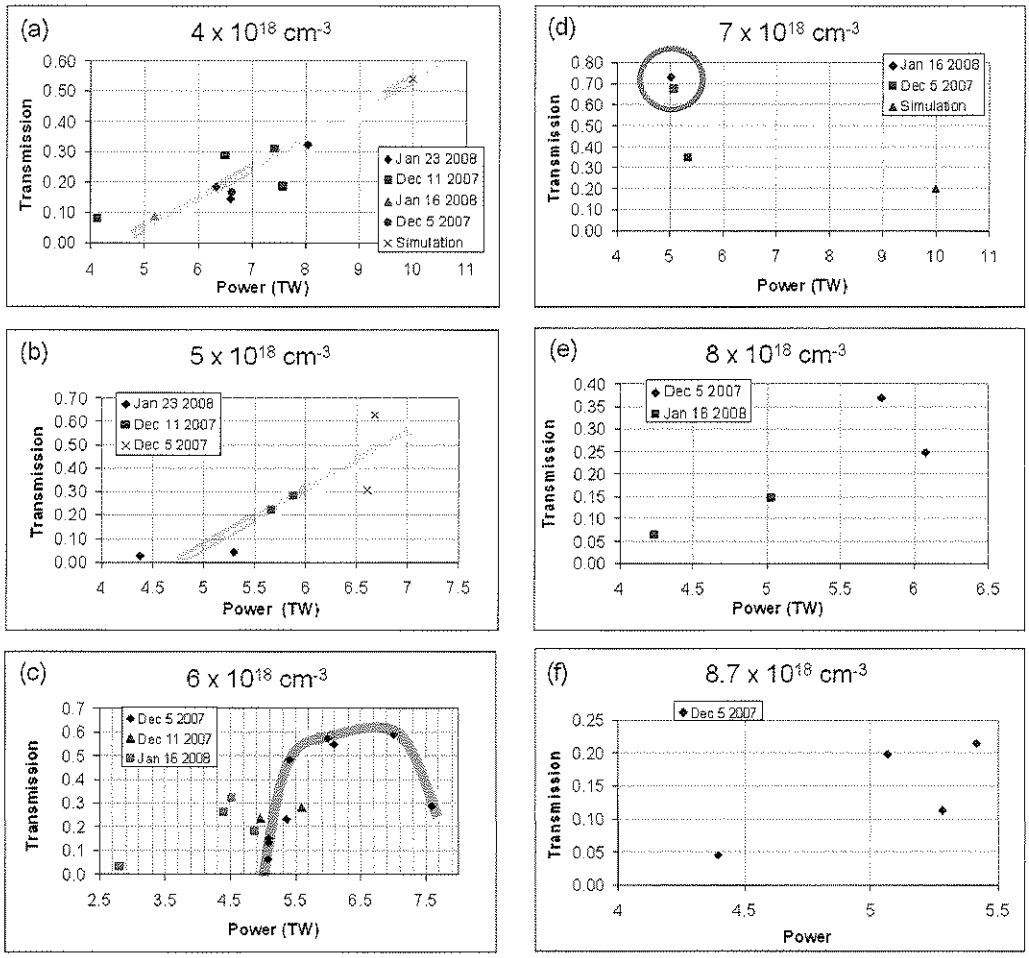

Figure 5.7: Plots of the fraction of energy in the guided spot at the exit of the 5 mm jet relative to the total energy for densities of 4, 5, 6, 7, 8, and 8.7 ^{18} cm^{-3} are plotted in Figs. a, b, c, d, e, and f respectively.

a prepulse which plays a larger role at higher powers for a fixed contrast ratio. As the power increases the prepulse can reach a level where preionzation occurs and may also produce plasma waves which disturb the plasma. Unfortunately, only 3 points could be plotted for the density of 7 $\times 10^{18}$ cm^{-3} and are shown in Fig. 5.7(d). An additional simulation point is presented to compare with experiment. Analysis was performed on the simulation data in the same way as on the experiment. The energy in the guided spot of the simulation is lower than that of the experiment. The 2 points around 0.7 represent 2 seperate dates in which this data was reproduced and represent the absolute highest percentage of energy measured in the central spot. In Fig. 5.7(e) and Fig. 5.7(f), the percentage of energy guided also increases with power. However, at these densities, the percentage of energy in the spot is lower in general.

In Figs.5.6 and 5.7, trends associated with density and power showed evidence for pump depletion as well as highlighting the importance of matched self-guiding. The nonlinear pump depletion length is approximately 5 mm for a density of 8 $\times 10^{18}$ cm^{-3} for a 55 fs laser pulse. Furthermore, the spot size is matched for 5 TW and $w_o = 5.5\ \mu m$ at a density of 7×10^{18} cm^{-3}. At this density, Fig. 5.7 clearly shows the peak percentage of energy in the guided spot which falls off for densities above and below. Above this density, the pulse is rapidly nearing pump depletion. Below this matched density, the spot size is too large to be fully self-guided[40, 41, 57] and therefore a portion of the pulse etches due to diffraction.

The power scaling exibited in Figs. 5.7 shows that higher power laser pulses are more effectively self-guided. Recall that the pump depletion length is independent of intensity and therfore independent of power. The matching condition for spot size however, is dependent on laser intensity and so it is dependent on power.

This can be expressed as $k_p w_m = 2\sqrt{2}(P/P_c)^{\frac{1}{6}}$. Here w_m is the matched spot size, P is the laser power, P_c is the critical power for relativistic self-focusing and k_p is the plasma wave number. This argument works if the initial spot size is larger than the matched spot size which happens at higher densities. However, at lower densities, a different explanation is required. At these densities, our laser is bordering on $P/P_c = 1$. Considering that the a portion of the laser at the front is below P_c, the total percentage of this portion decreases as the overall power is increased. This results in an effectively longer pulse for self-guided propagation. It may be that when self-guided propagation is considered, the pulse length should be defined as the length of the portion of the laser pulse which with power locally greater than P_c. This would be consistant with our data.

5.3.2 The Effects of Variation of Density on the forward spectrum

In the previous section, the most effective self-guiding occured at density where the initial spot-size was matched to the blowout radius. In this section, spectral data from the prism spectrometer is presented which reafirms the conclusions obtained by considering the percentage of the energy in the guided spot. The data presented in Figs. 5.8(a)-(h) shows the typical results of the spectra obtained using the prism spectrometer for densities ranging from 0 to 9×10^{18} cm^{-3}. The white curve along the bottom is a chip sum. The prism results presented show the spectrum of the pulse at the exit of the gas jet over a range of wavelengths from 0.65 μm to 1.9μm. As a reference and to illustrate the extent of the spectral modulation observed, Fig. 5.8(a) shows the vaccuum spectrum imaged at best focus of the laser pulse as obtained with the prism and is centered at 0.8 μm. Figs. 5.8(b)-(f) are spectra obtained for shots in which self-guiding was seen in the forward exit image. At a density to 4×10^{18} cm^{-3}, and imaging the exit of the jet, clear modulation of the spectrum is seen as shown in Fig. 5.8(b). The blue shifted spatially broad spectrum is the result of ionization by the portion of the pulse which is unguided. The fundamental wavelength is still clearly seen in the spectral image. Red shifted light which occurs due to photon deceleration is also clearly seen here and it is wavelength shifted out to approximately 1μm. At 5×10^{18} cm^{-3}, Fig. 5.8(c) shows a similar trend with a more pronounced hump appearing at approximatley 0.9μm. This feature was also seen in the simulation results. The blue shifting due to ionization remains. As the density is increased to 6×10^{18} cm^{-3}, the red shifted portion of the spectrum can be seen to extend out to nearly 1.5 μm as shown in Fig. 5.8(d). The blue shifted light shows a marked decrease in spectral intensity for this density compared to 5×10^{18} cm^{-3}. Here , the blue shifted light represents the uncoupled diffracted light which is seen on

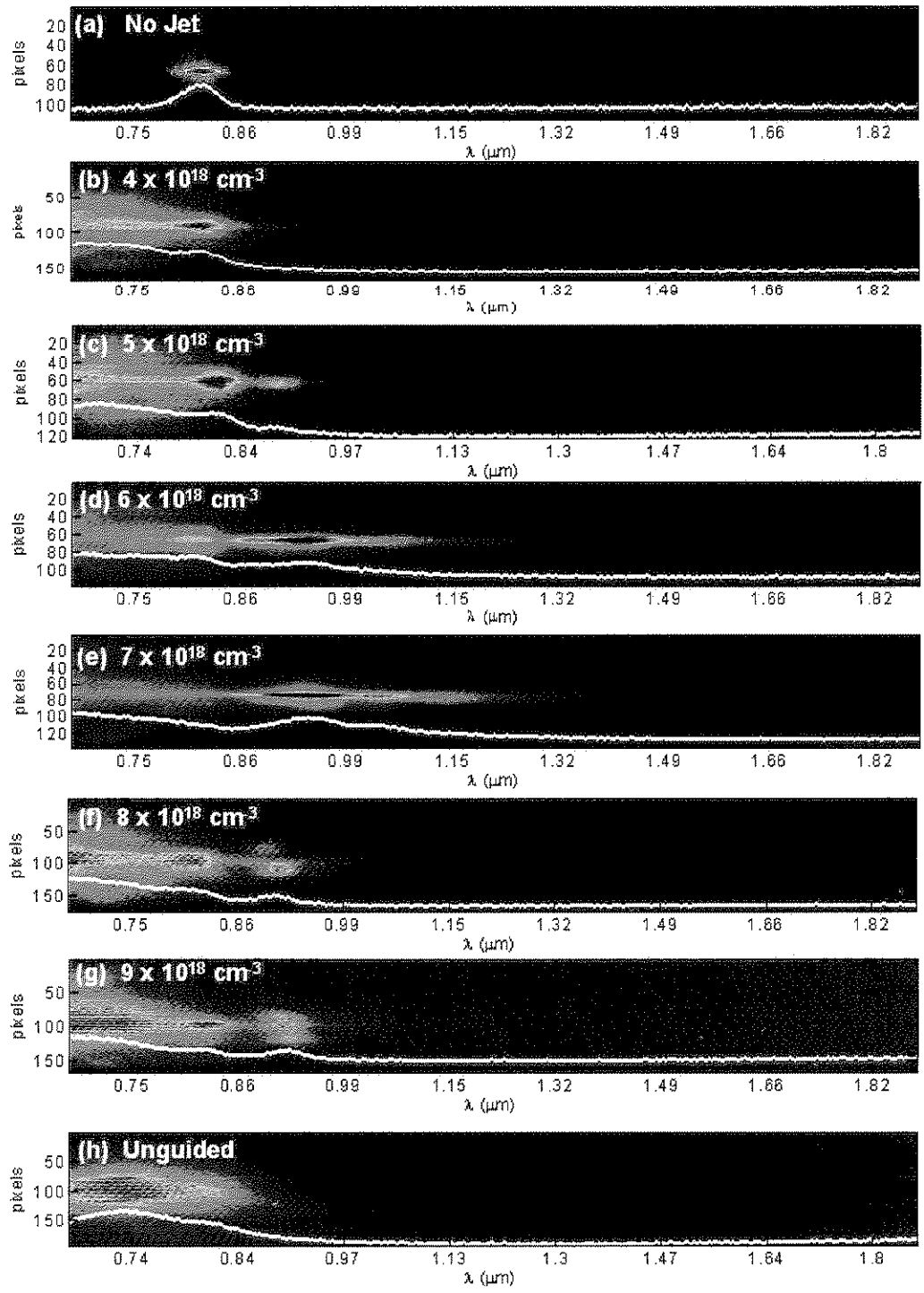

Figure 5.8: Fig.(a) is a of vacuumImages (b) through (g) taken from the prism spectrometer for guided shots at increasing densities

the forward image as the background light. A decrease in relative blue seen in this diagnostic corresponds to an increase in the percentage of light in the guided spot. Next, the spectrum for a plasma density of 7×10^{18} cm^{-3}, shown in 5.8(e) shows a marked decrease in spatially broad blue shifted light. This density also corresponds to the matched density as described in the previous section. The very strong narrow red shifted feature demonstrates that the laser pulse is efficiently driving a relativistic plasma wake. The succession of increasing red shift as the density increases is consistent with pump depletion and energy transfer to the wake as explained in the theory section. At a density of 8×10^{18} cm^{-3}, Fig. 5.8(f) shows that the strong red shifted light has disappeared. The spatially broad blue shifted portion of the spectrum has now returned. This again can be explained in light of the images of the gas jet exit which revealed a significantly lower percentage of light in the guided portion at this density. At 9×10^{18} cm^{-3}, shown in Fig. 5.8(g), the same spectral features are seen as in Fig. 5.8(f). Here, however the broad blue shifted light feature is even more pronounced compared to the red shifted feature which appears spatially larger. This suggests that the pulse has lost sufficient energy that it is no longer able to excite the wakefield and is now expanding.

Finally, Fig. 5.8(h) shows an unguided pulse. The spot here was taken from a laser shot which did not efficiently couple. This did not couple due to the fact that the z-position of the jet set the focus far from the jet entrance resulting in blue shifting which is due solely to ionization[34].

5.4 Confirmation of P_c

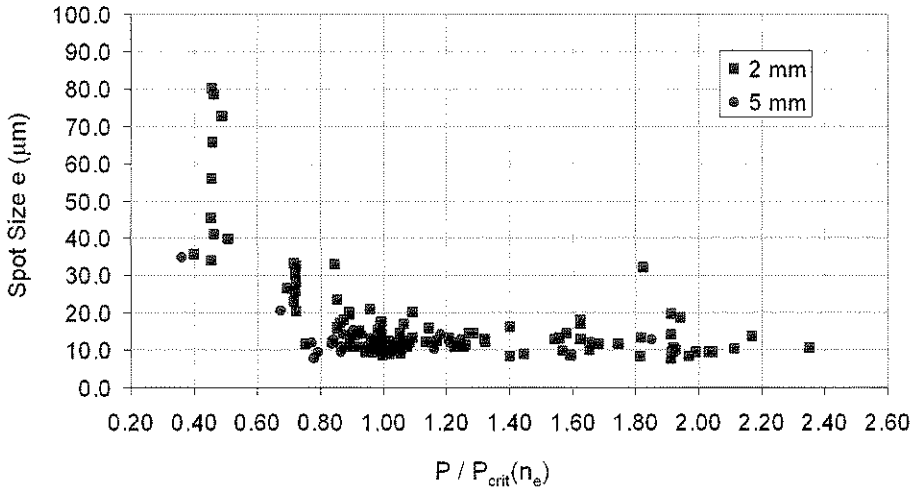

Figure 5.9: Plot of measured spot size vs. P/P_c for 2 mm and 5 mm jet experiments. The error of these measurements is smaller than the scatter in the data. Measurements are limited in resolution due collection to a minimum of $\sim 10\ \mu m$.

An important result found through these studies was a confirmation of importance of the critical power P_c for relativistic self focusing. Using the forward spot imaging with a gaussian fit, the spot size was measured. The value for P_c was obtained through density and power measurements. Although the forward image resolution was limited to approximately 9 μm, a plot could be made to compare the variation of the spot size with P/P_c.

In Fig. 5.9, the spot size at the exit of the gas jet is plotted vs. P/P_c for both the 2 mm (red squares) and 5 mm (blue circles) experiments. This plot shows a convergence to the resolution limit with increasing P/P_c. Spots plotted with powers greater than P_c maintain essentially a constant size which is the size limited by the numerical apperture of the optical system in the forward direction.

This transission from converging with P/P_c to a stable value near 10 μm occurs at $P/P_c \approx 1$ which is a confirmation of P_c.

5.5 8.5 mm Guiding

All data for the 8.5 mm long jet was taken with a density of 4.6 $\times 10^{18}$ cm^{-3} to assure that we operated below the pump depletion length L_{pd}. Additionally, the laser power was increased to maintain $P/P_c > 1$. A total of two laser shots out of $\sim$ 30 attempts produced self-guiding over this distance.

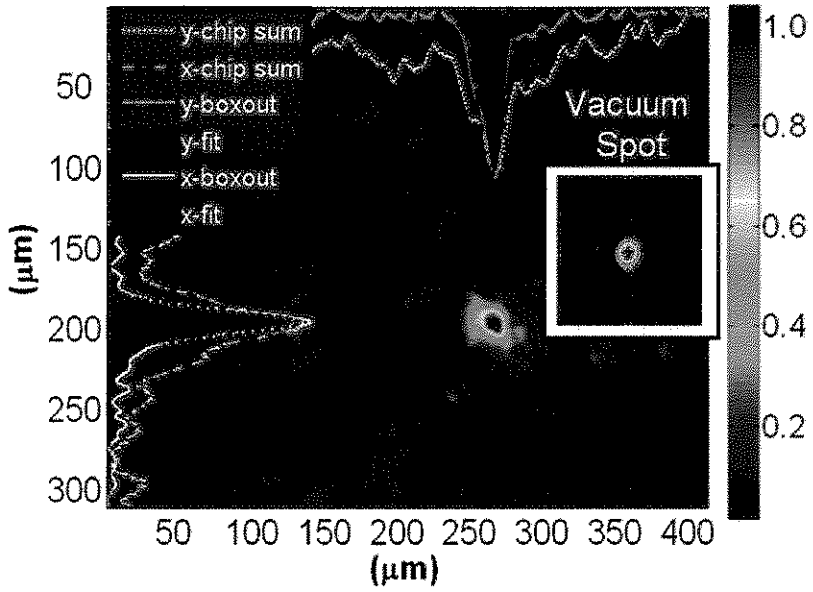

Figure 5.10: Images of the spot at 8.5 mm from entrance of the jet with a density of 4.6 $\times 10^{18}$ cm^{-3} viewed in a manner analogous to the simulation results. The white curves superimposed are sums over the chip size along each axis (horizontal and vertical). The green curves are lineouts taken through the peak. The red curves are nonlinear gaussian fits of the red curve. The inset here shows the vacuum best focus for comparison.

Self-guiding over 8.5 mm was achieved with $P/P_c = 1$. The image of one of the self-guided spots is shown in Fig. 5.10 with the associated best focal spot

measured using the same optical system. From the red curves the $1/e^2$ spot size for the exit spot was 16 μm capared to the vacuum spot size measured as $9\mu m$ using the same system. It should be noted that a high resolution imaging system revealed the actual best focus in vacuum as 5.5 μm, but was measured at a later date. The relatively high background level reveals that a significant fraction of the pulse energy was either poorly coupled or severly pump depleted. From the forward image of the guided spot of Fig. 5.10, the lineouts are com-

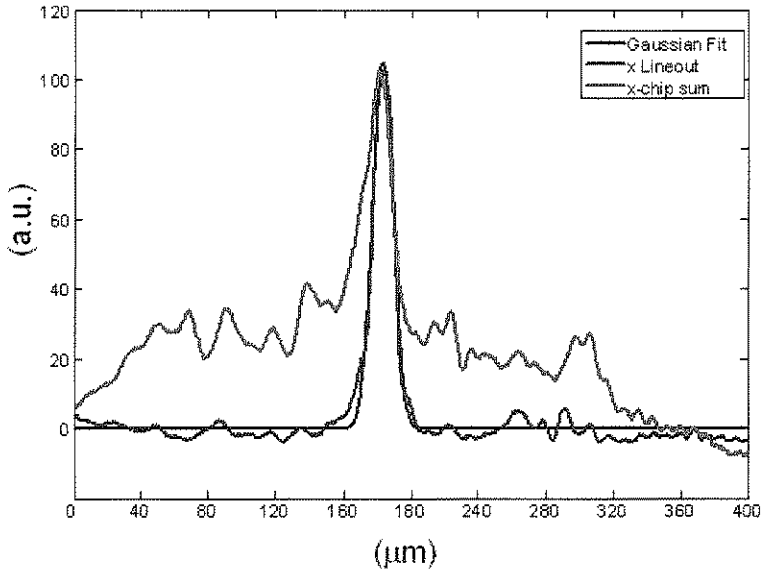

Figure 5.11: Lineouts from the exit spot image taken from the 8.5 mm gas jet

pared in Fig. 5.11. The chip sum (green curve)shows that most of the energy is in the background, however, a significant portion is still in the central spot. This conclusion is supported by the fact that the central self-guided spot can be seen clearly above the noise in the lineout (blue curve) which can be reasonably approximated by a gaussian (red curve). The transmitted intensity of two different lengths, but with a common density of 4.6×10^{18} cm$^-$3 is plotted in Fig. 5.11 by summing along the vertical axis of the CCD chip. Here the intensity distribution

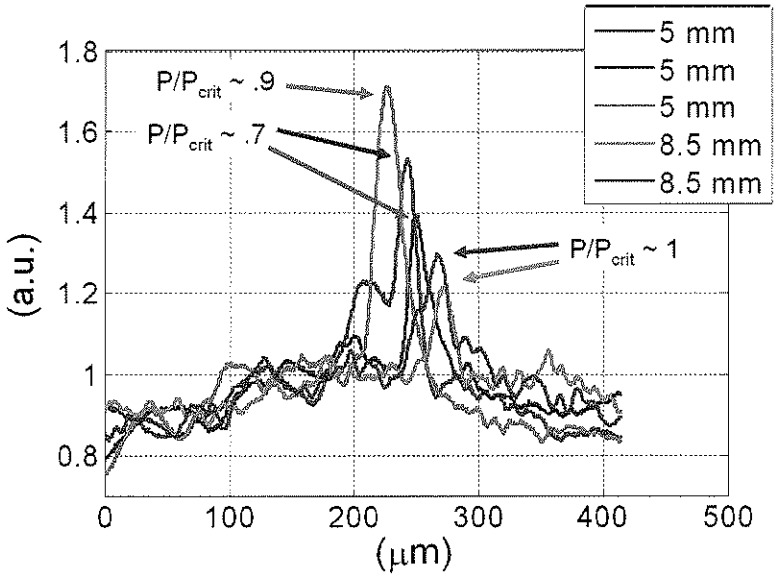

Figure 5.12: Curves showing comparative chip sums along the vertical axis for 5 mm and 8.5 mm.

of the pulses emerging from the 5 mm gas jet (plotted in red, purple, and bright green in Fig. 5.12 at the same density) shows a significantly stronger peak in energy when compared to similar plots (shown in blue-green and blue) taken for the 8.5 mm gas jet. It should be noted that the pulse power for the longer 8.5 mm gas jet guiding was slightly larger than the 5 mm gas jet. This can be deduced by considering that P/P_c has been noted for the shots and that since the density was constant and therefore P_c was constant the the power must have been increased. This scaling with distance reaffirms that self-guided energy transmission scales inversely with distance. The pump depletion of the pulse can also be seen as additional red shifting of the pulse spectrum. In Fig. 5.13, the spectrum taken from the prism spectrometer shows spectra from self-guided pulses at 4.6 $\times 10^{18}$ cm^{-3} for the 5 mm and 8.5 mm gas jets. In these spectra, the usual ionization blue shifted light is present in both the 5 and 8.5 mm data. However, the spec-

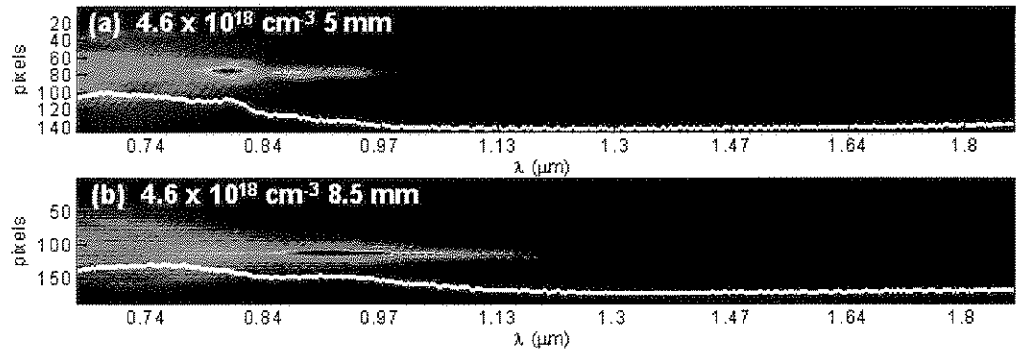

Figure 5.13: Comparison of the spectrum of the exit spot taken from the prism spectrometer between self-guiding over 5 mm and 8.5 mm at a density of 4.6 $\times 10^{18}$ cm^{-3}.

trum of the exit spot of the 8.5 mm gas jet extends much farther into the red than that of the self-guided pulse at the exit of the 5 mm gas jet supporting the claim that the self-guided pulses continue to drive nonlinear plasma waves as they propagate beyond a distance of 5 mm. Here, a portion of the pulse has shifted to a least 1.15 μm after 5 mm of propagation and at least 1.4 μm after 8.5 mm of propagation. This red shifted spectrum results from nonlinear pump depletion at the head of the short laser pulse as it propagate as described in the theory and simulation sections of this thesis. Theory predicts that the ~55 fs initial pulse should be nearly pump depleted by 8.5 mm. So far, a strong correlation between the self-guided image and the red shifting of the spectrum has been established. It has been shown that the extent of the red shifting of coupled laser pulses in which self-guiding is occuring increases with increased density and with increased length as expected. These spectral results were supported through high contrast self-guided pulses which could be seen on the forward exit imaging camera. In Fig. 5.14(a), the exit of the 8.5 mm jet is shown with no hint of guiding as the speckle noise pattern reveals no strong peak. The white curves here are of the

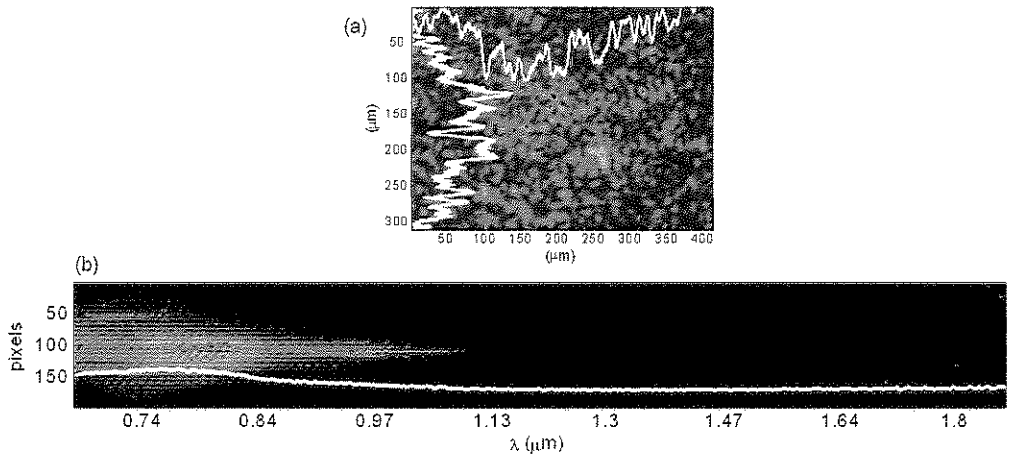

Figure 5.14: Fig.(a) is the image of the exit of a apparently unguided pulse from the 8.5 mm jet. Fig.(b) shows the spectrum from the prism spectrometer of the same shot indicating that a degree of self-guiding and wake formation did occur.

sum along each axis and also give no indication that self-guiding or wake coupling has occured. However, in Fig. 5.14(b), the spectrum of this image is presented. This spectrum, in light of previous findings presented in this section shows clearly that coupling and self-guiding to some degree has occured. This coupled pulse has eroded due to pump depletion or etched away due to diffraction at the head of the pulse or a combination.

5.6 Spectral Images of Self-Guided Spots

In this section, spectral images are presented based on different points in the evolution of the laser pulse in the plasma. By understanding where within the plasma the different wavelengths are produced, we can understand how the pulse is evolving.

The spectral imaging system imaged the exit laser spot formed onto the slit of the imaging spectrograph with a wavelength resolution of 7 nm and spatial resolution of $\sim$15 μm. The resulting imaged spectra, corrected for the λ-dependent transmission of the imaging optics, are shown in Figs.5.15(a)-(c). The corresponding figures 5.15(d),(e),and (f) have been normalized to 1 within each spectral bin. This procedure brings out the spectral content of the unguided halo which, although it is not very intense, has been shown to contain a significant amount of the total energy in the pulse spread over a much wider area.

In Figures 5.15(a)-(c), the spectral content of the resolution limited guided spot is recognized as the narrow feature stretching across the entire range of the spectrometer. The white curve along the side reveals the spatial size and total energy contrast of this guided feature for each of the 3 cases. Since $c\tau \sim \lambda_p$ for this range of density, spectral modulation must come from the interaction of the laser pulse with the first plasma period. Compared with the initial normalized spectrum of the laser (black curve), the white curve along λ shows a combination of photon acceleration at the back of the pulse which leads to a blue shift and pump depletion coming from the front of the pulse which red shifts the photons[27]. These processes, combined with the effect of group velocity dispersion in the plasma, lead to overall shortening of the laser pulse[18] as described in the theory section of this dissertation. This spatially narrow but spectrally broad feature present in Figures 5.15(a)-(f) is evidence for the existence of the

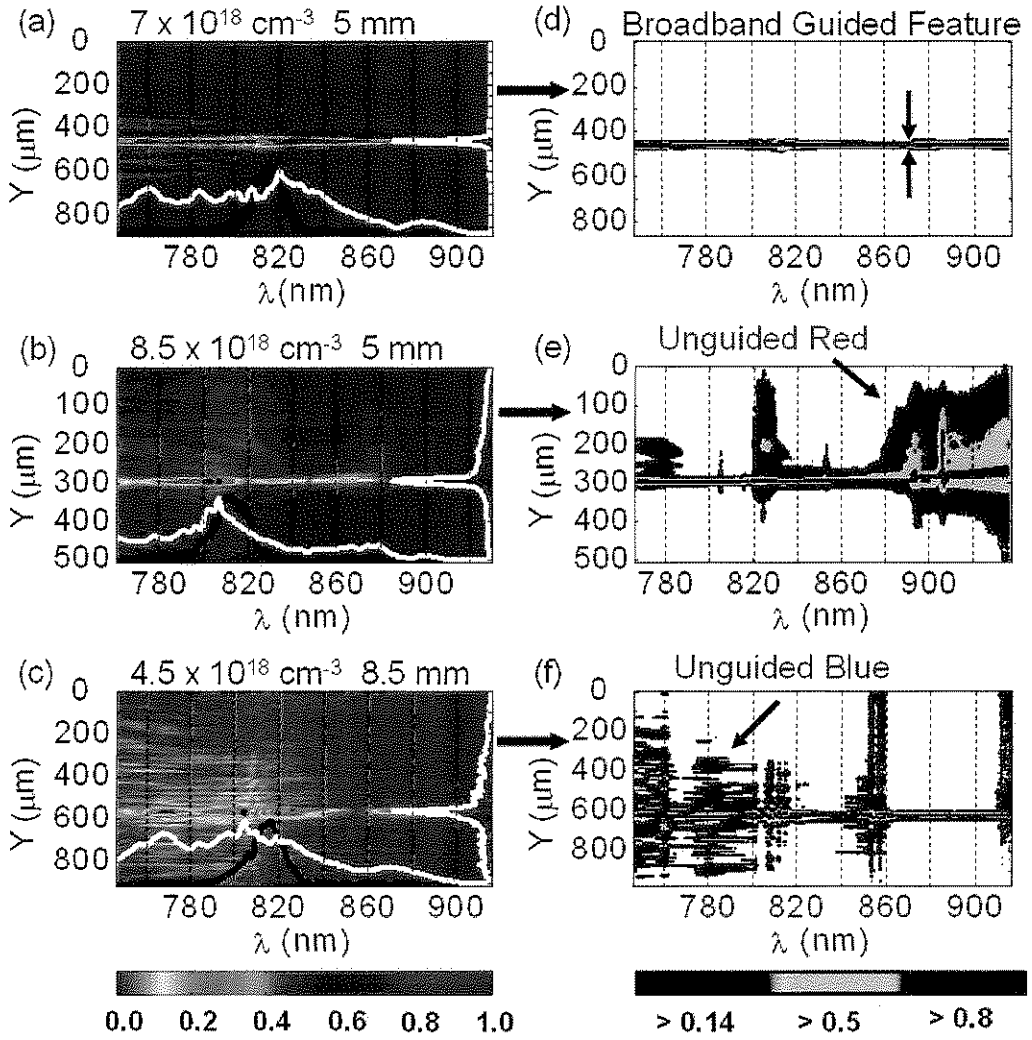

Figure 5.15: Here (a),(b) and (c) are the spectra of the pulse imaged at the exit of each gas jet. Corresponding figures (d),(e) and (f) have been normalized along each spectral bin to accentuate which wavelengths are guided. The white curve along the side (Y) is the spectrally integrated spatial distribution. The white curve along λ is the spatially integrated spectrum of the guided spot. The black curve is the initial pulse spectrum.

laser pulse residing within a large amplitude wake throughout the entire length of the plasma and since it is spatially narrow indicates that self-guiding occured through this length.

In Figures 5.15(a) and (d), the spectrum of the light exiting a 5 mm long, matched density 7×10^{18} cm^{-3} plasma is shown. This spectral image show that the entire spectral range is confined only to a narrow, guided region as expected. As the density is increased to 8.5×10^{18} cm^{-3}, Figs 5.15(b) and (e), the frequency content of the guided portion of the laser pulse is qualitatively similar to that in Fig. 5.15(a). However, Fig. 5.15(e) shows that some of the red shifted photons (which have lost energy to the wake) are spread over a much wider area because of diffraction as the pump nears depletion. Also, a portion of the diffracted photons at the front of the pulse have been blue shifted as a result of ionization [76]. This is in agreement with the prism spectrometer data.

To achieve a degree of self-guiding over 8.5 mm, as mentioned earlier, it was necessary to lower the density to $\sim 4.5 \times 10^{18}$ cm^{-3} to avoid pump depletion as described in Eq. 2.73. Additionally, the laser power was increased to maintain $P/P_c \geq 1$. For this density, recall the spot size is smaller than the matched spot size, and thus most of the laser pulse could not be self-guided. As seen in figures 5.15(c) and (f), the spectrum of the transmitted light once again shows a broadband and spatially narrow, but now, weakly guided feature. In addition, however, the broad unguided feature seen in Figure 5.15(e) is now all ionization blue shifted.

5.7 Comparison of Experimental with Simulation Spectrum

Previously in this chapter, the spectral features of the laser light transmitted by various length and density plasmas were compared. Here, the experimental data is compared with simulation.

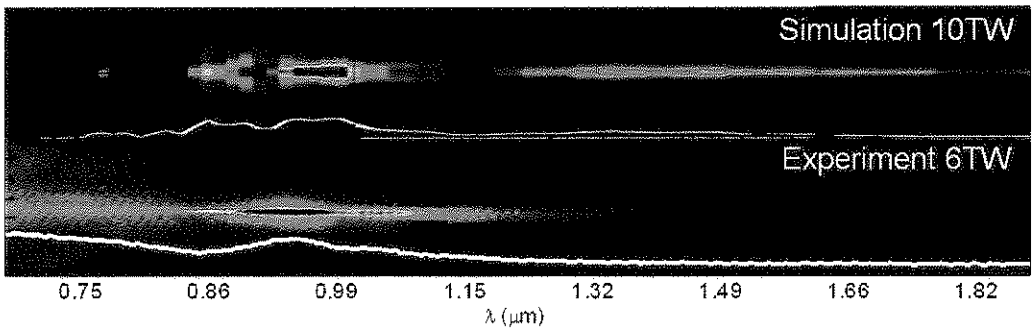

Figure 5.16: Spectrum from prism spectrograph directly compared to simulation data. the white curves along the bottom of each spectral image are sums along each spectral bin.

Fig. 5.16 shows a comparison between the experimentally measured spectrum of the transmitted light at a density of 7×10^{18} cm^{-3} and length of 5 mm with a laser power of 6 TW (5 TW in the central spot) and the spectrum of the 10 TW laser pulse after propagating through a similar plasma with a length of 4.6 mm in a PIC code. In spite of differences of laser power, the 2 images/curves show have many similarities. To begin with, both the simulation and the experimental results show evidence for a significant wake, i.e. spatially narrow spectral modulation. Indeed, as was shown earlier, the simulation allowed for direct confirmation of the presence of a highly nonlinear plasma wave wake. A clear increase in spectral intensity can be seen in the range of 900 μm in both the

simulation and experiment. Also, there appears to be a plateau up to approximately 1.15 μm in both the simulation and experiment. Also both the simulation and the experiment show spatial broadening in this range. Due to defocusing of longer wavelengths resulting from dispersion in the optical transport, the intensity of spectral features beyond 1.2 μm was obscured in the experimental image. Nonetheless, the experiment shows clearly that the range of red shifting extends beyond 1.5 μm. It should be noted that the amplitude and rate of energy transfer from the pump to the wake should be less since the laser power in the simulation was significantly higher than the experiment. This should result in a greater red shift in the simulation as was seen. Finally, ionization seen as blue shifted light off axis in the experimental result is not present in the simulation result which did not include the effects of ionization. Instead, the simulation result shows that spreading out of the pulse near the fundamental wavelength of 0.8 μm.

5.8 Self-Guiding and Pump Depletion

In Figure 5.17, the range of densities over which self-guiding was observed for gas jets of different lengths is plotted. The yellow shaded area defines the area where guiding is expected to occur. Here the highest density is bounded by L_{pd} (the solid red curve), while the lowest density is bounded by the required density channel depth (dotted pink line). For the case of complete cavitation, the required depth $\delta n/n_e$ is limited by n_e, such that $k_p w_o \geq 2$; i.e. $n_e > 4 \times 10^{18}$ cm$^{-}3$ for our w_o. The maximum propagation length for a laser pulse which erodes due to diffraction a distance of c/ω_p per initial Z_R is also plotted(dashed curve). All observed self-guided lengths excede this supposed limitation. Instead, the highest n_e points for all the plasma lengths are consistent with the limitations imposed by Eq. 2.73 scaling. At the highest densities, $c\tau > \lambda_w$, pulse shortening must

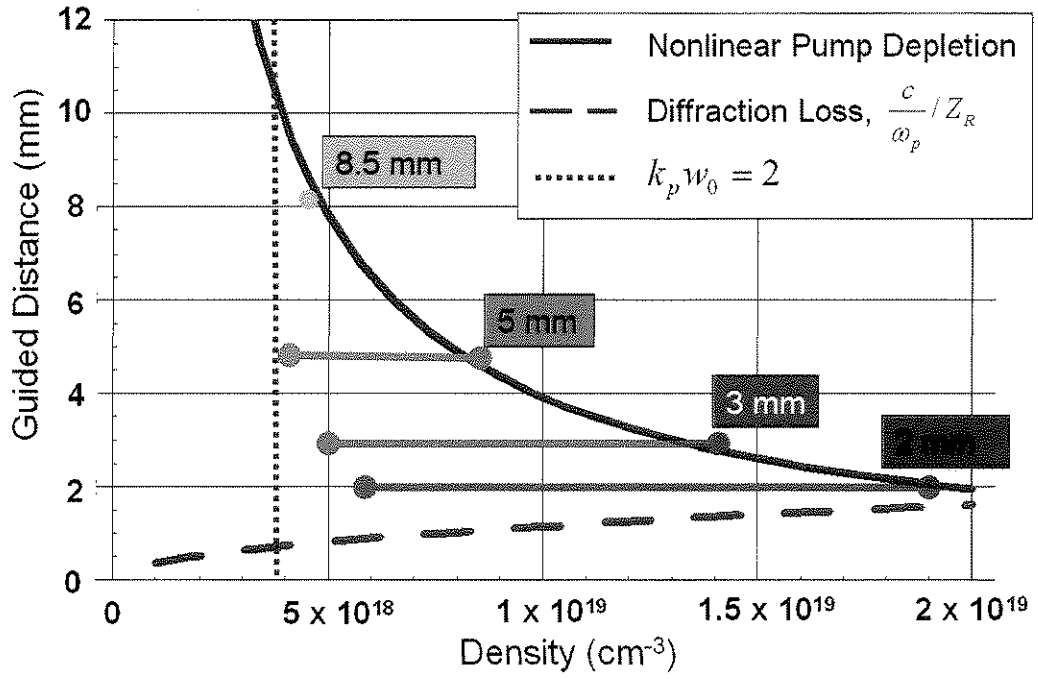

Figure 5.17: Summary of densities where self-guiding was observed in each of the four gas jets. The solid red curve is the plot of Eqn. 2.73 for a 55 fs laser pulse.

happen before the experiment is in the blow-out, LWFA regime. However, since at these highest denisities, $P/P_c >> 1$, this pulse shortening can occur rapidly. At the lowest self-guided densities, while $c\tau < \lambda_w$, P/P_c may be less than 1 which may limit the self-guiding process.

5.9 X-Rays from Self-Guided Pulses

As a final note, as mentioned in the previous section, a surface barrier detector capable of detecting x-rays was located in the forward direction. This diagnostic detected either no x-rays on the majority of shots. However, on the last self-guided shot in the 8.5 mm nozzle which produced the spectrum seen in the previous section, a large x-ray signal was detected which may have come from x-rays produced from laser wakefield accelerated electrons stopped in the chamber producing brehmstralung radiation.

CHAPTER 6

Summary

It is recognized that excitation of strong wakes traveling near light-speed in centimeter-scale plasmas is crucial for realizing a "benchtop," GeV-class laser-wakefield accelerator (LWFA)[70]. Such wakes are formed when a relativistically intense and ultra-short laser pulse propagates through an underdense plasma[39]. Extending the interaction length of such pulses, without the need to propagate them through a *preformed* plasma density channel[11, 4, 5], would greatly simplify a practical LWFA device. In this dissertation we have shown that it is possible to self-guide a portion of such a laser pulse and continue to excite a wake over tens of Rayleigh lengths until the laser pulse is energy depleted in the so-called blowout regime[9, 39, 56]. Extending this self-guided length with higher laser powers and lower plasma densities holds the promise of obtaining multi-GeV energy electron beams from a LWFA[40].

So called "matched-guiding" of a laser pulse occurs when diffraction is balanced by focusing. In a plasma, this happens when there is a radial variation of the electron density that provides the normalized on-axis depression $\delta n/n_e \simeq 4/(k_p^2 w_0^2)$, which in turn produces a refractive index channel that guides the pulse[13]. Here k_p and w_o are the plasma wave number and laser spot size, respectively, and n_e is the background electron plasma density. In the blowout regime, the laser pulse's initial ponderomotive force causes $n(r = 0)$ to go to zero within the pulse[69] and this will modify the matching condition as described

below.

When a relativistically intense $a_o \geq 1$ but ultra-short $c\tau \approx \lambda_p$ laser pulse with power $P > P_c$ enters an underdense, $\omega_p < \omega_o$, plasma, the plasma electrons at the head of the pulse are completely blown out radially during the rise time of the pulse leaving an ion channel in the first plasma period. Here $a_o = eA/mc^2$ is the normalized vector potential of the laser, ω_o and ω_p are the laser and plasma frequencies respectively, $\lambda_p = 2\pi c/\omega_p$ and $P_c \simeq 17(\omega_0/\omega_p)^2$ GW which is the critical power for relativistic self-focusing[13]. The relatively immobile plasma ions exert an attractive, space-charge force on these electrons which then rush back toward the laser axis setting up the wakefield. Most of the laser pulse thus resides inside the electron density depression and can therefore be guided. However, due to the inertia of the electrons, the density/refractive index channel is expected to form on a longitudinal scale length of c/ω_p. Therefore the very front of the laser pulse continuously erodes away due to diffraction with the degree of guiding of the remaining pulse varying along the laser pulse[65]. An estimate of the erosion rate is often quoted as c/ω_p per Rayleigh length Z_R which would limit the distance over which such an ultra-short pulse can be self-guided to a few Z_R [13]. However, nonlinear theory[9] and more recent 3D phenomenological theory[38] of LWFA show that in spite of diffractive pulse erosion, self-guiding and wake excitation is indeed possible over tens of Z_R when operating in the blowout regime.

To achieve such self-guiding in the blowout regime over a distance for significant acceleration, the laser spot size w_0 must be matched to the blowout radius R_b of the electrons so that $k_p w_o \simeq k_p R_b \simeq 2\sqrt{a_0}$. Simulations have demonstrated that spot sizes larger than the matched spot size w_m, but with $P/P_c > 1$, will converge to (and remain at) the w_m[39] where diffraction at the head of the laser

pulse is minimized. As the w_o is reduced from the matched spot size, diffraction loss tends to increase [39]. As a matched ultra-short laser pulse with $a_o \geq 2$ propagates through the plasma, the front of the laser pulse locally pump depletes as the wake is excited causing the photons to shift to longer wavelengths. These frequency downshifted photons slip back due to dispersion with a velocity $v_{etch} = c\omega_p/\omega_0$ into the wake where the transverse density depression is sufficient for guiding them. Here, v_{etch} is the difference between the linear and nonlinear group velocity of the laser pulse[9]. This considerably reduces the diffraction loss at the head of the laser pulse while simultaneously compressing the pulse and enhancing a_0[39]. This, in turn, helps maintain a strong plasma wake over many Z_R. Ultimately, energy transfer from the laser to the wake limits the length over which such a pulse can be self-guided by the plasma[9, 39]. To the first order, this nonlinear pump depletion length L_{pd} is given as[40],

$$L_{pd} = \frac{c}{v_{etch}}(c\tau) \simeq \frac{\omega_o^2}{\omega_p^2}(c\tau) \propto \frac{1}{n_e}. \tag{6.1}$$

Here τ is the full width half maximum (FWHM) duration of the laser pulse. For $2 < a_o < 20$, this scaling is independent of a_0, and therefore independent of power as long as $P/P_c > 1$. Beyond the pump depletion limit, the pulse is so severely etched that it is no longer intense enough to excite a wake and therefore no longer guided.

In this thesis, we have shown that a significant fraction of an ultra-short, but relativistically intense pulse can be guided and remain intense enough to excite a wake over a distance of up to 5 mm (or 40 Z_R) when initially focused to the matched spot size $w_m = 5.5\ \mu m$ in a plasma with density, n_e, of 7×10^{18} cm^{-3}. Furthermore, we have determined a scaling of the distance over which such a pulse can be guided as a function of n_e and deduce that this distance is consistent with the nonlinear pump depletion length L_{pd}. There have been

limited systematic prior experimental studies of the self-guided blowout regime, although many current laser wakefield experiments rely on this mechanism to extend the acceleration length[1]. In recent studies, self-guiding was observed using a 2 mm gas jet, but no limiting mechanism was demonstrated[71, 6, 77].

Experiments reported here were conducted using a Ti:Sapphire laser system capable of providing up to 12 TW, 50 $\pm$5 fs FWHM laser pulses with a central wavelength of 0.815 μm. The targets used were four different diameter (2, 3, 5 and 8.5 mm) supersonic Helium gas jets[59]. To determine whether self-guiding occured, we looked for a well defined spot in the image of the exit of plasma in addition to corresponding spectral modulation associated with a high amplitude plasma wake using two forward spectrometers. Indeed spectral analysis of the images of the laser spot that exited the plasma revealed that the self-guided portion of the laser pulse underwent considerable spectral modulation due to photon acceleration and deceleration in the wake. Energy balance of the transmitted laser spot also showed that most of the transmitted energy was in the guided spot when the beam was "matched" to the plasma. These optimally guided spots also tended to show the greatest red shift of the pulse spectrum as expected by photon deceleration by the wake. For plasma densities greater or less than the optimum density for guiding, the guided spot contained a smaller fraction of the total transmitted energy. The guided spots for these non-optimal plasma density conditions had a surrounding halo of typically blue shifted photons due to ionization of the neutral gas. Finally, by using plasmas of different length and varying plasma density and laser power, we show that the maximum distance over which such ultra-short, ultraintense laser pulses can be propagated in a plasma are limited over distances that can be predicted by the nonlinear pump depletion theory.

In conclusion, the experimental results, supported by theory and simulations, demonstrate self-guiding of intense but short laser pulses over tens of Z_R in a plasma. The observed self-guiding is most efficient when w_o is matched to the blowout radius R_b. The beam head erosion rate due to diffraction is considerably less than the simple estimate of c/ω_p per Z_R. The ultimate limit of self-guided propogation distance in the blowout regime is the pump depletion of the laser pulse.

Future work in this field will involve a quantitative analysis and comparison of the measured self-guided propagation lengths as a function of density and a_0 with comparitative simulations done with a fully explicit code such as OSIRIS and quasistatic code such as QuickPic. On the experimental front it is now possible to use a higher power laser to show GeV level energy gain using this self-guided regime.

References

[1] AIP. *Proceedings of the Advanced Accelerator Concepts, To Be Published*, 2008.

[2] S. Augst, D. Strickland, D. D. Meyerhofer, S. L. Chin, and J. H. Eberly. Tunnel ionization of nobel gases in a high-intensity laser field. *Phys. Rev. Lett.*, 63:2212–2215, 1989.

[3] I. Blumenfeld, C. E. Clayton, F. J. Decker, M. J. Hogan, C. K. Huang, R. Ischebeck, R. Iverson, C. Joshi, T. Katsouleas T, N. Kirby, W. Lu, K. A. Marsh, W. B. Mori, P. Muggli, E. Oz, R. H. Siemann, D. Walz D, and MM Zhou. Energy doubling of 42 gev electrons in a metre-scale plasma wakefield accelerator. *Nature*, 445:741–744, 2007.

[4] A. Butler, D. J. Spence, and S. M. Hooker. Guiding of high-intensity laser pulses with a hydrogen-filled capillary discharge waveguide. *Phys. Rev. Lett.*, 89:185003, 2002.

[5] C. G. R. Geddes et al. *Phys. Rev. Lett.*, 96:145002, 2005.

[6] A. Chiron, G. Bonnaud, A. Dulieu, J. L. Miquel, G. Malka, and G. Mainfray M. Louis-Jacquet. Experimental observations and simulations on relativistic self-guiding of an ultra-intense laser pulse in underdense plasmas. *Phys. Plasmas*, 3(4):1373–1401, January 1996.

[7] C. A. Coverdale, C. B. Darrow, C. D. Decker, K-C. Tzeng W. B. Mori, K. A. Marsh, C. E. Clayton, and C. Joshi. Propagation of intense subpicosecond laser pulses through underdense plasmas. *Phys. Rev. Lett.*, 74(23):4659–4652, June 1995.

[8] J. M. Dawson. Particle simulation of plasmas. *Review of Modern Physics*, 55(2):403–447, 1983.

[9] C.D. Decker, W.B. Mori, K.C., Tzeng, and T. Katsouleas. The evolution of ultra-intense, short-pulse lasers. *Phys. Plasmas*, 3(5):2047–2056, May 1996.

[10] B. J. Duda, R. G. Hemker, K. C. Tzeng, and W. B. Mori. A long-wavelength hosing instability in laser-plasma interactions. *Phys. Rev. Lett.*, 83:1978–1981, 1999.

[11] C. G. Durfee and H. M. Milchberg. Light pipe for high intensity laser pulses. *Phys. Rev. Lett.*, 71(15):2409–2412, Oct 1993.

[12] Y. Ehrlich, C. Cohen, A. Zigler, J. Krall, P. Sprangle, and E. Esarey. Guiding of high intensity laser pulses in straight and curved plasma channel experiments. *Phys. Rev. Lett.*, 77(20), 1996.

[13] E. Esarey, P. Sprangle, J. Krall, and A. Ting. *IEEE Trans. Plasma Sci.*, 24:252, 1996.

[14] E. Esarey, P. Sprangle, J. Krall, and A. Ting. Overview of plasma-based accelerator concepts. *IEEE Trans. Plasma Science*, 2(2):252–288, April 1996.

[15] E. Esarey, P. Sprangle, and A. Ting. Nonlinear theory of intense laser-plasma interactions. *Phys. Rev. Lett.*, 64:2011–2014, 1990.

[16] Fang Fang. *Some nonlinear aspects of ultra-intense laser-plasma interaction.* PhD thesis, University of California at Los Angeles, 2007.

[17] J. Faure, Y. Glinec, A. Pukhov, S. Kiselev, S. Gordienko, E. Lefebvre, J. P. Rousseau, F. Burgy, and V. Malka. A laser-plasma accelerator producing monoenergetic electron beams. *Nature*, 431(7008):541–544, Sep 2004.

[18] J Faure, Y Glinec, J. J. Santos, F. Ewald, J-P Rousseau, S Kiselev, A Pukhov, T Hosokai, and V. Malka. *Phys. Rev. Lett.*, 95:205003, 2005.

[19] J. Faure, V. Malka, J.-R. Marques, P.-G. David, F. Amiranoff, K. Ta Phuoc, and A. Rousse. Effects of pulse duration on self-focusing of ultrashort lasers in underdense plasmas. *Phys. Plasmas*, 9(3):756–759, March 2002.

[20] J. Faure, C. Rechatin, A. Norlin, Y. Glinec, and V. Malka. Controlled injection and acceleration of electrons in plasma wakefields by colliding laser pulses. *Nature*, 444(7120):737–739, Dec 2006.

[21] R. A. Fonseca, L. O. Silva, F. S. Tsung V. K. Decyk, W. Lu, C. Ren, W. B. Mori, S. Deng, S. Lee, T. Katsouleas, and J. C. Adam. Osiris: A three-dimensional, fully relativistic particle in cell code for modeling plasma based accelerators. In *Computational Science - ICCS 2002, PT III Procedings*, 2002.

[22] C. G. R. Geddes, K. Nakamura, G. R. Plateau, C. Toth, E. Cormier-Michel, E. Esarey, C. B. Schroeder, J. R. Cary, and W. B. Leemans. Plasma-density-gradient injection of low absolute-momentum-spread electron bunches. *Phys. Rev. Lett.*, 100(21):215004, Sep 2008.

[23] C. G. R. Geddes, C. Toth, J. van Tilborg, E. Esarey, C. B. Schroeder, D. Bruhwiler, C. Nieter, and J. Cary W. P. Leemans. High-quality electron beams from a laser wakefield accelerator using plasma-channel guiding. *Nature*, 431:538–541, 2004.

[24] C.G.R. Geddes, Cs. Toth, J van Tilborg, E. Esarey, C.B. Schroeder, J Cary, and W.P. Leemans. *Phys. Rev. Lett.*, 96:145002, 2005.

[25] Y. Glinec, J. Faure, V. Malka, T. Fuchs, H. Szymanowski, and U. Oelfke. Radiotherapy with laser-plasma accelerators: Monte carlo simulation of dose deposited by an experimental quasimonoenergetic electron beam. *Med. Phys.*, 33(1):155–162, Jan 2006.

[26] S. Gordienko and A. Pukhov. Scalings for ultrarelativistic laser plasmas and quasimonoenergetic electrons. *Phys. Plasmas*, 12:043109, 2005.

[27] D. F. Gordon, B. Hafizi, R. H. Hubbard, J. R. Peñano, P. Sprangle, and A. Ting. Asymmetric self-phase modulation and compression of short laser pulses in plasma channels. *Phys. Rev. Lett.*, 90:215001, 2003.

[28] S. Jackel, R. Burris, J. Grun, A. Ting, C. Manka, K. Evans, and J. Kosakowskii. Channeling of terawatt laser pulses by use of hollow waveguides. *Optics Letters*, 20(10):1086–1088, 1995.

[29] John David Jackson. *Classical Electrodynamics*. John Wiley and sons, New York,NY, 3rd edition, 1999.

[30] C. Joshi, W. B. Mori, T. Katouleas, J. M. Dawson, J. M. Kindel, and D. W. Forslund. Ultrahigh gradient particle acceleration by intense laser-driven plasma density waves. *Nature*, 31:525–529, 1984.

[31] R Jung, J Osterholz, O Willi, M Galimberti, L A Gizzi, M Borghesi, S Kar, C A Cecchetti, R Heathcote, and D Neely. Optimization and characterization of supersonic gas jet target for laser-plasma interaction studies. In *Central Laser Facility Annual Report 2004/2005*, page 23. 2005.

[32] T. Kameshima, W. Hong, K Sugiyama, X Wen, Y Wu, C. Tang, Q Zhu, Y. Gu, B B Zhang, H. Peng, S. Kurokawa, L. Chen, T T. Tajima, T. Kumita, and K. Nakajima. Gev-scale electron acceleration in a gas-filled capillary discharge waveguide. *Applied Physics Express*, 1:066001, 2008.

[33] S. Karsch, J. Osterhoff, A. Popp, T. P. Rowlands-Rees, Z. Major, M. Fuchs, B. Marx, R. Horlein, K. Schmid, L. Veisz, S. Becker, U. Schramm, B. Hidding, G. Pretzler, D. Habs, F. Gruner, F. Krausz, and S. M. Hooker. Gev-scale electron acceleration in a gas-filled capillary discharge waveguide. *New journal of physics*, 9(11):415, May 2007.

[34] L. V. Keldysh. Ionization in the field of a strong electromagnetic wave. *Sov. Phys. J. Exp. Theor. Phys.*, 20:1307, 1965.

[35] W. P. Leemans, B. Nagler B, A. J. Gonsalves, C. Toth, K. Nakamura, C. G. R. Geddes, E. Esarey, C. B. Schroeder, and S. M. Hooker. Gev electron beams from a centimetre-scale accelerator. *Nature Physic*, 2(10):696–699, Oct 2006.

[36] W. P. Leemans, C. E. Clayton, W. B. Mori, K. A. Marsh, A. Dyson, and C. Joshi. Plasma physics aspects of tunnel-ionized gases. *Phys. Rev. Lett.*, 68:321–324, 1992.

[37] W. P. Leemans, C. E. Clayton, W. B. Mori, K. A. Marsh, P. K. Kaw, A. Dyson, C. Joshi, and J. M. Wallace. Experiments and simulations of tunnel-ionized plasmas. *Phys. Rev. A*, 46:1091–1105, 1992.

[38] W. Lu, C. Huang, M. Zhou, W.B. Mori, and T. Katouleas. Nonlinear theory for relativistic plasmawakefields in the blowout regime. *Phys. Rev. Lett.*, 96:165002, 2006.

[39] W. Lu, C. Huang, M. Zhou, M. Tzoufras, F.S. Tsung, W.B. Mori, and T. Katsouleas. A nonlinear theory for multidimensional relativistic plasma wave wakefields. *Phys. Plasmas,* 13:056709, 2006.

[40] W. Lu, M. Tzoufras, C. Joshi, F.S. Tsung, W.B. Mori, Jiera, R. A. Fonseca, and L.O. Silva. Generating multi-gev electron bunches using single stage laser wakefield acceleration in a 3d nonlinear regime. *Phys. Rev. ST Accel. Beams*, 10:061301, 2007.

[41] Wei Lu. *Nonlinear Plasma Wakefield Theory and Optimum Scaling for Laser Wakefield Accelerator (LWFA) in the Blowout Regime.* PhD thesis, University of California at Los Angeles, 2006.

[42] V. Malka. Principles and applications of compact laser-plasma accelerators. *Nature Physics*, 5(6):447–453, Jun 2008.

[43] V. Malka, C. Coulaud, J. P. Geidre, V. Lopez, Z. Najmudin, and D. Neely. Characterization of neutral density profile in a wide range of pressure of cylindrical pulsed gas jets. *Rev. Sci. Inst.*, 71:2329, 2000.

[44] V. Malka, J. Faure, J. R. Marques, F. Amiranoff, J. P. Rousseau, S. Ranc, J. P. Chambaret, Z. Najmudin, B. Walton, P. Mora, and A. Solodov. Characterization of electron beams produced by ultrashort (30 fs) laser pulses. *Phys. Plasmas*, 8(6):2605–2608, June 2001.

[45] V. Malka, S. Fritzler, E. Lefebvre, M. M. Aleonard, F. Burgy, J. P Chambaret, J. F. Chemin, K. Krushelnick, G. Malka, S. P. D. Mangles, Z. Najmudin, M. Pittman, J. P. Rousseau, J. N. Scheurer, B. Walton, and A. E.

Dangor. Electron acceleration by a wake field forced by an intense ultrashort laser pulse. *Science*, 298:1596–1600, 2002.

[46] V. Malka, T. Fuchs, U. Oelfke, H. Szymanowski, J. Faure, Y. Glinec, and C. Rechatin. Laser-accelerated electrons for radiation therapy. *Med. Phys.*, 34(6):2562–2562, June 2007.

[47] S. P. D. Mangles, C. Bellei A. G. R. Thomas, A. E. Dangor, C. Kamperidis, Stefan Kneip, S. R. Nagel, L. Willingale, and Zulfikar Najmudin. Self-guided wakefield experiments driven by petawatt-class ultrashort laser pulses. *IEEE Trans. Plas. Sci.*, 34(4):1715–1721, 2008.

[48] S. P. D. Mangles, C. D. Murphy, Z. Najmudin, A G. R. Thomas, J. L. Collier, A. E. Dangor, E. J. Divall, P. S. Foster, J. G. Gallacher, C. J. Hooker, D. A. Jaroszynski, A. J. Langley, W. B. Mori, P. A. Norreys, F. S. Tsung, R. Viskup, B. R. Walton, and K. Krushelnick. Monoenergetic beams of relativistic electrons from intense laser-plasma interactions. *Nature*, 431:535–538, 2004.

[49] C.E. Max, J. Arons, and A.B. Langdon. Self-modulation and self-focusing of electromagnetic waves in plasmas. *Phys. Rev. Lett.*, 33:209, 1974.

[50] A. Modena, Z. Najmudin, A. E. Dangor, C. E. Clayton, K. A. Marsh, C. Joshi, V. Malka, C. B. Darrow, C. Danson, D. Neely, and F. N. Walsh. Electron acceleration from the breaking of relativistic plasma-waves. *Phys. Rev. Lett.*, 377:606–608, 1995.

[51] P. Mora and T. M. Antonsen. Kinetic modeling of intense, short laser pulses propagating in tenuous plasmas. *Phys. Plasma*, 4:217, 1997.

[52] Warren B. Mori. private communication, 2006.

[53] W.B. Mori. Physics of the nonlinear optics of plasmas at relativistic intensities for short-pulse lasers (invited paper). *IEEE Journal of Quantum Electrons*, 33:1942–1953, 1997.

[54] G Mourou, T. Tajima, and S. Bulanov. Optics in the relativistivc regime. *Review of Modern Physics*, 78:309–371, Jun 2006.

[55] K. Nakamura, B. Nagler, Cs. Tth, C. G. R. Geddes, C. B. Schroeder, E. Esarey, W. P. Leemans, A. J. Gonsalves, and S. M. Hooker. Gev electron beams from a centimeter-scale channel guided laser wakefield accelerator. *Phys. Plasmas*, 14(5):056708, 2007.

[56] A. Pukhov and J. Meyer ter vehn. Laser wake field acceleration: the highly non-linear broken-wave regime. *Appl. Phys. B*, 74:355–361, 2002.

[57] J.E. Ralph, K.A. Marsh, A.E. Pak, W. Lu, C.E. Clayton, F. Fang, W.B. Mori, and C. Joshi. Self-guiding of ultra-short, relativistically intense laser pulses through underdense plasmas in the blowout regime. *Submitted to Physical Review Letters.*

[58] J. B. Rosenzweig, B. Breizman, T. Katsouleas, and J. J. Su. Acceleration and focusing of electrons in two-dimensional nonlinear plasma wake fields. *Phys. Rev. A*, 44:R6189, 1991.

[59] S. Semushin and V. Malka. High density gas jet nozzle design for laser target production. *Rev. Sci. Instrum.*, 72:2961, 2001.

[60] L. O. Silva, W. B. Mori, R. Bingham, J. M. Dawson, T. M. Antonsen Jr., and P. Mora. Photon kinetics for laserplasma interactions. *IEEE Transactions on Plasma Science*, 28(4), 2000.

[61] D. J. Spence, P. D. S. Burnett, and S. M. Hooker. Measurement of the electron-density profile in a discharge-ablated capillary waveguide. *Optics Letters*, 24(14):993, 1999.

[62] P. Sprangle and E. Esarey. Interaction of ultrahigh laser fields with beams and plasmas. *Phys. Fluids B*, 4:2242, 1992.

[63] P. Sprangle, E. Esarey, J. Krall, and G. Joyce. Propagation and guiding of intense laser pulses in plasmas. *Phys. Rev. Lett.*, 69:2200–2203, 1992.

[64] P. Sprangle, E. Esarey, and A. Ting. Nonlinear interacton of intense laser pulses in plasmas. *Phys. Rev. A*, 41:4463, 1990.

[65] P. Sprangle, E. Esarey, and A. Ting. Nonlinear theory of intense laser-plasma interactions. *Phys. Rev. Lett.*, 64:2011, 1990.

[66] P. Sprangle, J. Krall, and E. Esarey. Analysis of radiation focusing and steering in the free-electron laser by use of a source-dependent expansion technique. *Phys. Rev. Lett.*, 73:3544–3547, 1994.

[67] P. Sprangle, A. Ting, and C. M. Tang. Analysis of radiation focusing and steering in the free-electron laser by use of a source-dependent expansion technique. *Phys. Rev. A*, 36:2773–2781, 1987.

[68] D. Strickland and G. Mourou. Compression of amplified chirped optical pulses. *Optics Communications*, 56(14):219–221, 1985.

[69] Guo-Zheng Sun, Edward Ott, Y.C. Lee, and Pervez Guzdar. Self-focusing of short intense pulses in plasmas. *Phys. Fluids*, 30:526, 1987.

[70] T. Tajima and J. Dawson. Laser electron-accelerator. *Phys. Rev. Lett.*, 43(4):267–270, 1979.

[71] A. G. R. Thomas, Z. Najmudin, S. P. D. Mangles, C. D. Murphy, A. E. Dangor, C Kamperidis, and K. L. Lancaster. Effects of laser-focusing conditions on propagation and monoenergetic electron production in laser-wakefield accelerators. *Phys. Rev. Lett.*, 98:095004, 2007.

[72] A. Ting, E. Esarey, and P. Sprangle. Nonlinear wake-field generation and relativistic focusing of intense laser pulses in plasmas. *Phys. Fluids B*, 2:1390–1393, 1990.

[73] A. Ting, C. I. Moore, K. Krushelnick, C. Manka, E. Esarey, P. Sprangle, R. Hubbard, H. R. Burris, R. Fischer, and M. Bainec. Plasma wakefield generation and electron acceleration in a self-modulated laser wakefield accelerator experiment. *Phys. Plasmas*, 4(5):1889–1899, May 1997.

[74] D. Umstadter, S. Y. Chen, A. Maksimchuk, G. Mourou, and R. Wagner. Nonlinear optics in relativistic plasmas and laser wake field acceleration of electrons. *Science*, 273:472–475, July 1996.

[75] Shuoqin Wang, C. E. Clayton, B. E. Blue, E. S. Dodd, K. A. Marsh, W. B. Mori, C. Joshi, S. Lee, P. Muggli, T. Katsouleas, F. J. Decker, M. J. Hogan, R. H. Iverson, P. Raimondi, D. Walz, R. Siemann, and R. Assmann. X-ray emission from betatron motion in a plasma wiggler. *Phys. Rev. Lett.*, 88:135004, 2002.

[76] Wm. M. Wood, G. B. Focht, and M.C. Downer. Tight focusing and blue shifting of millijoule femtosecond pulses from a conical axicon amplifier. *Opt. Lett.*, 13(11):984–986, 1988.

[77] T.-W. Yau, C.-J. Hsu, H.-H. Chu, Y.-H. Chen, C.-H. Lee, J. Wang, and S.-Y. Chen. Dependence of relativistic self-guiding and raman forward scattering on duration and chirp of an intense laser pulse propagating in a plasma. *Phys. Plasmas*, 9(2):391–394, February 2002.

[78] P. E. Young, J. H. .Hammer, S. C. Wilks, and W. L. Kruer. Laser beam propagation and channel formation in underdense plasmas. *Phys. Plasmas*, 2(7):2825–2834, 1995.